

Application of Inkjet-Printing Technology to Micro-Electro-Mechanical Systems

Eung Seok Park



Electrical Engineering and Computer Sciences
University of California at Berkeley

Technical Report No. UCB/EECS-2014-44

<http://www.eecs.berkeley.edu/Pubs/TechRpts/2014/EECS-2014-44.html>

May 1, 2014

Copyright © 2014, by the author(s).
All rights reserved.

Permission to make digital or hard copies of all or part of this work for personal or classroom use is granted without fee provided that copies are not made or distributed for profit or commercial advantage and that copies bear this notice and the full citation on the first page. To copy otherwise, to republish, to post on servers or to redistribute to lists, requires prior specific permission.

**Application of Inkjet-Printing Technology to Micro-Electro-Mechanical
Systems**

by

Eung Seok Park

A dissertation submitted in partial satisfaction of the
requirements for the degree of
Doctor of Philosophy

in

Engineering – Electrical Engineering and Computer Sciences

in the

Graduate Division

of the

University of California, Berkeley

Committee in charge:

Professor Tsu-Jae King Liu, Co-chair
Professor Vivek Subramanian, Co-chair
Professor Liwei Lin
Professor Ana Claudia Arias

Fall 2013

**Application of Inkjet-Printing Technology to Micro-Electro-Mechanical
Systems**

Copyright 2013
by
Eung Seok Park

Abstract

Application of Inkjet-Printing Technology to Micro-Electro-Mechanical Systems

by

Eung Seok Park

Doctor of Philosophy in Engineering – Electrical Engineering and Computer Sciences

University of California, Berkeley

Professor Tsu-Jae King Liu, Co-chair

Professor Vivek Subramanian, Co-chair

Printed electronics employing solution-processed materials is considered to be the key to realizing low-cost large-area electronic systems, but the performance of printed transistors is not generally adequate for most intended applications due to limited performance of printable semiconductors. In this dissertation, I propose an alternative approach of a printed switch, where the use of semiconductors can be avoided by building mechanical switches with printed metal nanoparticles. I provide the first demonstration of inkjet-printed micro-electro-mechanical (MEM) switches with abrupt switching characteristics, very low on-state resistance (10Ω), and nearly perfect off-state behavior with immeasurable leakage with on/off current ratio of 10^7 . The devices are fabricated using a novel process scheme to build 3-dimensional cantilever structures from solution-processed metallic nanoparticles and sacrificial polymers. These printed MEM switches thus represent a uniquely attractive path for realizing printed electronics. I will also discuss an inkjet-printed microshell encapsulation as a new zero-level packaging technology. Inkjet-printing of silver nanoparticle ink is demonstrated to form porous microshells through which sacrificial oxide can be selectively removed to release MEMS structures. A second inkjet printing process using finer gold nanoparticle ink or polymer is demonstrated to effectively seal the microshells. This inkjet-printed microshell encapsulation technology is successfully applied to a MEM relay, and is demonstrated to mitigate the issue of contact oxidation. Specifically, the stability of the relay ON-state resistance is dramatically improved by more than a factor of 100.

To my parents.

Contents

Contents	ii
List of Figures	iv
List of Tables	vii
1 Introduction	1
1.1 Inkjet Printing Technology	1
1.2 Printed Mechanical Switches	2
1.3 Microshell Encapsulation	5
1.4 Printed Microshell Encapsulation	7
1.5 Dissertation Outline	8
Bibliography	9
2 Physical Background	13
2.1 Basic Principles of Inkjet Printing	13
2.2 Mechanical/Electrical Modeling of A Cantilever-Beam	19
2.3 Nanoindentation	23
Bibliography	28
3 Inkjet-Printed Micro-Electro-Mechanical Switch	30
3.1 Introduction	30
3.2 Advantages of Printed Mechanical Switches	30
3.3 Structure and Operating Principle of Printed MEM Switches	31
3.4 Fabrication Process	32
3.5 Electrical Characteristics of Printed MEM Switches	39
3.6 Mechanical Properties	42
3.7 Conclusion	45
Bibliography	46

4	Scaling of Inkjet-Printed Micro-Electro-Mechanical Switch	48
4.1	Introduction	48
4.2	Process Optimization for Scaled Actuation-gap Devices	48
4.3	Pull-in Voltage Reduction from Scaled Actuation Gap	51
4.4	Conclusion	53
	Bibliography	54
5	Microshell Encapsulation using Inkjet-Printed Nanoparticle Films	55
5.1	Introduction	55
5.2	The Microshell Material Requirements	55
5.3	Inkjet-Printed Microshell Process	58
5.4	Structural Properties of the Printed Microshell	62
5.5	Sealing Microshell with Finer-Sized Nanoparticles	62
5.6	Conclusion	66
	Bibliography	67
6	Integration of Printed Microshell with Relay Fabrication for Improved Contact Stability	69
6.1	Introduction	69
6.2	Process Integration of Inkjet-Printed Microshell	70
6.3	Contact Resistance Stability Results	78
6.4	Conclusion	81
	Bibliography	82
7	Conclusion	83
7.1	Summary and Conclusion	83
7.2	Contributions of This Work	84
7.3	Suggested Future Work	85
	Bibliography	89

List of Figures

1.1	Basic circuit diagram for an active matrix liquid crystal display.	2
1.2	Effective carrier mobility values reported in the literature.	4
1.3	Schematic illustration of an example of MEM relay device.	6
2.1	Schematic illustration of drop-on-demand nozzles.	14
2.2	Schematic illustration of the drop formation process steps in sequence.	15
2.3	Micrographs of drop formation from the piezoelectric nozzles used in this work.	16
2.4	Micrograph of a piezoelectric nozzle printing a pattern with missing lines due to jet instability.	17
2.5	Schematic illustration of force balance for a droplet in equilibrium.	18
2.6	Micrograph of contact angle measurement using a goniometer.	19
2.7	Schematic diagrams illustrate different types of loading on the cantilever beam.	20
2.8	Schematic illustration of dimensions used in cantilever beam analysis.	22
2.9	Normalized force <i>vs.</i> normalized displacement of the cantilever beam.	24
2.10	An example of a load <i>vs.</i> displacement curve in a typical nanoindentation measurement.	25
2.11	Schematic illustration of the unloading procedure in nanoindentation measurement.	26
3.1	Structure and operation of the printed MEM switch design is illustrated.	32
3.2	Illustration of the process used to fabricate the MEM switches.	34
3.3	Measured height profile of the printed electrodes with dimpled drain structure. .	35
3.4	Profile of contact dimple structure.	35
3.5	Dependence of contact dimple parameters on the number of printed drops. . . .	36
3.6	Dependence of contact angle of water on the PMMA surface on UV-ozone exposure time.	37
3.7	Measured source-beam thickness <i>vs.</i> number of printed layers.	38
3.8	“Wrinkles” on the printed layer upon drying process.	38
3.9	Illustration of the two-step anchoring process.	39
3.10	Steady-state electrical characteristics of the printed MEM switch.	40
3.11	Circuit schematic of the measurement setup used for electrical characterization of the printed MEM switch.	40
3.12	Dynamic electrical characteristics of the printed MEM switch.	41

3.13	Dependence of pull-in delay on applied gate-to-source voltage V_{GS} .	42
3.14	Endurance measurement of the printed MEM switches.	43
3.15	Structural analysis of the printed cantilever by nanoindentation technique.	44
4.1	Micrographs showing two-step beam formation process.	49
4.2	Effects of UV-ozone (UVO) exposure time on the process.	50
4.3	Measured current-voltage characteristics of scaled-gap printed switches.	52
4.4	Measured current-voltage characteristics for two printed switches with the gate electrode farther from the anchor than the drain electrode.	53
5.1	Process flow for microshell encapsulation.	56
5.2	Process flow for microshells employing etch-access windows.	57
5.3	Process flow for microshells employing etch-release holes.	57
5.4	Schematic illustration of inkjet-printed microshell encapsulation process.	58
5.5	Micrographs of inkjet-printed Ag microshell.	59
5.6	Measured thicknesses of inkjet-printed films after sintering at 200°C and 400°C.	60
5.7	Micrographs of dried inkjet-printed nanoparticle films composed of multiple layers, dried at 60°C.	61
5.8	Cross-sectional SEM images of an inkjet-printed Ag microshell after exposure to HF vapor.	61
5.9	Measured height profiles of inkjet-printed microshells before and after HF vapor etch, obtained with an optical profilometer	63
5.10	Cross-sectional SEM images of printed nanoparticle films.	64
5.11	Measured profile of the encapsulated sacrificial oxide after exposure of its sealed microshell to HF vapor and subsequent removal of the microshell by wet etching.	65
5.12	Measured height profiles of microshells fabricated with differences in the sintering process.	65
6.1	Schematic diagram illustrating the structure and operating principle of a six-terminal MEM relay in this work.	70
6.2	Schematic illustration of the fabrication process for encapsulating a relay in a microshell.	71
6.3	SEM image of a single encapsulated relay.	72
6.4	Surface profiles of a microshell-encapsulated MEM relay.	73
6.5	Micrograph of the patterned oxide islands for microshells encapsulating MEM relays.	74
6.6	Micrograph of printed Ag nanoparticle ink on patterned oxide islands.	75
6.7	Surface profiles of a microshell-encapsulated MEM relay after completion of microshell deposition.	76
6.8	Surface profiles of a microshell-encapsulated MEM relay after oxide removal by vapor HF etch.	77
6.9	Plot of calculated maximum shell deflection.	78

6.10	Comparison of measured $I - V$ characteristics for bare relay <i>vs.</i> an encapsulated relay.	79
6.11	Test setup for monitoring relay On-state resistance over many hot-switching cycles.	80
6.12	Evolution of contact resistance with the number of hot-switching cycles, for bare <i>vs.</i> encapsulated relays.	81
7.1	Measured current-carrying capacity of the printed MEM switches.	86
7.2	Schematic diagrams illustrate design schemes for printed four-terminal relays. .	87

List of Tables

1.1	Reported effective carrier mobility values of solution-processed semiconductor polymers in literature	3
3.1	Design parameters and values of the fabricated printed MEM switches.	33
5.1	Length values of microshells investigated to verify structural collapse upon release.	66
6.1	Parameters and values of dimensions in the microshell test structures.	74

Acknowledgments

First of all, I would like to express my sincere gratitude towards my advisors, Professor Tsu-Jae King Liu and Professor Vivek Subramanian. Without their advice and guidance, it would have been much more challenging, if not impossible, for me to complete the Ph.D work. I am truly lucky to have advisors whom I can admire in intellectual aspect and respect their personality. I am also grateful to Professor Liwei Lin and Professor Ana Claudia Arias for being on my qualification and dissertation committees and providing valuable feedbacks to improve my research. I would also like to thank Professor Gyu-Tae Kim (Korea University) and Professor Jongyoon Han (MIT), who advised and encouraged me to pursue a doctoral study.

I would also like to express my gratitude to many of my colleagues that I have interacted with from the two research groups; Min Hee Cho, Xin Sun, Donovan Lee, Rhesa Nathanael, Peter Matheu, Hei Kam, Jaeseok Jeon, Changhwan Shin, Sung Hwan Kim, Byron Ho, Zachery Jacobson, Wookhyun Kwon, Nattapol Damrongplasit, Jack Yaung, Nuo Xu, Louis Hutin, Yenhao Chen, I-Ru Chen, Yibo Liao, Sun Young Kim, Chuang Qian, Jun Fujiki, Peng Zheng, Ji-Zheng Liu, Steve Volkman, Alejandro de la Fuente Vornbrock, Shong Yin, Teymur Bakhishev, Huai-Yuan Tseng, Dan Soltman, Lakshmi Jagannathan, Feng Pan, Jaewon Jang, Hongki Kang, Kyle Braam, Sarah Swisher, Rungrot Kitsomboonloha, Rumi Karim, Jake Sadie, Andre Zeumault, Gerd Grau, Garret McKerricher, Jing Chen, Seungjun Chung, Kareem Elassy, Michael Rodder, Koshin Hosoya, Himamshu Nallan, and Artos Cen. One of the joys of studying at UC Berkeley was having such amazing colleagues whom I always found something to learn from. Funding for this research was provided by DARPA/MTO NEMS Program and I am also grateful to the Fulbright Program and its student service officers for the financial support and advising.

Finally, I owe my gracious thanks to my family for their limitless support. They have always encouraged and believed in me, making me a better person everyday. I would also thank my wife and son for their understanding and love, and simply being there for me.

Chapter 1

Introduction

1.1 Inkjet Printing Technology

Printed electronics have observed rapid progress over the last decade due to the development of both printing technology and the required printable solution-processed materials. There are various printing technologies available such as inkjet-printing, gravure printing, screen printing, offset lithography and flexography. The basic principle of printing is the transfer of patterns, via a vehicle of liquid ink from a pre-patterned master set to a target substrate. Inkjet printing has a unique characteristic in this regard, as it has the capability of direct writing without any predefined master pattern; it can deposit ink to any arbitrary positions on the substrate by means of precisely controlled movable nozzles and a plate on which substrates are loaded.

Originally invented as a technology to record information by deposition of ink on paper, the inkjet printing technology has been transformed into a fabrication method to build electron devices with development of printable materials. Especially, solution-processed semiconductor polymers and metals have great impact on both the processability and performance of printed electronic devices. One of the fundamental devices fabricated in the field of printed electronics is a thin-film transistor (TFT). Probably the biggest driving force behind the research effort on developing the printed TFTs using solution-processed materials is the capability of making flexible electronics with lower cost. For example, TFTs are universally used as switching devices for the pixels in active matrix liquid crystal displays (AMLCDs) [1, 2, 3] (See Fig. 1.1). To lower the display module cost, it is also desirable to fabricate the display row driver circuitry monolithically on the panel in the regions peripheral to the pixel array. For a video display, the switches in the row driver circuitry must operate at a frequency > 100 kHz to implement the shift registers. As demand grows for large-area displays (business TVs, electronic bulletin boards, signage, *etc.*) and flexible displays, lower-cost approaches to manufacturing switches on large-area substrates will be needed.

Recently, inkjet-printed TFTs have been demonstrated as pixel switches for AMLCDs [4, 5, 6] due to their potentially low cost and compatibility with flexible substrates. Although

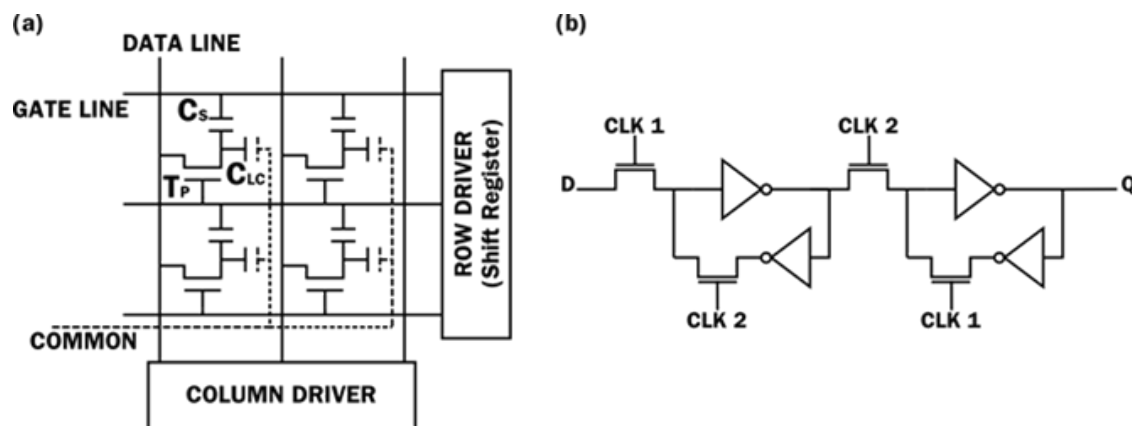


Figure 1.1: Basic circuit diagram for an active matrix liquid crystal display. (a) Each pixel has one switching device (T_P) that is turned on by the row driver circuitry to charge the storage capacitor (C_S) and liquid crystal capacitor (C_{LC}) to the data line voltage. (b) Circuit schematic for one stage of a shift-register, which can be implemented with TFTs or printed MEM switches directly on the display panel.

the performance of printed TFTs has improved steadily with the development of improved printable semiconductor materials, their performance generally is inferior to that of conventional silicon TFTs fabricated by planar processing techniques.

Therefore, printed electronics needs to overcome a barrier in order to be successfully applied to commercialization of flexible electronics: degradation of performance in solution-processed semiconductors. The performance of semiconductor materials depends on the method in which they were deposited on substrate, and the conventional vacuum-deposition method has unmatched performance compared to solution-processed deposition methods. The effective carrier mobility is one of the most important parameters which can be used to characterize TFT performance. Figure 1.2 shows selected values of the highest effective carrier mobility of solution-processed semiconductor polymers reported in the literature in the year between 1986 and 2005 summarized in Ref. [7]. Although there has been tremendous progress in recent years due to active research efforts, it is clear that the devices fabricated using solution-processed materials/methods have performances still inferior to the ones made using the conventional vacuum-deposited method. It is in this context that new switching devices can be a promising alternative to the thin-film transistors.

1.2 Printed Mechanical Switches

In the silicon industry, micro-electro-mechanical systems (MEMS) have been developed to provide superior performance in specific applications over their conventional solid-state counterparts. And recently, they are also gaining attraction as potentially promising alternatives even for digital logic applications, as the incremental benefits from scaling of CMOS tran-

Point No.	Material	Mobility (cm^2/Vs)	Deposition	Reference
1	polythiophene	10^{-5}	s	[8]
2	phthalocyanine	10^{-3}	v	[9]
3	polyacetylene	10^{-4}	s	[10]
4	poly(3-hexylthiophene)	10^{-4}	s	[11]
5	poly(3-hexylthiophene)	0.001	s	[12]
6	$\alpha - \omega$ -hexathiophene	0.001	v	[13]
7	$\alpha - \omega$ -hexathiophene	0.0272	v	[13]
8	pentacene	0.002	v	[14]
9	$\alpha - \omega$ -di-hexyl-hexathiophene	0.05	v	[15]
10	$\alpha - \omega$ -di-hexyl-hexathiophene	0.06	v	[16]
11	$\alpha - \omega$ -hexathiophene	0.03	v	[17]
12	pentacene	0.038	v	[18]
13	C60	0.3	v	[19]
14	phthalocyanine	0.02	v	[20]
15	poly(3-hexylthiophene)	0.045	s	[21]
16	$\alpha - \omega$ -di-hexyl-hexathiophene	0.13	v	[22]
17	pentacene	0.62	v	[23]
18	pentacene	1.5	v	[24]
19	bis(dithienothiophene)	0.05	v	[25]
20	bis(dithienothiophene)	0.1	s	[26]
21	$\alpha - \omega$ -di-hexyl-hexathiophene	0.23	v	[27]
22	dihexyl-anthradithiophene	0.15	v	[28]
23	$\alpha - \omega$ -dihexyl-quinquethiophene	0.1	s	[29]
24	pentacene	3	v	[30]
25	CuPc	0.001	v	[31]
26	PCBM	0.002	s	[32]
27	pentacene	3.3	v	[33]
28	poly(3-hexylthiophene)	0.73	s	[34]
29	PCBM	0.02	s	[35]
30	poly(3-hexylthiophene)	0.1	s	[36]
31	PCBM	0.01	s	[37]
32	C60	6	v	[38]
33	C60MC12	0.06	s	[39]
34	PCBM	0.02	s	[40]
35	thieno[2,3- <i>b</i>]thiophene	0.15	s	[40]

Table 1.1: Reported effective carrier mobility values of solution-processed semiconductor polymers in literature in Fig. 1.2

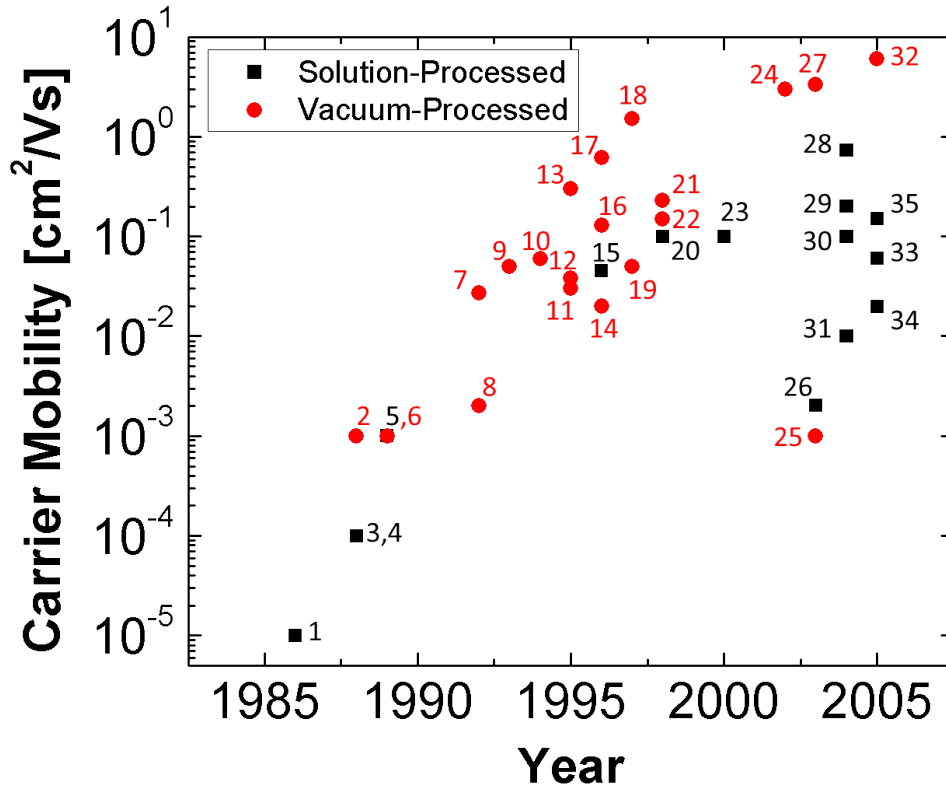


Figure 1.2: Effective carrier mobility values reported in the literature between 1986 and 2005. After Ref. [7]. Indicated numbers on the markers represent the point number in Table 1.1 to find the source data from the References.

sistors are diminishing. MEM relays have been proposed as a lower-power alternative to conventional CMOS devices [41]. A similar approach can be considered in printed electronics, which can be even more beneficial in this case since the performance of the solid-state printed TFTs is not yet matured compared to that of Si-based TFTs. In fact, there has been research on realization of MEM structures using printed technology. The first attempt to develop printed MEMS was made by Fuller and co-workers in 2002 [42], where they introduced the concept of building three-dimensional MEMS using inkjet-printing metal nanoparticles and demonstrated resonant inductive coils, electrostatic-drive motors, and electrothermal actuators. It was the first work on fabrication of printed MEMS. The structures demonstrated were built using additive processes only, without employing any sacrificial materials, although they hinted at the necessity of using a sacrificial layer. After their promising initial work, research on developing the fabrication process of printed MEMS was carried out by many other groups. Wilhelm and co-workers demonstrated actuators fabricated using

an offset liquid embossing technique [43]. Although this was not done using inkjet printing techniques, solution-processed nanoparticles were used as a structural material together with polyimide, which also acted as a sacrificial material. Nakano and co-workers have employed inkjet-printing to fabricate MEM switches [44], where they inkjet-printed silver nanoparticles as signal and control electrodes on a polyimide substrate. Via-holes were formed by a punching machine and two separate terminals were prepared and attached together using adhesive to form a cantilever-type switch. The structures are flexible due to plastic materials (polyimide and parylene) employed as a substrate and structural layer. A similar approach has been employed to fabricate complementary MEM switches from the same research group [45], where a cantilever-type polyimide beam can be electrostatically actuated by two actuating electrodes (bias and ground electrode). The demonstrated printed MEM switch was targeted to act as a complementary digital logic device and inverter operation was successfully performed at 60 V with switching delays in the range of few milliseconds. The large operating voltage and switching delay come from the fact the actuation gap was defined by thick adhesive ($\sim 12 \mu\text{m}$), which was used to stack multiple terminals together manually. Although these works suggest that building three-dimensional structures using solution-processed nanoparticles and polymer can be achievable by printing, anchor formation was done manually using adhesives, which may limit processability. More recently, Lam and co-workers demonstrated a cantilever structure fabricated using inkjet-printed silver nanoparticles as a structural material and Poly(methyl methacrylate) (PMMA) as a sacrificial material [46]. Both the silver nanoparticles and PMMA were inkjet-printed, where the PMMA was patterned into a “mold” structure so that the printed silver inks can be confined inside. A cantilever-beam structure was successfully obtained after trimming out “undesired rims” formed across the PMMA barrier using a laser milling tool. This laser milling process was further employed to define finer patterns such as holes and flexures, and an accelerometer structure was implemented. It is a meaningful result in that it demonstrated the cantilever structure was successfully fabricated from solution-processed materials. However, they had to rely on laser trimming to define the cantilever beam after the completion of printing. Moreover, the cantilever structure did not have an actuation component to achieve any functionality.

All of the previous works on fabrication of printed MEMS form the basis for the work in this dissertation. The purpose of this work is to develop a fabrication process to build electrically functional MEM switches using inkjet-printing technique with precisely defined structures such as a controlled actuation gap size and a controlled shape of the cantilever beam.

1.3 Microshell Encapsulation

As stated earlier in this chapter, MEM relays can be a promising alternative to transistors for low-power logic device applications. Previously, MEM relays were fabricated using conventional surface micromachining processes [41]. Figure 1.3 shows an example of this type of

MEM relay device. The movable gate electrode, suspended by folded-flexure beams, can be electrostatically actuated so that the channel electrode attached on the bottom of the gate can connect the source/drain electrode electrically when the relay is turned on (Fig. 1.3(c)). In the OFF-state, the channel is separated from the source/drain electrode via air gap and thus no leakage current flows (Fig. 1.3(b)). This provides ideal abrupt switching behavior which is beneficial in terms of power consumption since OFF-state leakage current can be effectively suppressed.

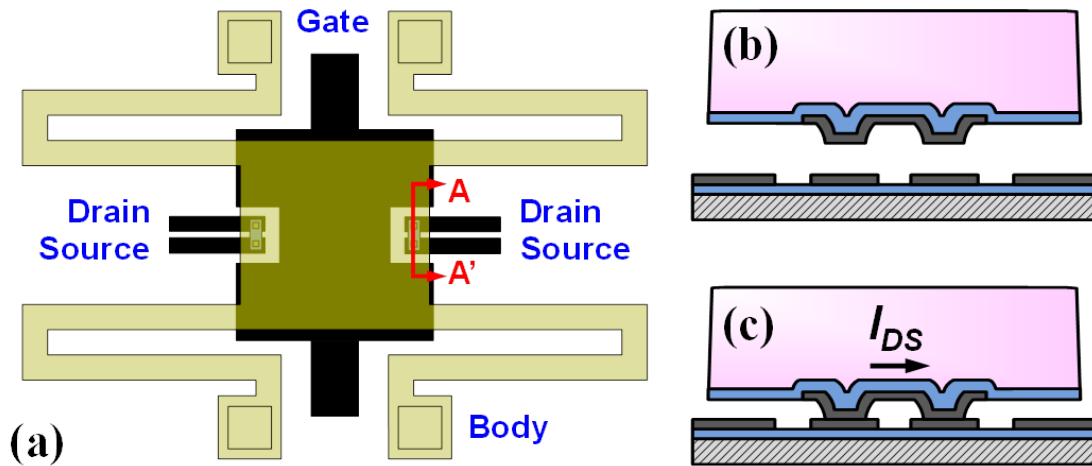


Figure 1.3: Schematic illustration of an example of MEM relay device.

The contacting electrode (channel and source/drain electrodes) material is tungsten (W) to take advantage of its mechanical hardness, which reduces physical wear and micro-welding during the operation of the relays. A drawback of using W as contacting material comes from the fact that it oxidizes easily in the presence of oxygen, and its electrical conductivity severely degrades once it is oxidized in the course of switching operation. This degrades the performance of the relays since the equivalent resistance of the relay in the ON-state (R_{ON}) should be maintained below $\sim 10\text{ k}\Omega$ in order to be applicable in logic applications. To enhance the contact stability, a hermetic package is required.

In general, MEMS devices have more complex configuration than conventional integrated circuits (IC) devices because they contain mechanical, chemical, or fluidic components in addition to electrical parts. These sensitive components should be properly protected and sometimes sealed in controlled environments, such as high vacuum or oxygen-free ambient, in order for them to perform the intended functions. Therefore, it is important to provide the MEMS devices with proper packaging. It is also important to consider the cost efficiency when developing MEMS packaging, since it may take 50 - 70% of total cost for commercial MEMS products [47] due to its nature of low volume production and complex interface to non-electrical components. Although some packaging technologies can be adopted from IC counterparts, a different approach is often necessary in order to treat MEMS-specific

non-electrical components. MEMS packaging technology can be categorized into two types: zero-level packaging and first-level packaging [48]. Zero-level packaging, also known as wafer-level packaging, is a process scheme where packaging can be applied monolithically with device fabrication. Since it is applied as part of the integrated fabrication process, devices can be protected from possible damage or contamination that can occur at subsequent processing steps, which provides for flexibility in post-processing. On the other hand, first-level packaging process starts after the device fabrication has been completed. This scheme can be applied to a wide range of MEMS device structures because of its post-processing nature, which is beneficial in terms of general applicability. Since the components of the packaging chip, for example, ceramic holder and sealing lid, are relatively expensive, the cost of this type of packaging can be justified only for certain applications, such as telecommunications base stations, satellites and defense systems [48].

1.4 Printed Microshell Encapsulation

In this thesis, a fabrication process was developed to provide MEMS devices with microshell encapsulation packaging, one type of zero-level packaging, using inkjet printing. Inkjet-printed nanoparticle films have been employed to as the structural and sealing layers for microshell encapsulation. Advantages of using inkjet-printing technology in packaging applications stem from its inherent low-temperature and low-cost process. Considering that packaging may account for a large portion of the process cost in MEMS, cost-effective processing is a great benefit. Since the packaging process is applied at the end of the MEMS device fabrication, it is also beneficial to be able to lower the process temperature to minimize any accidental impact on the completed MEMS devices from thermal treatment. Sintering of printed nanoparticle films can be performed at relatively low temperature, usually between 100°C and 300°C, due to its enhanced surface-to-volume ratio [49], so that a packaging process employing printed nanoparticle films can be CMOS-compatible.

Specifically, one of the important process requirements in microshell encapsulation package is the property of the structural layers. The structural layer should be permeable to the selected etchant since the encapsulated sacrificial material must be removed after the structural layer is deposited to cover them. The structural material should also provide sufficient mechanical strength to avoid structural collapse after the sacrificial layer is removed and cavity is formed. On the other hand, the structural layer should be dense enough to prevent sealant from penetrating through the structural layer and being deposited on the encapsulated devices, which can accidentally alter electrical or mechanical behavior of the packaged devices. In this thesis, it will be shown that the printed nanoparticle films can satisfy these rather strict requirements for the microshell materials by demonstrating that the developed printed microshell encapsulation process can be successfully integrated to MEM relays and their contact stability can be enhanced.

1.5 Dissertation Outline

In Chapter 2, basic principles required to study inkjet-printing technology and MEM structures are presented.

In Chapter 3, inkjet-printed micro-electro-mechanical (MEM) switches are presented that can deliver abrupt switching characteristics, very low on-state resistance ($\sim 10 \Omega$), and nearly perfect off-state behavior with on/off current ratio of 10^7 , which can be used to implement complementary logic functions. The devices are fabricated using a novel process scheme to build 3-dimensional cantilever structures from solution-processed metallic nanoparticles and sacrificial polymers. These printed MEM switches thus represent a uniquely attractive path for realizing printed electronics.

In Chapter 4, further optimizations of the printed MEM switch process are presented in order to reduce the power consumption of the device and to suppress performance variations. Reducing the operating voltage by scaling the device is of interest in this regard, which may also lead to a broader range of applications. More in depth study on the process would be necessary for this purpose. In this chapter, various process-related issues are studied to further optimize both the process and the performance of the device.

In Chapter 5, a low-thermal budget ($< 300^\circ\text{C}$) microshell encapsulation process using inkjet-printed nanoparticle inks is presented. For microshell encapsulation applications, it is advantageous that the porosity of such printed nanoparticle films can be controlled by the size and structure of the nanoparticles and sintering conditions. Furthermore, the sintering temperature is usually low enough such that the entire process is CMOS compatible.

In Chapter 6, the inkjet-printed microshell encapsulation described in Chapter 5 is employed to provide MEM relays with a hermetic package for improved contact stability. The CMOS-compatible process (due to its low thermal budget) has successfully been applied and the MEM relay contact resistance stability was enhanced by $\sim 100\times$.

Chapter 7 summarizes the key results and contributions of this dissertation; future directions are also suggested.

Bibliography

- [1] Ernst Lueder. *Liquid Crystal Displays: addressing schemes and electro-optical effects*. Ed. by Anthony C. Lowe. Chichester: John Wiley & Sons, Ltd, 2001.
- [2] Joseph A. Castellano. *Liquid Gold: The story of liquid crystal displays and the creation of an industry*. Singapore: World Scientific Publishing, Co. Pte. Ltd., 2005.
- [3] Cyril Hilsun. “Flat-panel electronic displays: a triumph of physics, chemistry and engineering”. In: *Philosophical Transactions of the Royal Society A: Mathematical, Physical and Engineering Sciences* 368 (1914) (Mar. 2010), pp. 1027–1082.
- [4] Yusaku Kato et al. “A large-area, flexible, ultrasonic imaging system with a printed organic transistor active matrix”. In: *2008 IEEE International Electron Devices Meeting* (Dec. 2008), pp. 1–4.
- [5] H E A Huitema et al. “Active-Matrix Displays Driven by Solution-Processed Polymeric Transistors”. In: *Advanced Materials* 14 (17) (Sept. 2002), pp. 1201–1204.
- [6] H. Sirringhaus et al. “34.1: Active Matrix Displays Made with Printed Polymer Thin Film Transistors”. In: *SID Symposium Digest of Technical Papers* 34 (1) (2003), p. 1084.
- [7] Th. Birendra Singh and Niyazi Serdar Sariciftci. “PROGRESS IN PLASTIC ELECTRONICS DEVICES”. In: *Annual Review of Materials Research* 36 (1) (June 2006), pp. 199–230.
- [8] A Tsumura, H Koezuka, and T Ando. “Macromolecular electronic device: Field-effect transistor with a polythiophene thin film”. In: *Applied Physics Letters* 49 (18) (Nov. 1986), pp. 1210–1212.
- [9] C Clarisse et al. *Field-effect transistor with diphthalocyanine thin film*. 1988.
- [10] J H Burroughes, C A Jones, and R H Friend. “New semiconductor device physics in polymer diodes and transistors”. In: *Nature* 335 (6186) (Sept. 1988), pp. 137–141.
- [11] A Assadi et al. “Field-effect mobility of poly(3-hexylthiophene)”. In: *Applied Physics Letters* 53 (3) (July 1988), pp. 195–197.
- [12] J Paloheimo et al. “Lower Dimensional Systems and Molecular Devices”. In: *Proceedings of NATO ASI*. New York: Plenum Press, 1989.
- [13] Gilles Horowitz et al. “A field-effect transistor based on conjugated alpha-sexithienyl”. In: *Solid State Communications* 72 (4) (Oct. 1989), pp. 381–384.

- [14] Gilles Horowitz et al. "Role of the semiconductor/insulator interface in the characteristics of π -conjugated-oligomer-based thin-film transistors". In: *Synthetic Metals* 51 (1-3) (Sept. 1992), pp. 419–424.
- [15] Francis Garnier et al. "Molecular engineering of organic semiconductors: design of self-assembly properties in conjugated thiophene oligomers". In: *Journal of the American Chemical Society* 115 (19) (Sept. 1993), pp. 8716–8721.
- [16] Francis Garnier et al. "All-Polymer Field-Effect Transistor Realized by Printing Techniques". In: *Science* 265 (5179) (Sept. 1994), pp. 1684–1686.
- [17] L Torsi et al. "Intrinsic Transport Properties and Performance Limits of Organic Field-Effect Transistors". In: *Science* 272 (5267) (June 1996), pp. 1462–1464.
- [18] C D Dimitrakopoulos, A R Brown, and A Pomp. "Molecular beam deposited thin films of pentacene for organic field effect transistor applications". In: *Journal of Applied Physics* 80 (4) (Aug. 1996), pp. 2501–2508.
- [19] J Kastner, J Paloheimo, and H Kuzmany. "Fullerene Field-Effect Transistors". English. In: *Electronic Properties of High-Tc Superconductors SE - 89*. Ed. by Hans Kuzmany, Michael Mehring, and Jörg Fink. Vol. 113. Springer Series in Solid-State Sciences. Springer Berlin Heidelberg, 1993, pp. 512–515.
- [20] Zhenan Bao, Andrew J Lovinger, and Ananth Dodabalapur. "Organic field-effect transistors with high mobility based on copper phthalocyanine". In: *Applied Physics Letters* 69 (20) (Nov. 1996), pp. 3066–3068.
- [21] Zhenan Bao, Ananth Dodabalapur, and Andrew J Lovinger. "Soluble and processable regioregular poly(3-hexylthiophene) for thin film field-effect transistor applications with high mobility". In: *Applied Physics Letters* 69 (26) (Dec. 1996), pp. 4108–4110.
- [22] Christos D Dimitrakopoulos et al. "Field-effect transistors comprising molecular beam deposited α,ω -di-hexyl-hexathienylene and polymeric insulator". In: *Synthetic Metals* 92 (1) (Jan. 1998), pp. 47–52.
- [23] Y-Y Lin, D J Gundlach, and T N Jackson. *High-mobility pentacene organic thin film transistors*. 1996.
- [24] Y-Y Lin et al. *Stacked pentacene layer organic thin-film transistors with improved characteristics*. 1997.
- [25] H Sirringhaus et al. "Bis(dithienothiophene) organic field-effect transistors with a high ON/OFF ratio". In: *Applied Physics Letters* 71 (26) (Dec. 1997), pp. 3871–3873.
- [26] Henning Sirringhaus, Nir Tessler, and Richard H Friend. "Integrated Optoelectronic Devices Based on Conjugated Polymers". In: *Science* 280 (5370) (June 1998), pp. 1741–1744.

- [27] Howard E Katz, Andrew J Lovinger, and Joyce G Laquindanum. " α,ω -Dihexylquaterthiophene :A Second Thin Film Single-Crystal Organic Semiconductor". In: *Chemistry of Materials* 10 (2) (Jan. 1998), pp. 457–459.
- [28] Joyce G Laquindanum, Howard E Katz, and Andrew J Lovinger. "Synthesis, Morphology, and Field-Effect Mobility of Anthradithiophenes". In: *Journal of the American Chemical Society* 120 (4) (Jan. 1998), pp. 664–672.
- [29] H E Katz et al. "A soluble and air-stable organic semiconductor with high electron mobility ". In: *Nature* 404 (6777) (Mar. 2000), pp. 478–481.
- [30] Marcus Halik et al. "Fully patterned all-organic thin film transistors". In: *Applied Physics Letters* 81 (2) (July 2002), pp. 289–291.
- [31] Jason Locklin et al. "Ambipolar Organic Thin Film Transistor-like Behavior of Cationic and Anionic Phthalocyanines Fabricated Using Layer-by-Layer Deposition from Aqueous Solution". In: *Chemistry of Materials* 15 (7) (Mar. 2003), pp. 1404–1412.
- [32] C Waldauf et al. "Solution-Processed Organic n-Type Thin-Film Transistors". In: *Advanced Materials* 15 (24) (Dec. 2003), pp. 2084–2088.
- [33] Tommie Wilson Kelley et al. "High-Performance OTFTs Using Surface-Modified Alumina Dielectrics". In: *The Journal of Physical Chemistry B* 107 (24) (May 2003), pp. 5877–5881.
- [34] B H Hamadani and D Natelson. "Temperature-dependent contact resistances in high-quality polymer field-effect transistors". In: *Applied Physics Letters* 84 (3) (Jan. 2004), pp. 443–445.
- [35] Th. B Singh et al. "Fabrication and characterization of solution-processed methanofullerene-based organic field-effect transistors". In: *Journal of Applied Physics* 97 (8) (Apr. 2005), pp. 83714–83715.
- [36] Guangming Wang et al. "Fabrication of regioregular poly(3-hexylthiophene) field-effect transistors by dip-coating". In: *Synthetic Metals* 146 (2) (Oct. 2004), pp. 127–132.
- [37] T.D. Anthopoulos et al. "Ambipolar Organic Field-Effect Transistors Based on a Solution-Processed Methanofullerene". In: *Advanced Materials* 16 (23-24) (Dec. 2004), pp. 2174–2179.
- [38] Th. B Singh et al. "Enhanced Mobility of Organic Field-Effect Transistors with Epitaxially Grown C60 Film by in-situ Heat Treatment of the Organic Dielectric". In: *MRS Online Proceedings Library*. Vol. 871. 2005.
- [39] Masayuki Chikamatsu et al. "Solution-processed n-type organic thin-film transistors with high field-effect mobility". In: *Applied Physics Letters* 87 (20) (Nov. 2005), pp. 203503–203504.
- [40] Martin Heeney et al. "Stable Polythiophene Semiconductors Incorporating Thieno[2,3-b]thiophene". In: *Journal of the American Chemical Society* 127 (4) (Jan. 2005), pp. 1078–1079.

- [41] Tsu-Jae King Liu et al. “Prospects for MEM logic switch technology”. In: *Electron Devices Meeting (IEDM), 2010 IEEE International*. 2010, pp. 18.3.1–18.3.4.
- [42] S.B. Fuller, E.J. Wilhelm, and J.M. Jacobson. “Ink-jet printed nanoparticle microelectromechanical systems”. In: *Journal of Microelectromechanical Systems* 11 (1) (2002), pp. 54–60.
- [43] Eric J. Wilhelm, Brian T. Neltner, and Joseph M. Jacobson. “Nanoparticle-based microelectromechanical systems fabricated on plastic”. In: *Applied Physics Letters* 85 (26) (Dec. 2004), pp. 6424–6426.
- [44] Shintaro Nakano et al. “Low operation voltage of inkjet-printed plastic sheet-type micromechanical switches”. In: *Applied Physics Letters* 92 (5) (Feb. 2008), pp. 053302–3.
- [45] Tomoyuki Yokota et al. “Plastic complementary microelectromechanical switches”. In: *Applied Physics Letters* 93 (2) (2008), p. 023305.
- [46] E W Lam, H Li, and M A Schmidt. “SILVER NANOPARTICLE STRUCTURES REALIZED BY DIGITAL SURFACE MICROMACHINING Microsystems Technology Laboratories Massachusetts Institute of Technology , Cambridge , Massachusetts , USA”. In: *Transducers 2009* (2009), pp. 1698–1701.
- [47] H. Reichl and V. Grosser. “Overview and development trends in the field of MEMS packaging”. In: *Technical Digest. MEMS 2001. 14th IEEE International Conference on Micro Electro Mechanical Systems (Cat. No.01CH37090)*. IEEE, pp. 1–5.
- [48] Stepan Lucyszyn. *Advanced RF MemS*. Cambridge University Press, 2010.
- [49] Ph. Buffat and J-P. Borel. “Size effect on the melting temperature of gold particles”. In: *Physical Review A* 13 (6) (1976), pp. 2287 –2289.

Chapter 2

Physical Background

2.1 Basic Principles of Inkjet Printing

Inkjet printing technology has experienced a great amount of progress in recent years, especially as a novel method for fabrication of electrical components. Accumulated knowledge through active research enabled deeper understanding and developing of printed electronics. In this section, the basic principles of inkjet printing technology are addressed to understand the underlying operation of inkjet printing technology, which was used as a main vehicle to realize devices and structures in this dissertation.

Inkjet printing is one of several printing technologies that can be used as an additive fabrication technology using solution-processed materials. The target of the inkjet printing is to deposit the selected material onto a substrate with required precision in a reliable way.

2.1.1 Drop-on-Demand Nozzle

There are largely two types of nozzles used for drop-on-demand (DOD) type of inkjet printing, where drops were generated and jetted when necessary as opposed to making a continuous flow of droplets. Thermal inkjet (TIJ) nozzle employs a resistive heating element that is in contact with the liquid ink in order to thermally generate a bubble nearby, which in turn induces volume expansion of the liquid ink inside the nozzle [1, 2] (See Figure 2.1(a)). It is relatively straightforward to fabricate this type of nozzles since the required resistive heater can be made using a conventional multi-layer process using standard surface micro-machining techniques. The drawbacks of TIJ nozzles come from the fact that the solvent of the ink needs to be heat-compatible, which may limit the range of solvent that can be used. For example, most bio-compatible materials are not able to endure such thermal treatment. Piezoelectric nozzles, on the other hand, exploit mechanical expansion controlled electrically and control the volume of the nozzle by applying a voltage pulse signal [3, 4] (See Figure 2.1(b)). Therefore, it allows more flexibility in solvent choice, which made it become dominant in inkjet printing. Droplet formation process will be described in the following section, for the case of the piezoelectric nozzle.

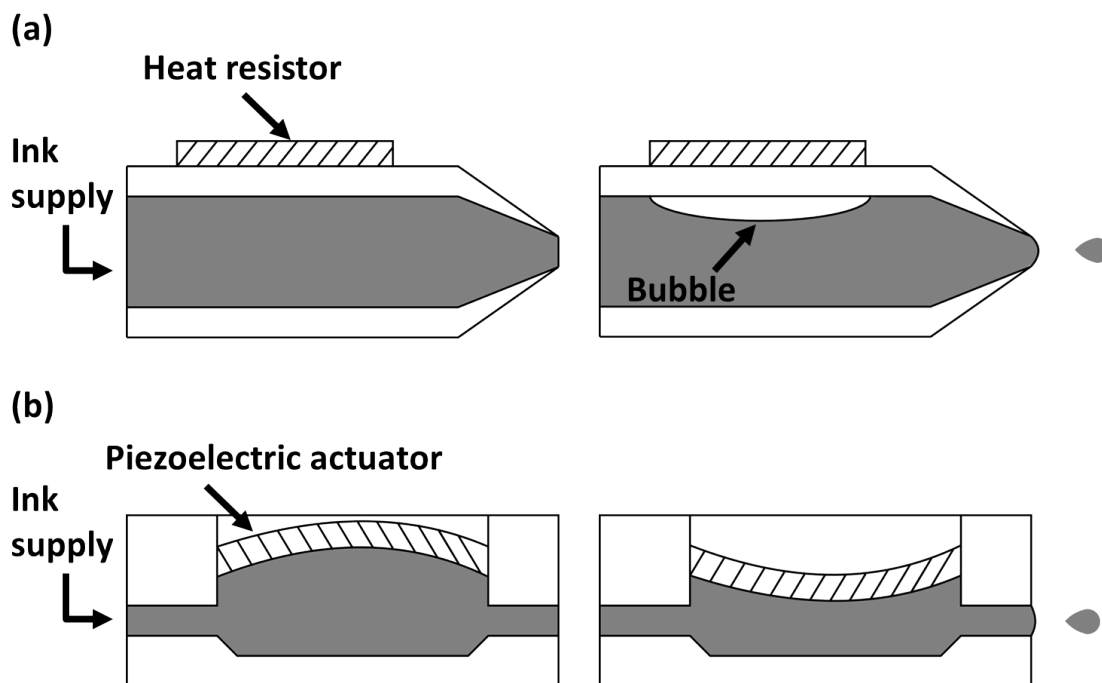


Figure 2.1: Schematic illustration of drop-on-demand nozzles. (a) Thermal inkjet (TIJ) nozzle employs a resistive heating element that is in contact with the liquid ink in order to thermally generate bubbles nearby, which in turn induces volume expansion of the liquid ink inside the nozzle. (b) Piezoelectric nozzles exploit mechanical expansion controlled electrically and control the volume of the nozzle by applying a voltage pulse signal. Figures drawn after Ref. [2] and [4], respectively.

2.1.2 Drop Formation

The drop formation consists of different steps, which incorporate the transfer of energy from the liquid inside the nozzle to the generated drop. The basic principles of the droplet formation are briefly described here.

A schematic diagram illustrating the drop formation process steps in sequence as a response to the applied voltage pulse on the nozzle is shown in Fig. 2.2 [5]. The liquid inside the nozzle remains in an equilibrium state before voltage is applied to the piezoelectric actuator (Fig. 2.2(a)). Upon applying a positive voltage pulse, the liquid starts to flow out of the nozzle due to the volume contraction of the nozzle (Fig. 2.2(b)). Kinetic energy transferred from the inside of the nozzle keeps accumulating at the extruded volume of the liquid on the outside of the nozzle (Fig. 2.2(c)). A droplet is then separated from this volume of liquid upon the accumulated energy increasing beyond a threshold value, and the energy is transferred into both kinetic energy and surface energy of this newly generated droplet (Fig. 2.2(d)). The generated droplet flies to the substrate, while the remaining liquid now re-

tracts into the nozzle as a response to the negative voltage pulse (Fig. 2.2(e)). It is important to optimize the positive pulse duration such that the positive pulse ends at the point when the maximum velocity is obtained. An excessive value of positive pulse duration may cause generation of multiple droplets, rather than a single one, or formation of air bubbles during the retraction process. Next, refilling of the nozzle from the ink supply occurs. Figure 2.3 shows a micrograph of drop formation from the piezoelectric nozzles used in this work.

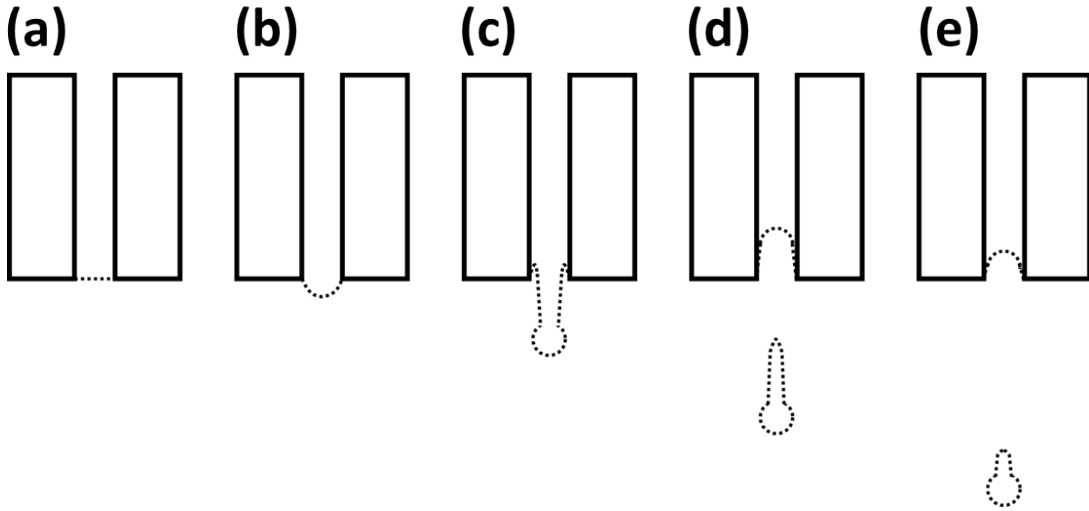


Figure 2.2: Schematic illustration of the drop formation process steps in sequence. (a) The liquid inside the nozzle remains in equilibrium state. (b) Upon applying positive voltage pulse, the liquid starts to flow out of the nozzle due to the volume contraction of the nozzle. (c) Kinetic energy transferred from the inside of the nozzle accumulates in the extruded volume of the liquid on the outside of the nozzle. (d) A droplet is separated from the liquid when the accumulated energy increases beyond a threshold value, and the energy is transferred into both kinetic energy and surface energy of this newly generated droplet. (e) The generated droplet flies to the substrate, while the remaining liquid now retracts into the nozzle in response to the negative voltage pulse. Figure is drawn after Ref. [5].

The physical properties that determine the formation and jetting of the droplets are surface tension, viscosity, and inertia of the liquid ink. Various dimensionless parameters have been defined to take into account of effects on the fluid from these properties; Reynolds number Re , Weber number We , and Ohnesorge number Oh are defined as follows.

Reynolds number was developed to relate inertia and viscous force, defined as:

$$Re = \frac{\rho d V}{\eta} \quad (2.1)$$

where ρ is the density, V is velocity, η is viscosity of the fluid, and d is a characteristic length. The Weber number relates inertia and surface tension, defined as:

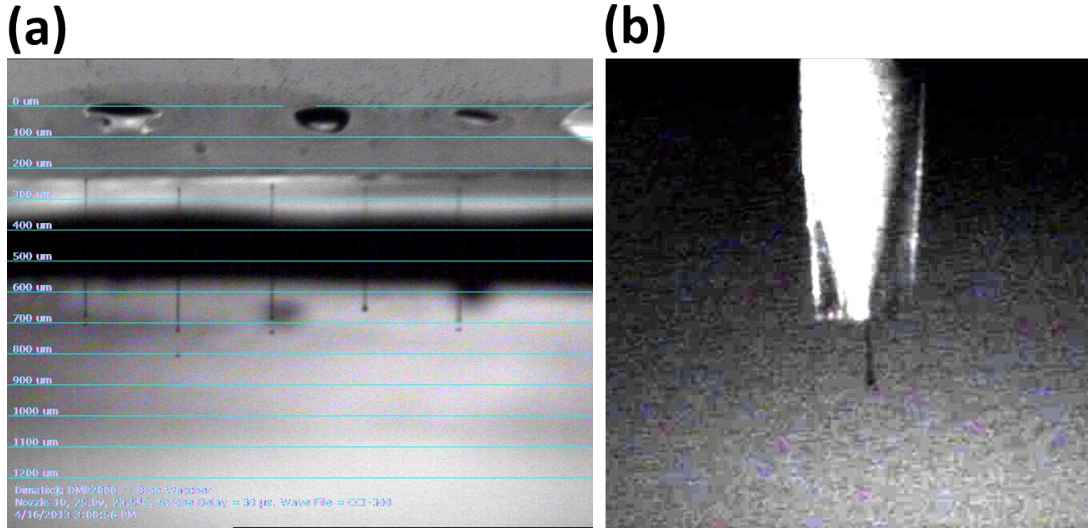


Figure 2.3: Micrographs of drop formation from the piezoelectric nozzles used in this work. (a) Dimatix Cartridge (FujiFilm) and (b) Microfab nozzle

$$We = \frac{\rho d V^2}{\sigma} \quad (2.2)$$

where σ is the surface tension. Finally, the Ohnesorge number can be defined using these two numbers to eliminate the effect of velocity:

$$Oh = \frac{\sqrt{We}}{Re} = \frac{\eta}{\sqrt{\sigma \rho d}} \quad (2.3)$$

Therefore, Oh can be used to characterize the jetting/formation of the droplet based on the physical properties only, independent of the dynamic condition in which the droplet is generated or moving. Large value of Ohnesorge number ($Oh > 1$) represents the case where the behavior of the fluid is dominated by viscosity and droplet generation can be hindered by large viscous force. On the other hand, small value of Ohnesorge number ($Oh < 0.1$) represents the case where drop formation may become unstable due to excessive generation of satellite droplets. In some cases, the inverse of Ohnesorge number $Z = 1/Oh$ is used to characterize the formation or behavior of droplets [6].

2.1.3 Reliability of Nozzles

It is important for the nozzles to generate droplets in a reliable and stable manner. The physical properties of the generated droplets, such as size and velocity, should be controlled to be consistent during operation. Additionally, the nature of the DOD nozzle implies that there is an idle period when the nozzle is not generating any droplets even during the

operation, and therefore it is necessary to have some methods to keep the nozzle in a stable condition to avoid a failure in jetting (See Figure 2.4).

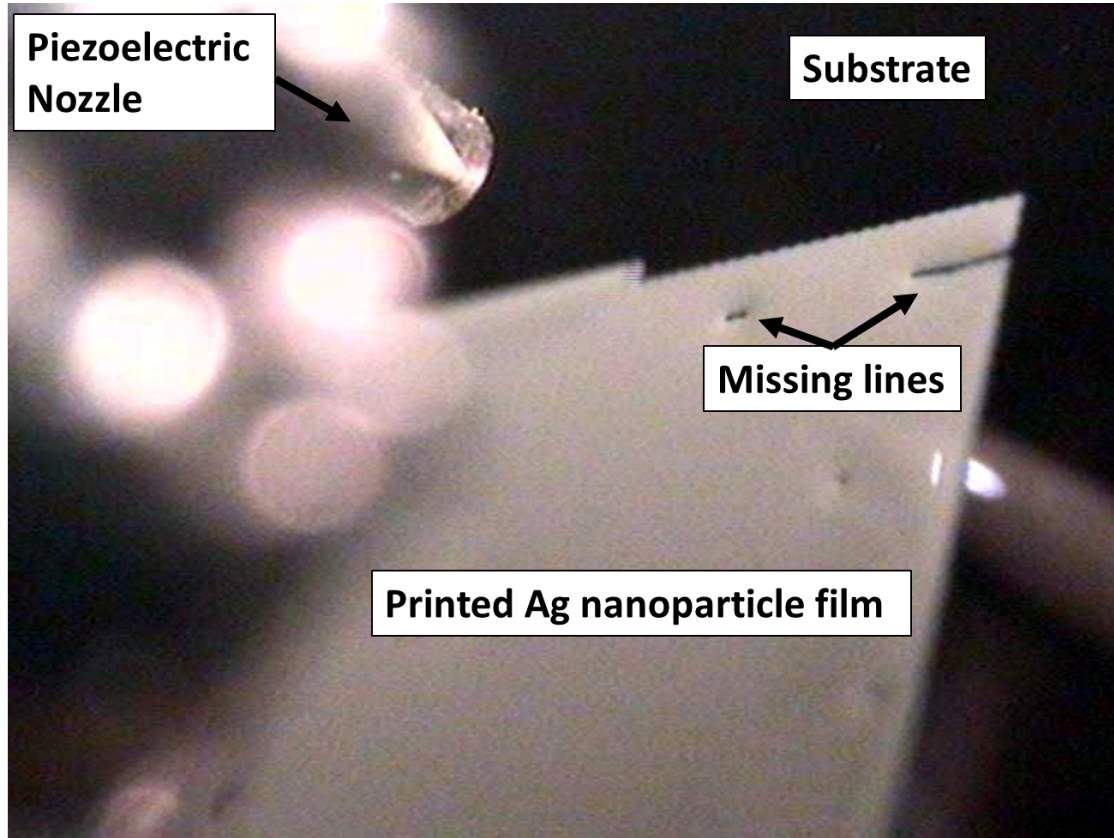


Figure 2.4: Micrograph of a piezoelectric nozzle printing a pattern with missing lines due to jet instability.

2.1.4 Contact Angle

The jetted drop flies to the substrate and makes a contact with a substrate. Upon making a contact with a solid substrate, the liquid forms its shape to minimize its energy. It is after three important forces balance out that the liquid is stabilized to reach an equilibrium contact angle (θ_E); the surface energy between the liquid and the vapor environment (γ_{LV}), the surface energy between the solid substrate and the vapor environment (γ_{SV}), and the surface energy between the liquid and the solid substrate (γ_{LS}) (See Fig. 2.5). The balance among these surface energies can be represented by the Young equation [7] through θ_E :

$$\gamma_{SV} = \gamma_{LS} + \gamma_{LV} \cos \theta_E \quad (2.4)$$

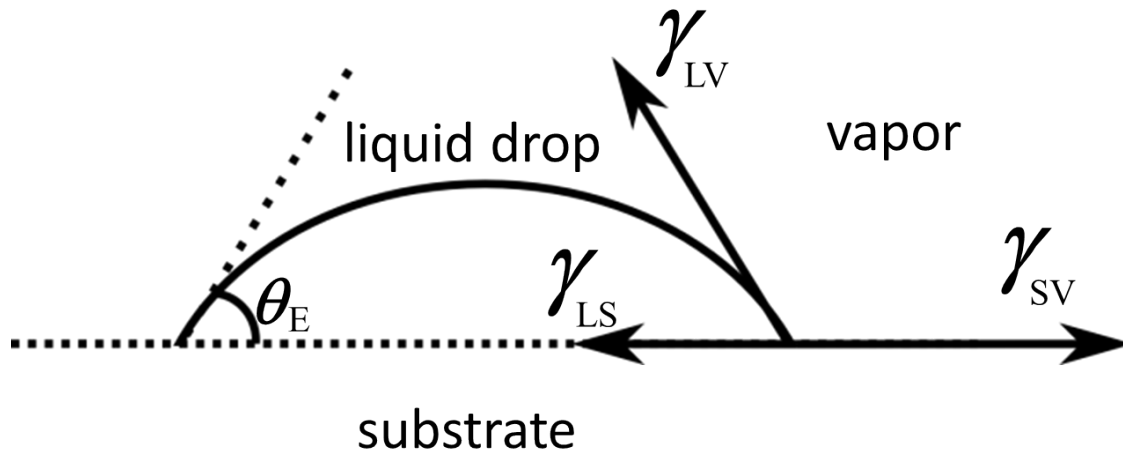


Figure 2.5: Schematic illustration of force balance for a droplet in equilibrium.

The wetting of a liquid on a substrate is often characterized by the contact angle, θ_E , that forms between the droplet and the substrate; a hydrophobic surface has a tendency to repel a water droplet and to form a larger contact angle ($\theta_{E,\text{water}} > 90^\circ$), while a water droplet on a hydrophilic surface tends to spread and have smaller contact angle ($\theta_{E,\text{water}} < 90^\circ$).

The contact angle can be measured experimentally using various methods [8]; optical reflectometry, interference microscopy, or sessile drop method using goniometer. Figure 2.6 shows an example of the contact angle measurement using a goniometer (KRUSS contact angle analyzer), where a water droplet was deposited on a selected substrate (PMMA, in this case) while the side-view image was taken by attached camera. The contact angle can be determined by analyzing the micrograph using image processing software by fitting the outline of the droplet.

2.1.5 Coffee-Ring Effect

An important physical phenomenon that has a great impact on printed features is the so-called “coffee-ring effect”. It manifests itself in a coffee stain on the table after spilt drop of coffee (or any solution containing suspended particles) has been evaporated. Its importance in printed electronics comes from the fact that the printed features may have a non-uniform surface topology after the patterned liquid ink dries. Deegan and co-workers have reported a model to quantify this coffee-ring effect using concepts of the capillary flow and contact line pinning in Ref. [9]. Once a liquid on a solid substrate reaches equilibrium and contact line pinning occurs [10], the contact line retraction starts as liquid evaporates. Initially, the contact area remains constant because the contact line is fixed while the solvent evaporates,

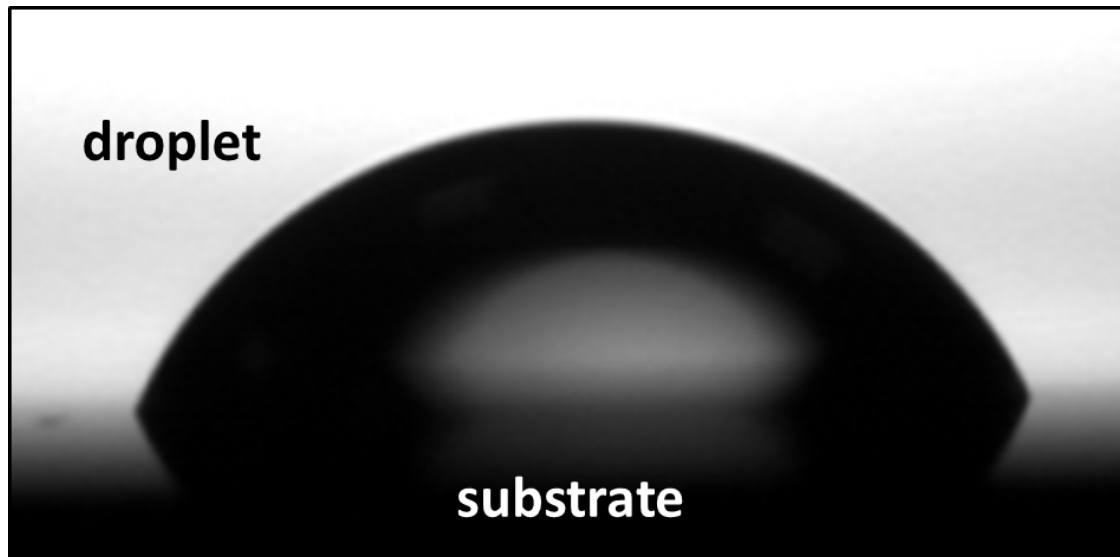


Figure 2.6: Micrograph of contact angle measurement using a goniometer.

which causes radial flow outward to replenish the evaporated liquid at the pinned perimeter. This radial flow carries solutes outward and stacks the solute so that a thick layer along the perimeter is created. During this stage, the contact angle decreases as the volume of the liquid is reduced due to solvent evaporation. When the contact angle becomes smaller than the receding contact angle, the contact line will recede and the contact area is reduced. More recently, further studies found that the shape of suspended particles (solutes) [11] or pH of solvent [12] may impact this phenomenon.

Depending on the intended application, the coffee-ring structure may be something to avoid or exploit. In general, it is an obstacle in building 3-dimensional structures using multi-layer processes because it can create a rather thick barrier, which makes it difficult to form a connection between two regions separated by such a barrier.

2.2 Mechanical/Electrical Modeling of A Cantilever-Beam

Since one of the main topics in this dissertation is to implement mechanical structures using aforementioned inkjet-printing technology, it is good to be equipped with some basic knowledge to understand and analyze behaviors of such micro-electro-mechanical devices. In this section, basic principles required to model electrostatically actuated cantilever structures are addressed.

2.2.1 Spring Constant

The behavior of a cantilever beam structure can be understood by modeling the movable beam as a spring. For example, the vertical displacement of the beam at the free end upon an applied load can be modeled as the displacement of the spring in response to an external force. The relation between the displacement (z) and the applied force (F) follows Hookes law $F = kz$, where k is the linear spring constant, granted that the force is such that z is limited to small deflection of the beam.

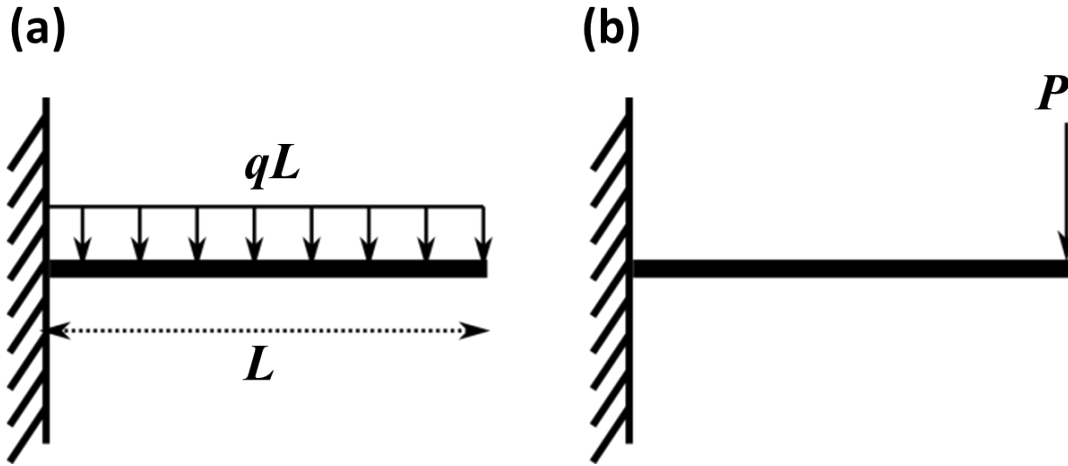


Figure 2.7: Schematic diagrams illustrate different types of loading on the cantilever beam. (a) Uniformly distributed load and (b) a point load at the free end of the cantilever beam.

It should be noted that the effective spring constant of a cantilever beam is a function of a type of applied load. For example, the load q may be uniformly distributed over the entire beam (Fig. 2.7(a)) and the corresponding beam deflection δ_z is given as [13]:

$$\delta_z = \frac{qL^4}{8EI} \quad (2.5)$$

where q is the uniformly distributed load over the beam length L , E is elastic modulus of the beam material, and I is moment of inertia of the beam. The Equation (2.5) can be arranged as follows:

$$qL = \left(\frac{8EI}{L^3} \right) \delta_z = k\delta_z \quad (2.6)$$

Since qL is the effective load and δ_z is the corresponding displacement, the effective spring constant can be obtained as $k = \frac{8EI}{L^3}$. Similarly, a point load P applied on the free end of the beam (Fig. 2.7(b)) causes the beam deflection given as [13]:

$$\delta_z = \frac{PL^3}{3EI} \quad (2.7)$$

which can be rearranged into a form of Hooke's law:

$$P = \left(\frac{3EI}{L^3} \right) \delta_z = k\delta_z \quad (2.8)$$

Then, the corresponding spring constant for this case $k = \left(\frac{3EI}{L^3} \right)$ can be obtained.

The spring constants derived above are valid independent of the shape of the cross-section or material of the beam. If the beam has rectangular cross-section, the moment of inertia is given as $I = WH^3/12$ (W is the width and H is the height of the beam). For a beam of homogeneous material, E is the material's Young's modulus.

2.2.2 Pull-in Mode Operation

Electrostatically actuated micro-electro-mechanical (MEM) switches can be modeled using parallel-plate capacitors, where an electrostatic force exists between the movable beam and an actuating electrode. Figure 2.8 shows an example of a cantilever beam structure, where the cantilever beam is actuated by applying a voltage to the underlying actuating electrode. Upon applying a voltage V on the actuating electrode, the beam is attracted downwards by electrostatic force and eventually stopped by a contacting electrode. The threshold voltage which makes the beam collapse into contact with the contacting electrode is called the pull-in voltage V_{PI} . It can be obtained using a force balance equation between the electrostatic force F_{elec} and the spring restoring force F_{spring} . By modeling this system as a parallel-plate capacitor, F_{elec} is given as:

$$F_{elec} = \frac{\epsilon_0 AV^2}{2(g_0 - z)^2} \quad (2.9)$$

where ϵ_0 is the vacuum permittivity, A is the actuation area (overlap area between the actuation electrode and the beam), g_0 is actuation gap, and z is the beam deflection which increases positively from the equilibrium position to downwards (as shown in z -axis). Following the sign convention defined in Fig. 2.8, $F_{spring} = -kz$, where k is the spring constant of the cantilever beam. The net force applied on the beam is the summation of F_{elec} and F_{spring} :

$$F_{net} = F_{elec} + F_{spring} = \frac{\epsilon_0 AV^2}{2(g_0 - z)^2} - kz = \frac{\epsilon_0 AV^2}{2g^2} - k(g_0 - g) \quad (2.10)$$

where a new variable $g = g_0 - z$ is defined to indicate the gap between the beam and the actuation electrode. There exists a positive feedback in the system when a voltage source (infinite charge pump) is used to actuate the beam, which is the case for most practical MEMS applications. As the applied voltage increases linearly, F_{elec} increases superlinearly with z because capacitance also increases, increasing charge; in contrast, F_{spring} increases only linearly with z . Beyond a certain value of beam deflection, there is no stable equilibrium position for the beam, $F_{elec} > F_{spring}$ so that the beam collapses into contact. The voltage at

which the beam pulls in is defined as the pull-in voltage V_{PI} . Both the gap size at pull-in g_{PI} and V_{PI} can be calculated by inspecting the stability of the net force F_{net} in Equation (2.10). F_{net} can be rearranged without losing its generality as follows [14]:

$$\delta F_{net} = \left. \frac{\partial F_{net}}{\partial g} \right|_V \cdot \delta g \quad (2.11)$$

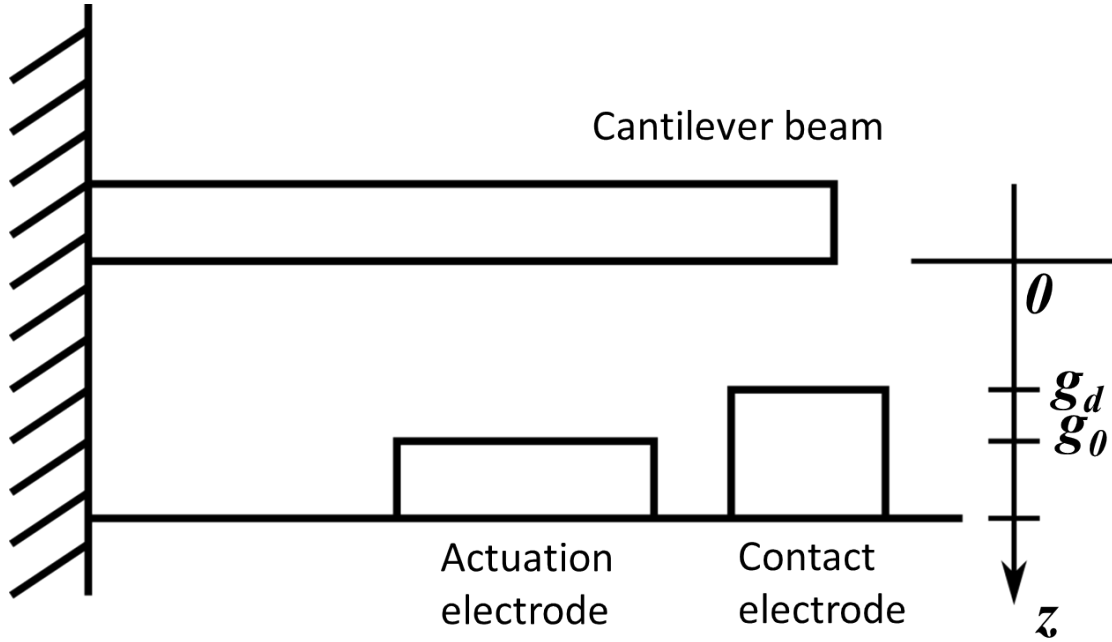


Figure 2.8: Schematic illustration of dimensions used in cantilever beam analysis.

For a small increase of deflection, or equivalently a small decrease of gap ($\delta g < 0$), the condition $\delta F_{net} < 0$ should be satisfied in order to have a stable equilibrium position, otherwise the system is unstable due to the aforementioned positive feedback. Therefore, the condition $\left. \frac{\partial F_{net}}{\partial g} \right|_V > 0$ should be satisfied to have a stable system. At the onset of unstable positive feedback,

$$\left. \frac{\partial F_{net}}{\partial g} \right|_V = -\epsilon_0 AV^2/g^3 + k = 0 \quad (2.12)$$

and the values of g and V which satisfy the above condition are g_{PI} and V_{PI} , respectively:

$$V_{PI} = \sqrt{\frac{kg_{PI}^3}{\epsilon_0 A}} \quad (2.13)$$

By substituting Eq. (2.13) into Eq. (2.10),

$$g_{\text{PI}} = \frac{2}{3}g_0 \quad (2.14)$$

that is, the onset of a positive feedback, or the pull-in mode, occurs when the gap between the beam and the actuating electrode g becomes two-thirds of the initial gap g_0 .

The pull-in phenomenon can also be understood graphically. The forces acting on the beam, F_{elec} and F_{spring} are plotted in Fig. 2.9. The force is normalized to the maximum mechanical force on the beam ($F_{s,\text{max}} = kg_0$) and the displacement is normalized to an initial actuation gap g_0 . When increasing the applied voltage quasi-statically ($V_1 < V_2 < V_3 < V_4$), the beam deflects accordingly and stays in a stable equilibrium point (such as points A and B) where the forces balance $F_{\text{net}} = 0$. Pull-in instability occurs at V_3 (point C), where a small disturbance in displacement results in a positive rate of change of the net force $\left. \frac{\partial F_{\text{net}}}{\partial g} \right|_V > 0$. Therefore, the pull-in voltage is $V_{\text{PI}} = V_3$ and corresponding gap is g_{PI} is about $2/3$ of the initial actuation gap g_0 , as indicated in Fig. 2.9. Increasing the voltage above $V_{\text{PI}} = V_3$ makes the condition $F_{\text{elec}} > F_{\text{spring}}$ always true so that the beam remains in contact with the contacting electrode. On the other hand, when decreasing the applied voltage, the beam may not be released from the contacting electrode at V_{PI} , resulting in a hysteresis. This hysteretic behavior comes from the fact that there are two stable equilibrium points for $V < V_{\text{PI}}$, for example, points B and D are two equilibrium points for $V = V_2$. If we assume the contact gap g_d was defined such that $g_d/g_0 \sim 0.8$, then the condition $F_{\text{elec}} > F_{\text{spring}}$ remains satisfied (so that the beam is deflected to contact the contacting electrode) during the course of decreasing the applied voltage from V_4 to V_2 because the equilibrium point of the beam is located between the point C and D along the normalized force line. Any surface adhesion force F_{adhesion} between the beam and the contact electrode exacerbates this effect. Therefore, the release voltage V_{RL} at which the beam is released from the contact electrode is smaller than V_2 . Balancing the acting forces, F_{elec} , F_{spring} , and F_{adhesion} , V_{RL} can be obtained as follows:

$$\begin{aligned} F_{\text{spring}} &= F_{\text{elec}} + F_{\text{adhesion}} \\ V_{\text{RL}} &= \sqrt{\frac{2(k(g_0 - g_d) - F_{\text{adhesion}})(g_0 - g_d)^2}{\epsilon_0 A}} \end{aligned} \quad (2.15)$$

It should be noted that the location of the actuating electrode defines the applied load on the beam, and the effective spring constant of the beam k should be adjusted accordingly, as seen in the section 2.2.1.

2.3 Nanoindentation

The mechanical properties, in addition to the electrical properties, of a structural beam have significant impact on MEMS device performance. Furthermore, nanoparticles rarely have been used to implement MEMS devices and so it is important to characterize their

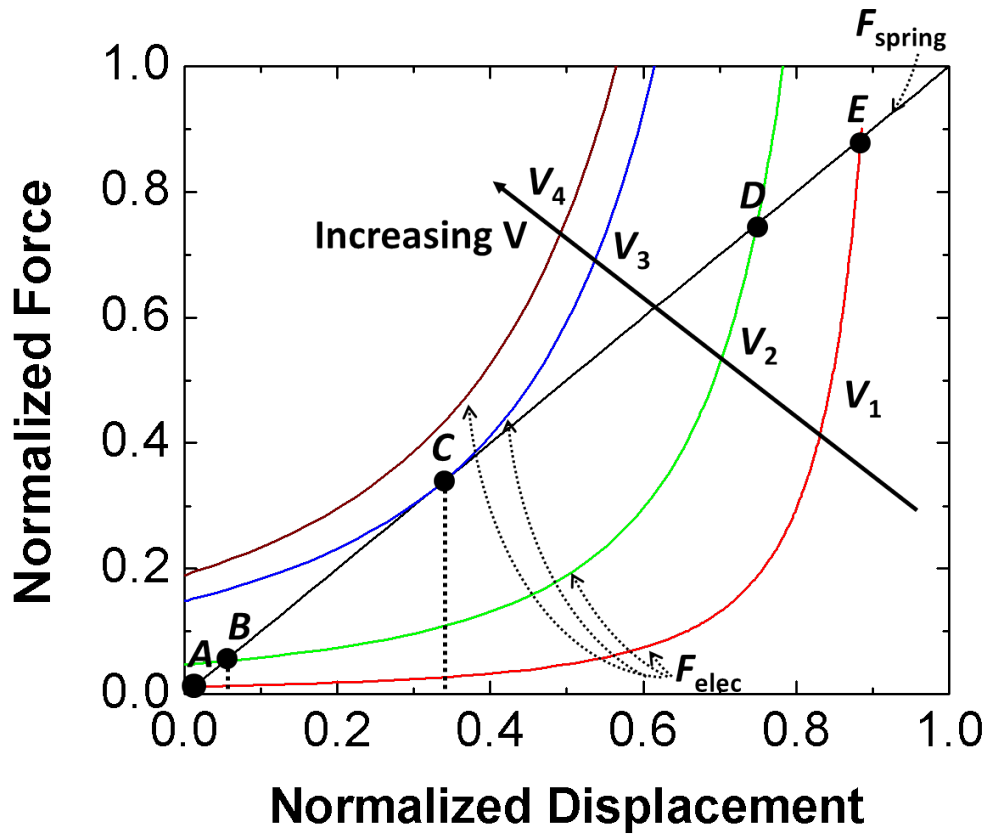


Figure 2.9: Normalized force *vs.* normalized displacement of the cantilever beam. Plot after Ref. [14]

mechanical properties in this dissertation. A method called nanoindentation was employed for this purpose in this work and its basic principle is briefly reviewed in this section.

Nanoindentation was developed to measure the elastic modulus and hardness of a material sample to be studied using an indenter load [15, 16]: the measurement employs a sharp mechanically strong tip of a specific geometry which can be used to make a nano-scale indentation on the surface of the sample while the applied load on the tip and the corresponding displacement of the tip are recorded during the loading and unloading cycle. An example of such a load (P) *vs.* displacement (h) curve is shown in Fig. 2.10. The load P represents the force applied on the indenter and h is the displacement of the indenter with respect to an undeformed surface of the sample. The Oliver-Pharr model [15] was developed by assuming that both elastic and plastic deformation occurs during loading but only elastic displacement occurs in the unloading process. By studying this unloading response, it is possible to extract the elastic modulus and hardness of the sample. The Oliver-Pharr model is briefly reviewed here following the basic explanation in Ref. [16], where further details can be found.

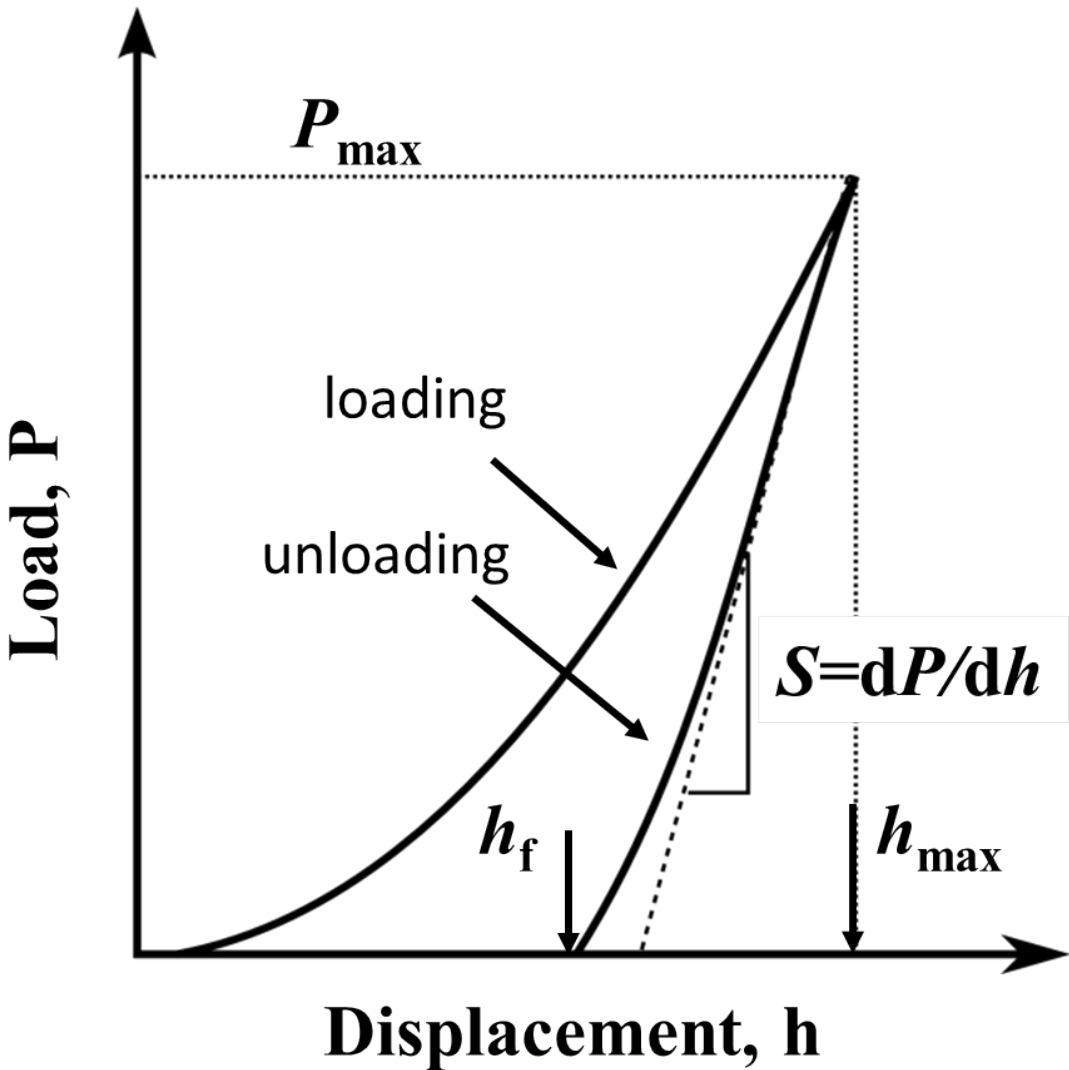


Figure 2.10: An example of a load *vs.* displacement curve in a typical nanoindentation measurement. Figure drawn after Ref. [16].

The unloading curve can be characterized by three physical quantities; the maximum load P_{\max} , the maximum displacement h_{\max} , and the elastic unloading stiffness, $S = dP/dh$, which represents the tangential line at the upper portion of the unloading curve (at the start of the unloading curve). It should also be noted that the final depth h_f has usually non-zero value due to the plastic deformation which may occur during the loading cycle. The unloading curve can be modeled by a power law relation, given as:

$$P = \alpha(h - h_f)^m \quad (2.16)$$

where α and m are power law fitting parameters.

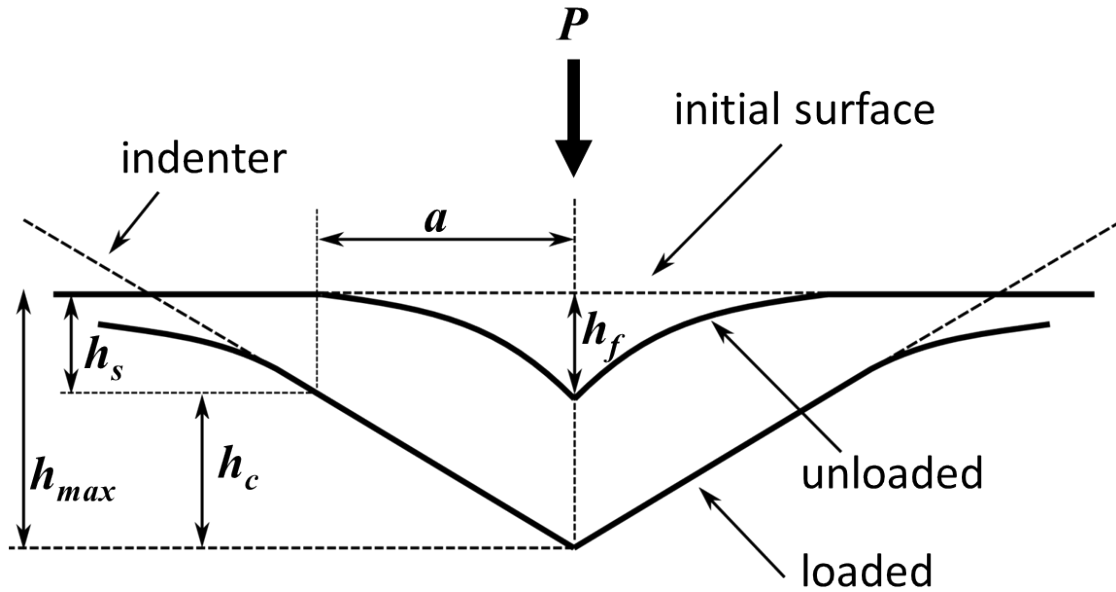


Figure 2.11: Schematic illustration of the unloading procedure in nanoindentation measurement. Figure drawn after Ref. [16].

The unloading procedure is illustrated schematically in Fig. 2.11. It is assumed here that the pile-up of material at the contact periphery during the initial loading procedure is negligible [16]. The amount of sink-in h_s is then approximated by:

$$h_s = \epsilon \frac{P_{\max}}{S} \quad (2.17)$$

where ϵ is a parameter which is a function of the geometry of the indenter.

The vertical displacement of the contact periphery h_c from the sink-in can be obtained by inspecting the geometry shown in Fig. 2.11, that is, $h_c = h_{\max} - h_s$. From Eq. (2.17):

$$h_c = h_{\max} - \epsilon \frac{P_{\max}}{S} \quad (2.18)$$

The projected area of the indenter at a distance d back from its tip can be calculated, and is called the ‘area function’. Assuming the area function $A_c(d)$ can be obtained by calibration measurement from a standard sample experimentally, the contact area A is given as:

$$A = A_c(h_c) \quad (2.19)$$

The hardness can be obtained from the contact area:

$$H = \frac{P_{\max}}{A} \quad (2.20)$$

The elastic modulus E is related to the contact area A and unloading stiffness S , given as:

$$S = \beta \frac{2}{\sqrt{\pi}} E_{\text{eff}} \sqrt{A} \quad (2.21)$$

where E_{eff} is the effective (or reduced) elastic modulus defined by

$$\frac{1}{E_{\text{eff}}} = \frac{1 - \nu^2}{E} + \frac{1 - \nu_i^2}{E_i} \quad (2.22)$$

where ν is the specimen’s Poisson ratio and ν_i and E_i are the corresponding parameters for the indenter.

The effective elastic modulus is a required modification to include the effect from the fact that the elastic displacement occurs both in the specimen (E, ν) and the indenter (E_i, ν_i). It was assumed in the original Oliver-Pharr model that β is 1 but it was found later that modification may be necessary for more accurate extraction.

In this dissertation, the nanoindentation method was not only used to measure intrinsic properties of the printed nanoparticle films but also to study the effective spring constant of movable structures, such as cantilever beam of printed relays, since the nanoindenter could be used to facilitate mechanical deflection of the cantilever.

Bibliography

- [1] John L. Vaught et al. *Thermal Ink Jet Printer, US Patent 4,490,728*. 1984.
- [2] Ichiro Endo et al. *BUBBLE JET RECORDING METHOD AND APPARATUS IN WHICH A HEATING ELEMENT GENERATES BUBBLES IN A LIQUID FLOW PATH TO PROJECT DROPLETS, US Patent 4,723,129*. 1988.
- [3] Steven I. Zoltan. *Pulsed Droplet Ejecting System, US Patent 3,683,212*. 1972.
- [4] Edmond L. Kyser and Stephan B. Sears. *Method and Apparatus for Recording with Writing Fluids and Drop Projection Means Therefor, US Patent 3,946,398*. 1970.
- [5] J Frits Dijkstra and Anke Pierik. “Dynamics of Piezoelectric Print-Heads”. In: *Inkjet Technology for Digital Fabrication*. John Wiley & Sons, Ltd, 2012, pp. 45–86.
- [6] N Reis and B Derby. “Ink Jet Deposition of Ceramic Suspensions: Modeling and Experiments of Droplet Formation”. In: *MRS Online Proceedings Library 625* (2000), null–null.
- [7] Thomas Young. “An Essay on the Cohesion of Fluids”. In: *Philosophical Transactions of the Royal Society of London* 95 (Jan. 1805), pp. 65–87.
- [8] Pierre de Gennes, Françoise Wyard, and David Quéré. *Capillary and wetting phenomena: bubbles, pearls, waves*. New York, NY 10013: Springer, 2004.
- [9] Robert D Deegan et al. “Capillary flow as the cause of ring stains from dried liquid drops”. In: *Nature* 389 (6653) (Oct. 1997), pp. 827–829.
- [10] Byung Mook Weon and Jung Ho Je. “Self-Pinning by Colloids Confined at a Contact Line”. In: *Physical Review Letters* 110 (2) (Jan. 2013), p. 28303.
- [11] Peter J Yunker et al. “Suppression of the coffee-ring effect by shape-dependent capillary interactions”. In: *Nature* 476 (7360) (Aug. 2011), pp. 308–311.
- [12] Rajneesh Bhardwaj et al. “Self-Assembly of Colloidal Particles from Evaporating Droplets: Role of DLVO Interactions and Proposition of a Phase Diagram”. In: *Langmuir* 26 (11) (Mar. 2010), pp. 7833–7842.
- [13] James Gere and Barry Goodno. *Mechanics of Materials*. 7th ed. CENGAGE Learning, Apr. 2008.
- [14] Clark T Nguyen. *EE 245 Lecture Notes -Introduction to MEMS Design Fall 2010*. 2010.

- [15] W C Oliver and G M Pharr. “An improved technique for determining hardness and elastic modulus using load and displacement sensing indentation experiments”. In: *Journal of Materials Research* 7 (06) (1992), pp. 1564–1583.
- [16] W.C. Oliver and G.M. Pharr. “Measurement of hardness and elastic modulus by instrumented indentation: Advances in understanding and refinements to methodology”. In: *Journal of Materials Research* 19 (01) (Mar. 2011), pp. 3–20.

Chapter 3

Inkjet-Printed Micro-Electro-Mechanical Switch

3.1 Introduction

Printed electronics employing solution-processed materials is considered to be the key to realizing low-cost large-area electronic systems, but the performance of printed transistors is not generally adequate for most intended applications due to limited performance of printable semiconductors. An alternative approach for a printed switch is proposed, where the use of semiconductors can be avoided by building mechanical switches with printed metal nanoparticles. In this chapter, inkjet-printed micro-electro-mechanical (MEM) switches are presented that can deliver abrupt switching characteristics, very low on-state resistance ($\sim 10 \Omega$), and nearly perfect off-state behavior with on/off current ratio of 10^7 , which can be used to implement complementary logic functions. The devices are fabricated using a novel process scheme to build 3-dimensional cantilever structures from solution-processed metallic nanoparticles and sacrificial polymers. These printed MEM switches thus represent a uniquely attractive path for realizing printed electronics.

3.2 Advantages of Printed Mechanical Switches

Printed electronics has received a great deal of attention in recent years as a means of realizing low-cost electronic systems such as displays, sensors, and RFID tags. Most efforts to date have focused on printed thin film transistors (TFTs) based on organic semiconductors. Although the performance of printed TFTs has been improving steadily due to improvements made to printable semiconductor materials, the performance of printed TFTs is generally not adequate for most intended applications, both in terms of the achievable carrier mobility and in terms of the realizable off-state leakage current. We propose that an alternative switch may be extremely interesting in this regard, particularly if the use of printed semiconductors can be avoided. Interestingly, while printed semiconductors trail

their conventional counterparts, the performance of printed metals is already very close to conventionally processed metallic thin films. Metallic nanoparticles have been used to deliver printed metallic features with conductivity $> 70\%$ of bulk metal conductivity. Therefore, an alternative path for realizing printed electronics is clear; the use of semiconductors can be avoided entirely if the requisite switch functionality is realized by implementing devices via solution-processed metals exclusively. Specifically, mechanical switches may be used rather than electrical switches, thus delivering the same functionality while offering substantially enhanced performance. These can be made without semiconducting materials because they operate by electro-static actuation of a movable (conducting) electrode structure, rather than by modulating the conductivity of fixed (semiconducting) channels. Indeed, there have been some initial demonstrations of mechanical constructs realized using printed materials [1, 2, 3, 4], suggesting that electromechanical switches may be a viable path for realization of printed electronics. Here, for the first time we demonstrate printed micro-electro-mechanical (MEM) switches fabricated using nanoparticles, and show switching performance far exceeding that of printed transistors, thus attesting to the strength of this technology as a candidate switch for printed electronics. Indeed, we show that this technology has the potential to address virtually all the shortcomings of printed transistors. The devices show excellent switching behavior with very low on-resistance and nearly perfect off-state behavior with immeasurable leakage, and can be used to implement complementary logic functions. All this is achieved while leveraging the best class of printed electronic materials available today - metals. In other words, printed mechanical switches could represent a uniquely attractive path for realizing printed electronics.

3.3 Structure and Operating Principle of Printed MEM Switches

The printed MEM switches are demonstrated to illustrate the benefits of this approach. The structure and operation of the printed MEM switch design is illustrated (Fig. 3.1). The fabricated switch is a cantilever-type three-terminal switch, where the movable cantilever beam is electro-statically actuated downward into contact with a drain electrode when a suitably large voltage difference exists between it and an underlying gate electrode. When the switch is in the OFF state, there is an air gap separating the beam and the contacting drain electrode so that ideally no current can flow ($I_{OFF} = 0$). This then allows for the realization of switches with abrupt switching behavior and ultra-low leakage; indeed, we find leakage to be at the noise floor of our measurement setup, attesting to the advantages of MEM switches in this regard. In these switches, the position of the source beam depends on the balance between the electrostatic force (F_{elec}) and the spring restoring force of the beam (F_{spring}). While F_{elec} increases super-linearly with increasing downward beam displacement, F_{spring} increases only linearly with displacement. Thus, there is a critical displacement beyond which F_{elec} is always larger than F_{spring} , so that the gap will eventually close abruptly as the

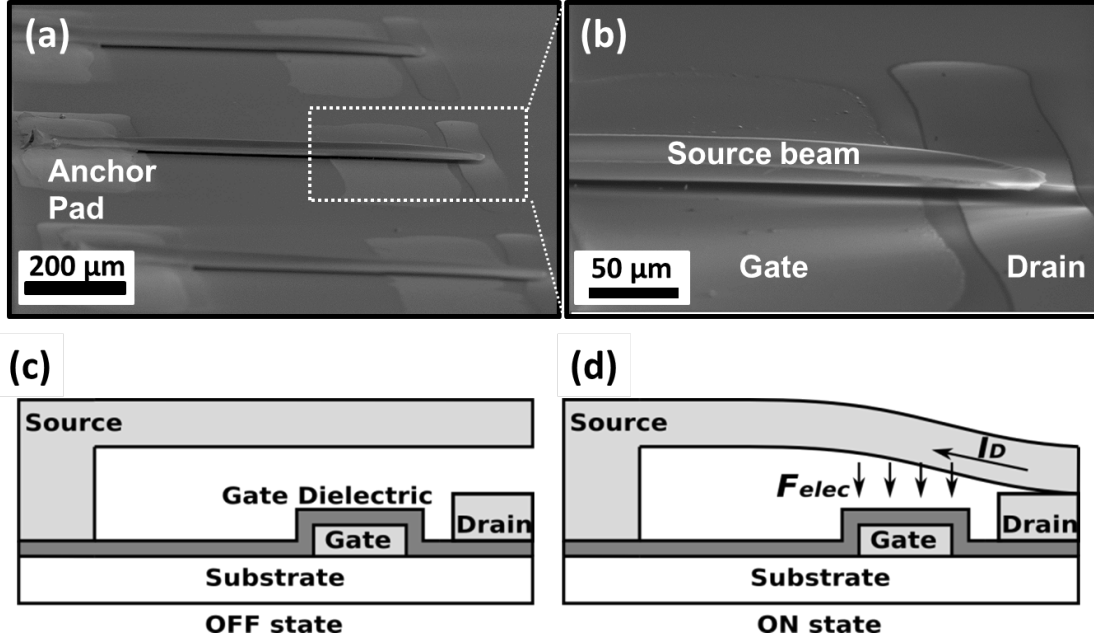


Figure 3.1: Structure and operation of the printed MEM switch design is illustrated. Scanning electron micrographs of (a) the whole view of the printed MEM switch with (b) magnified view of the end of the beam. Source beam is anchored to source pad and two additional bottom electrodes (actuating gate and contacting drain) are located under the beam. Illustration of the three-terminal switch structure (c) in the *OFF*-state and (d) in the *ON*-state.

applied voltage across the gap is increased. This phenomenon is referred to as “pull-in,” and the voltage (V_{PI}) at which it occurs is dependent on the switch design parameters [5](See Chapter 2):

$$V_{PI} = \sqrt{\frac{8}{27} \frac{k_{\text{eff}} g_0^3}{\epsilon_0 A_a}} \quad (3.1)$$

where k_{eff} is the effective spring constant of the beam, g_0 is as-fabricated actuation gap thickness, the ϵ_0 is the vacuum permittivity, and A_a is the actuation area (i.e. beam-to-gate overlap). To prevent the possibility of source-to-gate leakage, an insulating gate-dielectric layer covers the gate electrode.

3.4 Fabrication Process

In this section, fabrication processes innovations which were required for solution-based MEM relay fabrication are discussed. First, MEM switches require very good control of gap thickness; this is achieved by developing a sacrificial layer process wherein a highly

Parameter	Value [μm]
Beam Width [W]	90
Beam Thickness [H]	2.25
Beam Length [L_b]	650
Anchor-to-gate Length [L_g]	450
Actuation Gap [g_0]	1.65
Contact Gap [g_d]	1.2
Gate Width [W_d]	180

Table 3.1: Design parameters and values of the fabricated printed MEM switches.

uniform spin-coated organic release layer is used to set the gap precisely over an entire substrate prior to printing the cantilever. Second, MEM switches require strong mechanical anchor formation for the cantilever beam which overlies the source contact. Given the aforementioned sacrificial layer, a printed via process [6] is used, wherein the sacrificial layer is dissolved and dried to the edges of the anchor region by printing solvent to define the anchor hole. Finally, MEM switches require a robust cantilever formation and release process; this is achieved by using sintered printed metallic nanoparticles to form the cantilever and by etching away the organic sacrificial layer in solvent to release the overlying cantilever. Note that all steps in the process must achieve solvent orthogonality, such that the solvent from upper layers does not attack previously deposited lower layers. This was obtained by selecting solvent materials that do not interact substantially upon deposition.

The process used to fabricate the MEM switches is illustrated in Fig. 3.2, with dimensions as shown in Table 3.1. Silver nanoparticle ink (CCI-300 from Cabot Corp., Boston, MA) is used to print the gate, drain, and source electrodes as follows. First, the gate electrode was inkjet-printed onto the insulating substrate. An oxidized Si wafer was used for convenience in this case, though the process temperatures make the process fully compatible with a wide range of substrates. Next, poly-4-vinylphenol (PVP) was spin-coated and cross-linked to form an insulating gate dielectric layer (Fig. 3.2(a)). The cross-linking ensures solvent orthogonality for subsequent printing steps in that the cross-linked PVP layer will act as an etch-stop layer when the sacrificial layer is etched during the via-hole process because the etchant solvent (acetone) will dissolve the sacrificial layer while cross-linked PVP is insoluble. The PVP layer also provides an optimal wetting condition for the silver ink, so that the drain electrode and source pad can be printed to form the desired patterns. The gate dielectric electrically isolates the gate from the source beam if it comes into contact with both the drain and gate electrodes.

Next, the drain electrode and source pad were printed (Fig 3.2(b)), where the drain can be intentionally thickened in the contacting region (as shown in Fig. 3.3) by printing a single drop of silver ink multiple times onto the same spot. This “dimpled” design allows the apparent contact area (A_c) to be well defined and provides for a smaller contact gap (g_d) which is beneficial for reducing the switch turn-on delay. $F_{adhesion}$ can be reduced

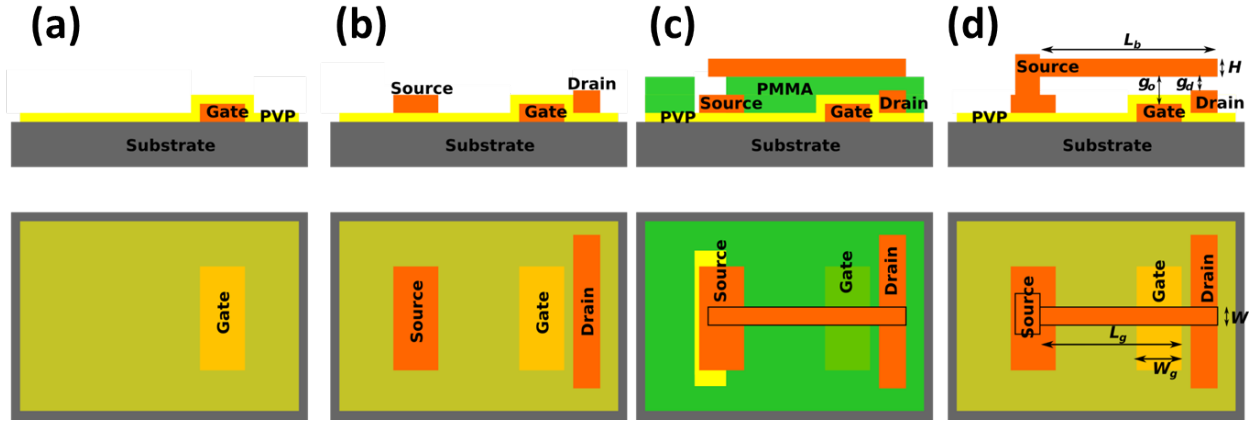


Figure 3.2: Illustration of the process used to fabricate the MEM switches. (a) Gate electrode is printed with silver ink; thin film of cross-linked PVP is spin-coated to form the gate dielectric. (b) Drain electrode and source pad are printed in alignment with the gate electrode. Additional drops of ink can be printed in the contacting region to define a contact dimple. (c) Sacrificial layer of PMMA is spin-coated and source beam is inkjet-printed, after which the source anchor region is defined by printing acetone to dissolve PMMA underneath one end of the source beam. (d) The source anchor is formed by filling the hole in the PMMA with inkjet-printed silver ink, and the structure is released by removing PMMA film with acetone.

by leveraging the “coffee-ring” effect to reduce A_c . Figure 3.3 shows the topography of a contact dimple measured by an optical profilometer. It has a crater-like structure, so that the apparent contact area A_c is significantly smaller than the dimple area. Characteristic parameters of the contact dimple structure are defined in Fig. 3.4. The apparent contact area is estimated to be $A_c = \pi d_d w_d$, where the “coffee-ring” width d_d is defined at a critical path t_c . It is possible to adjust A_c (hence $F_{adhesion}$ and R_{ON}) by varying the number of printed drops. Fig. 3.5 shows how A_c and also the thickness of the dimple depend on the number of printed drops. A_c increases with the first 3 drops because they fill the center of the dimple. (This is corroborated by the measurements of t_d which show that the dimple thickness is almost constant for the first 3 drops.) A_c then decreases as additional drops are printed.

After electrode formation, a sacrificial poly(methyl-methacrylate) (PMMA) layer was spin-coated (thickness $\sim 1.8\mu\text{m}$) and cross-linked at 180°C . PMMA was chosen since the cross-linked form is sufficiently robust to survive subsequent cantilever printing, but is still soluble in solvents as needed for anchor formation and cantilever release.

The cantilever beam then was printed onto the sacrificial PMMA layer; since it is printed immediately on top of the spin-coated sacrificial layer, a well-controlled gap is ensured. The surface of the PMMA is known to be very hydrophobic (surface energy of PMMA = 32.7 mN/m [7]), which prevents deposited droplets from being spreaded properly to form

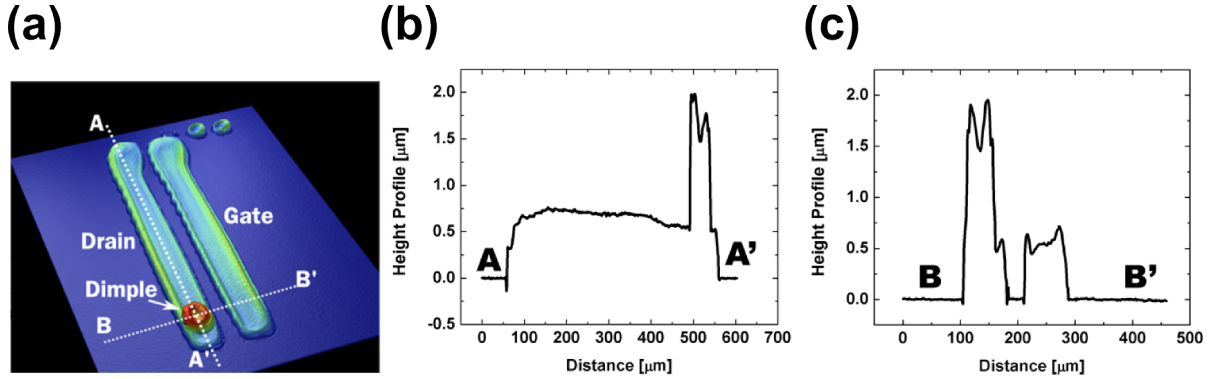


Figure 3.3: Measured height profile of the printed electrodes with dimpled drain structure. (a) 3-dimensional height profile taken by optical profilometer. The 2-D line scan profile along A-A' and B-B' lines are shown in (b) and (c), respectively.

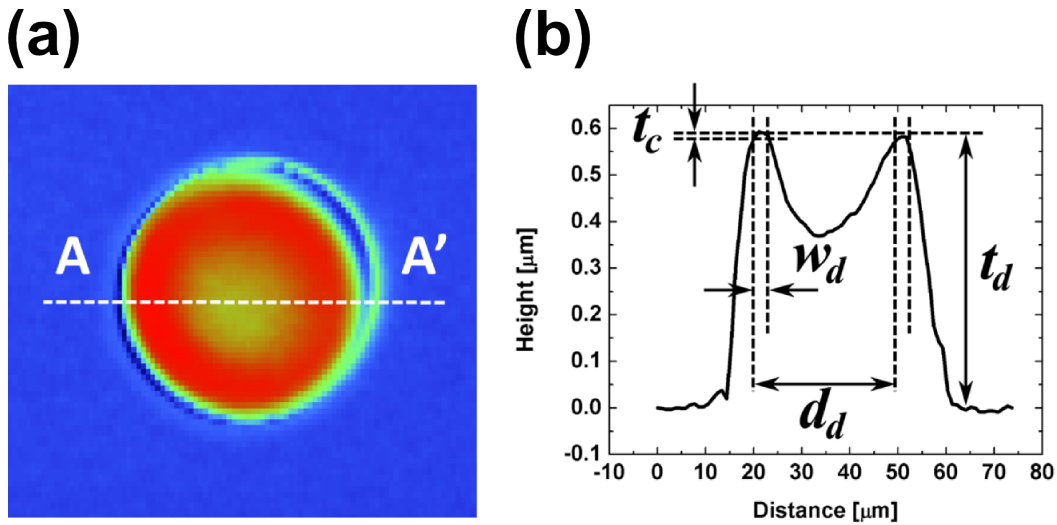


Figure 3.4: Profile of contact dimple structure. Characteristic patterns of the dimple are defined in (b) the plot of thickness along the line A-A' in (a). The apparent contact area is calculated as $A_c = \pi d_d w_d$, where the “coffee-ring” width d_d is defined at a critical depth t_c (15 nm)

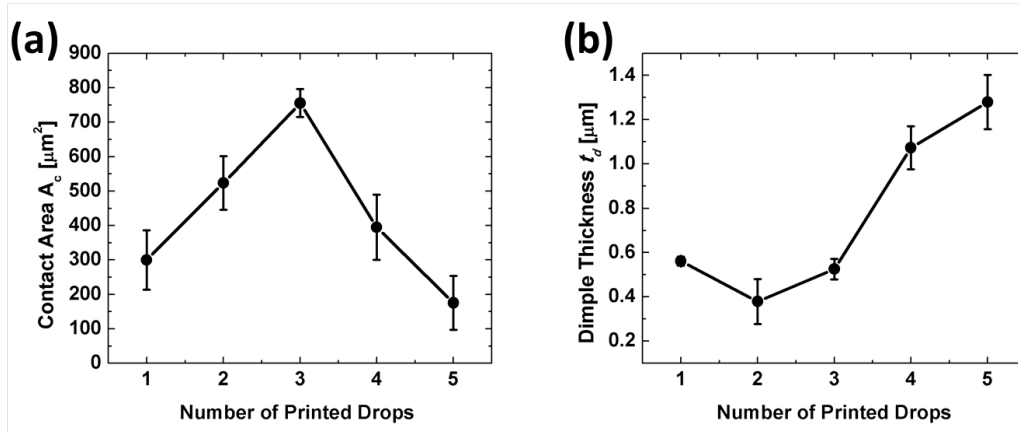


Figure 3.5: Dependence of contact dimple parameters on the number of printed drops. (a) Measured apparent contact area A_c varies non-monotonically with the number of printed drops because the first 3 drops fill the center of the dimple. After the center of the dimple is completely filled up, A_c decreases as more drops are printed. This is substantiated by (b) the measurement of t_d which shows that the dimple thickness remains almost constant for the first 3 drops.

continuous pattern. The surface of PMMA needs to be modified to obtain desired wettability, which can be done by exposing it to UV-ozone to add polar functional groups so that the surface energy be increased [8]. Figure 3.6 shows the change of contact angle of water on PMMA as a function of the amount of time in which PMMA is exposed to UV-ozone. For optimal wetting, UV-ozone exposure of 210 sec was chosen for beam printing. It is important to optimize the beam thickness because this determines the effective beam stiffness k_{eff} for given beam dimensions; thinner beams will collapse upon release due to stiction [9] while thicker beams will have high V_{PI} and hence have large power consumption. The thickness of the beam in this work was controlled by adjusting the number of printed layers, as shown in Fig. 3.7 (~ 450 nm per layer with drop space = $25 \mu\text{m}$), with interspersed drying steps between the layers. The beam was dried at 150°C , and annealed afterwards at 180°C . This multi-step process ensures that thick films can be built up without any emergence of bulging and cracking from excessive solvent volumes [10]. It should be noted that ‘wrinkles’ have been observed on the printed film in the multi-layer process (Fig. 5.7), when the thermal budget used in the interspersed drying steps is not large enough (drying temperature $< 120^\circ\text{C}$). This might result from residual polymers, which is used in nanoparticle ink to encapsulate particles to prevent them from aggregation in solution, in the lastly deposited dried film may be driven out at the drying step of the next deposited film. The formation of ‘wrinkles’ was successfully prevented by using larger thermal budget (150°C for 5 mins) in the drying process. It was found that the beam thickness (H) must be $> 1.6 \mu\text{m}$ to avoid collapse or stiction upon release.

The anchor for the beam was then formed as follows: first, the anchor region was defined

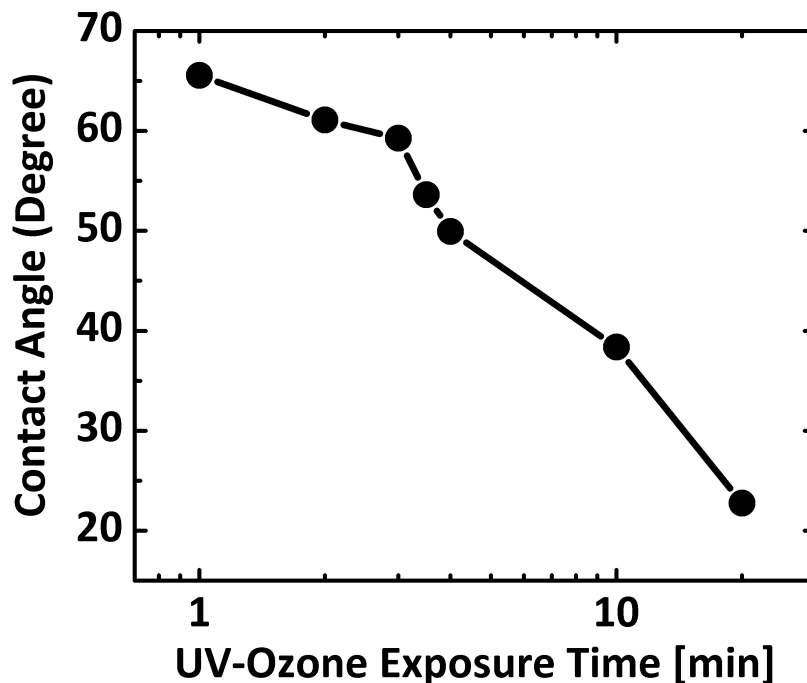


Figure 3.6: Dependence of contact angle of water on the PMMA surface on the amount of time in which it is exposed to UV-ozone. The contact angle decreases as longer exposure to UV-ozone add more polar functional groups on the surface of PMMA [8].

by inkjet-printing acetone to etch a hole in the PMMA [6] underneath one end of the beam (Fig 3.2(c)); then, this hole is filled by printing silver nanoparticle ink, connecting the beam to the underlying source pad (Fig. 3.2(d)).

The use of inkjet-printed solvent to form the via hole has some unique consequences. This is not a true “etching” process, in that the resulting waste material is not removed, but is rather deposited at the edge of the hole. Thus, the via formation process results in a crater-like structure (Fig. 3.9(a,b)), where the boundary is thicker than the center of the pattern, due to the so-called ‘coffee-ring’ effect [6]. Figure 3.9(c) shows an optical micrograph of the printed cantilever from the top view. Since the “crater” is formed after the cantilever is printed and annealed, the crater does not alter the cantilever gap; this is a key benefit of the two-step cantilever beam formation process used here, where the cantilever is printed first and the via hole is formed subsequently. Finally, the via hole is filled with nanoparticle metal ink and sintered to form the anchor, which serves as the source contact for the MEM switch. The peak temperature for the entire process is 220°C, which makes this device attractive for use on a wide range of substrates. Indeed, since the PVP is merely a dielectric material, other materials with lower cross-linking temperatures could potentially be used to

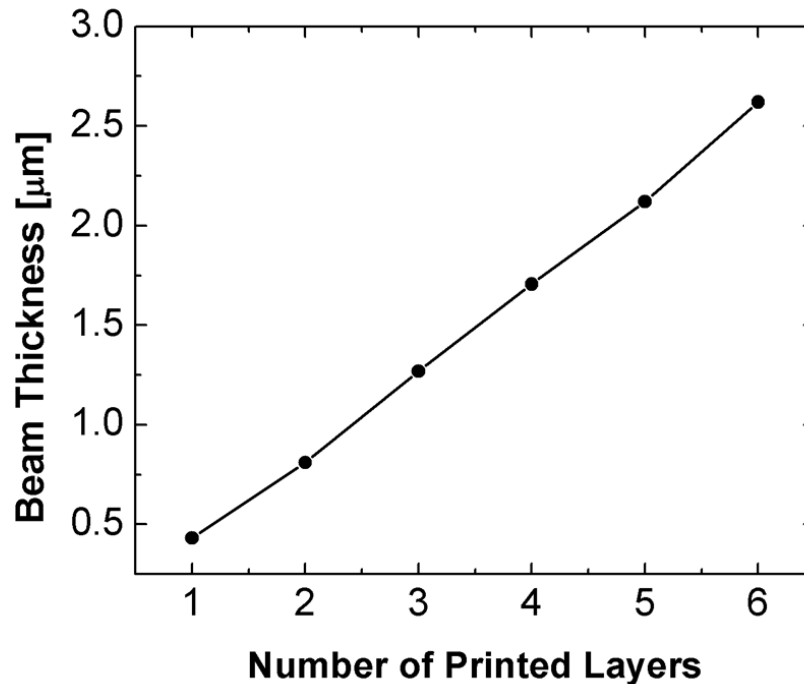


Figure 3.7: Measured source-beam thickness vs. number of printed layers. The thickness of the beam in this work was controlled by adjusting the number of printed layers. Increment of thickness from each additionally printed layer is approximately 450 nm, when using drops with spacing of 25 μm .

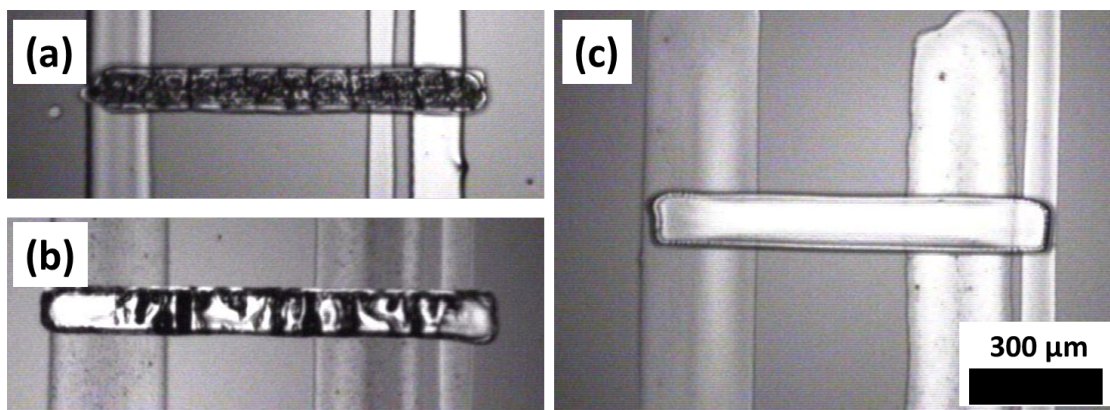


Figure 3.8: “Wrinkles” on the printed layer upon drying process. (a,b) When the temperature used in the interspersed drying steps between the layers is lower than 120°C, wrinkles can be observed on the dried printed film. (c) The formation of wrinkles can be avoided by using higher drying temperature ($> 120^\circ\text{C}$).

reduce the temperature requirements even further.

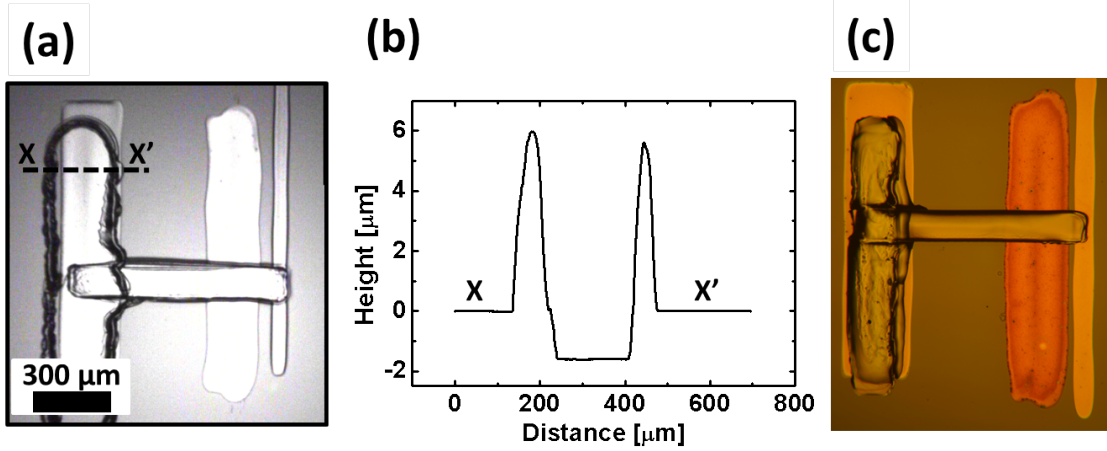


Figure 3.9: Illustration of the two-step anchoring process. (a) Optical micrograph of cantilever beam after the hole is defined by inkjet-printing PMMA. (b) Surface profile of the etch hole along the XX' line at (a) shows the crater-like structure, where the boundary is thicker than the center of the pattern. (c) Optical micrograph of the released MEM switch.

3.5 Electrical Characteristics of Printed MEM Switches

The measured switch driving current (I_D) *vs.* gate voltage (V_{GS}) characteristic is shown in Fig 3.10(a), using the schematic diagram of the measurement setup shown in Fig 3.11 ($V_{DD} = 1, 10, 100$ mV, $R_L = 6.74$ k Ω). It shows immeasurably low I_{OFF} (below the noise floor of the semiconductor parameter analyzer) and abrupt switching behavior; this attests to the excellent switching characteristics of MEM switches, making them attractive for the aforementioned candidate applications of printed electronics. Note that the switch turns on when V_{GS} increases above V_{PI} , but turns off when V_{GS} is lowered below the release voltage V_{RL} . Hysteresis ($V_{RL} < V_{PI}$) exists because F_{elec} remains larger than F_{spring} for values of $V_{GS} < V_{PI}$ when the source is pulled in, and it is exacerbated by surface adhesive force ($F_{adhesion}$) in the contacting region. Note that hysteresis is not a problem in the intended printed electronics applications, provided it is controlled and falls within a reasonable range, as is achieved herein.

Figure 3.10(b) shows the measured switch current (I_D) while the voltage on the drain electrode (V_{DS}) is varied for a fixed V_{GS} . For $V_{GS} > V_{PI}$, I_D linearly increases with V_{DS} ; thus, in the *ON* state the switch can be modeled as a simple resistor, R_{ON} (*ON*-state resistance). The inverse slope of the $I_D - V_{DS}$ plot gives a value of $R_{ON} \sim 10\Omega$. Considering that there is a metal-metal junction at the contact between the source beam and the drain electrode,

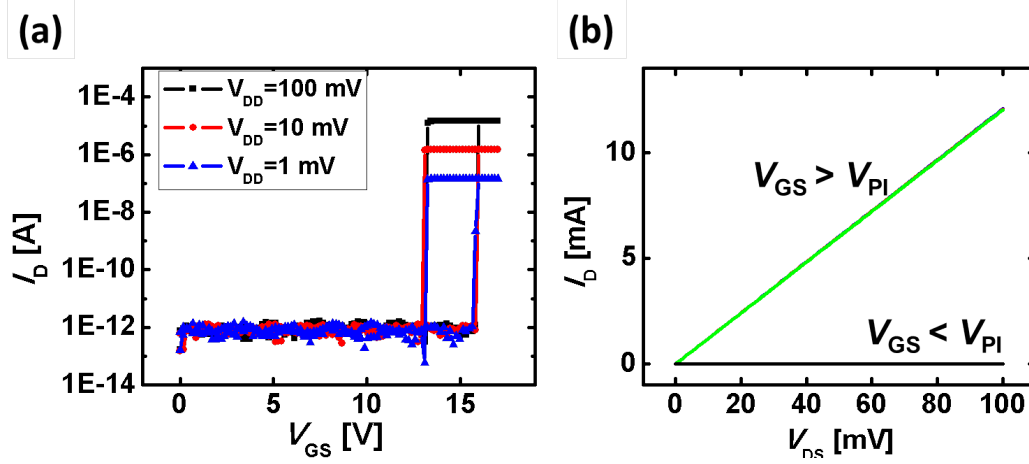


Figure 3.10: Steady-state electrical characteristics of the printed MEM switch. Measured (a) I_D - V_{GS} and (b) I_D - V_{DS} characteristic of the printed MEM switch. The I_D - V_{GS} measurement was carried out using the schematic diagram of the measurement setup shown in Fig 3.11 with $R_L = 6.74k\Omega$.

R_{ON} can be further modeled as two resistors connected in series; $R_{ON} = R_{contact} + R_{bulk}$, where $R_{contact}$ is the contact resistance at the drain contact and R_{bulk} is that from the rest of the switch. The sheet resistance of the printed nanoparticle film used in this work is about $0.2 \Omega/\square$, and the switch comprises 14 squares, which results in $R_{bulk} \sim 3\Omega$. Thus R_{ON} is dominated by $R_{contact} \sim 7\Omega$.

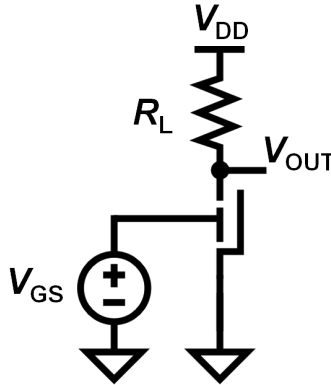


Figure 3.11: Circuit schematic of the measurement setup used for electrical characterization of the printed MEM switch.

To investigate the dynamic behavior of the cantilever-type switch, transient characteristics were measured. Figure 3.12(a) shows *a.c.* characteristics, where an input voltage pulse signal (frequency of 1 kHz and amplitude of 21 V) is applied to the gate and the output volt-

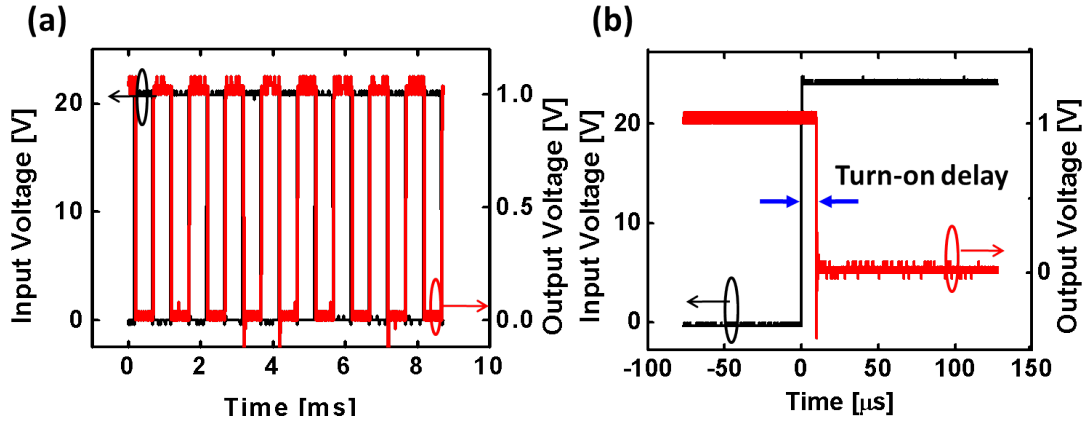


Figure 3.12: Dynamic electrical characteristics of the printed MEM switch. (a) Measured input and output voltage waveforms for the printed MEM switch inverter circuit with $R_L = 6.7k\Omega$ and $V_{DD} = 0.1V$, (b) Measurement of pull-in delay for the printed MEM switch. Note that the measurement was performed using a similar setup to that shown in Fig 3.11.

age is measured at the drain electrode, using a similar setup to that shown in Fig 3.11. In the *OFF*-state, the switch remains open and the potential at the drain electrode follows V_{DD} ; on the other hand, when the switch closes in the *ON*-state, the drain potential approaches that of the grounded source electrode since $R_{ON} \ll R_L$. There is a delay between the input and output voltage signals, which consists of mechanical and electrical delays. Mechanical delay arises from the fact that it takes time for the beam to traverse the original contact gap in response to the electrostatic force induced by the gate voltage. Furthermore, electrical signals have intrinsic RC delays when they propagate through a conducting medium. Therefore, the total delay is the sum of the mechanical and electrical delay. Figure 3.12(b) shows this turn-on delay, which is mainly mechanical delay since resistance and capacitance from the switch itself are small.

As expected, this delay can be reduced by increasing the applied electrostatic actuation force on the beam, F_{elec} , where larger F_{elec} will cause the beam travel faster. Specifically, turn-on delay is inversely proportional to the applied gate voltage [11], in the range of $10 - 16\mu s$, depending on the gate-overdrive voltage, as shown in Fig 3.13. The delay can be further reduced by scaling device dimensions, especially by reducing the contact gap (g_d), and hence shortening the travel distance of the beam. Importantly, since the mechanical delay is dominant with negligible electrical RC delay, a substantial design opportunity exists to work around the mechanical delay and realize ultra-fast electrical operation (the contribution of RC delay is estimated to be, $RC \sim R_{ON}(\epsilon_0 A_a / g_0) \sim (10\Omega \times 87fF) \sim 0.87ps$). Previous design analyses have shown that MEM switch-based circuits can be optimized by utilizing complex gates such that all the switches move simultaneously and only one mechanical delay is incurred per operation [11]. Endurance of the MEM switches was studied using a similar test setup, by monitoring R_{ON} throughout the test. The switch can endure $\sim 10^5$ on/off hot

switching cycles (Fig 3.14) without stiction- or welding-induced failure.

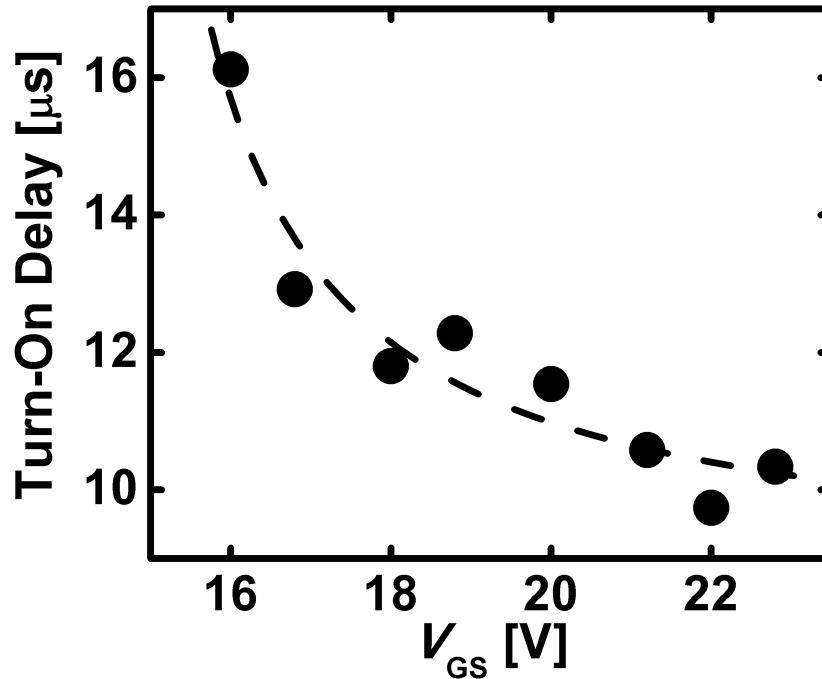


Figure 3.13: Dependence of pull-in delay on applied gate-to-source voltage V_{GS} . The pull-in delay improves with increasing electrostatic actuation force F_{elec} from larger V_{GS} , which causes the beam travel faster.

3.6 Mechanical Properties

To study the mechanical properties of the solution-processed nanoparticle material and structural properties of the resulting cantilever beam, nanoindentation [12] was employed. In a nanoindentation measurement, a sharp mechanically strong tip (often diamond) of a specific geometry is used to apply a controlled load onto the surface of a film such that a nano-scale indent is formed while the applied load on the tip and the corresponding displacement of the tip are recorded. By studying the measured load-displacement curve, which shows the indentation response of the film, intrinsic mechanical properties such as contact stiffness, hardness, and elastic modulus can be extracted. For movable structures, nanoindentation offers the additional advantage of enabling the extraction of the effective beam stiffness. We applied a nanoindenter load to the end of the cantilever beam and obtained a load-displacement curve as shown in Fig. 3.15(a). Two regimes are apparent, where (I) the beam is free-standing and bends downward to the contact electrode, and (II) the beam is finally in

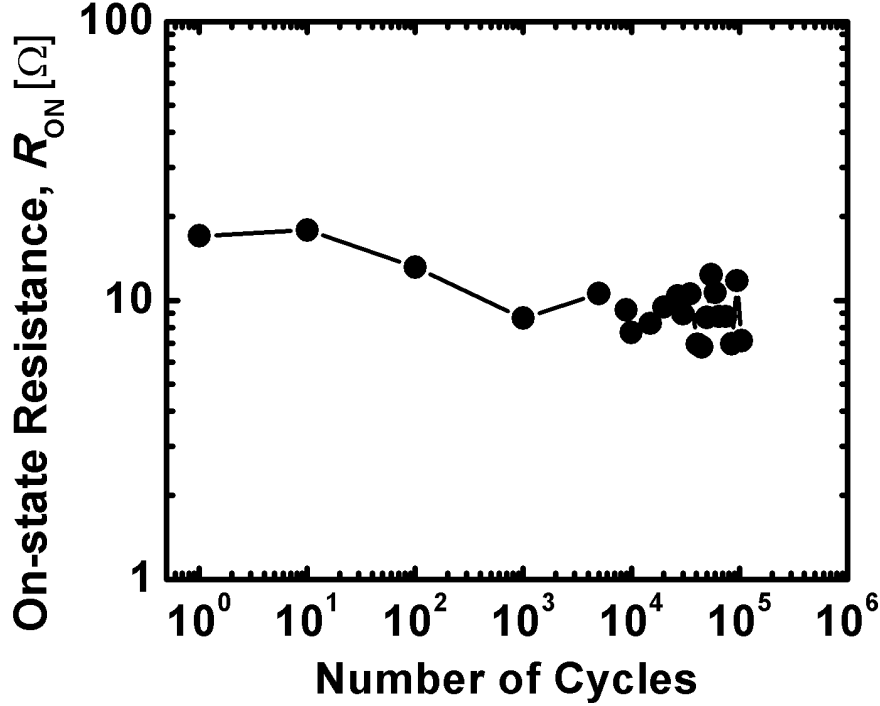


Figure 3.14: Endurance measurement of the switches shows they can operate on/off hot switching up to $> 10^5$ cycles.

contact with the contact electrode and the nanoindenter tip starts to make an indentation into the surface of the beam (Fig. 3.15(b)). In regime (I), all the displacement comes purely from the beam displacement, which increases with the applied load. The load-displacement curve shows a linear response and the effective spring constant of the beam, k_{eff} , can be extracted from the slope of the curve in this regime. The linear fit results in a slope of 9.7 N/m (Fig. 3.15(a), segment **a**). It is worth comparing this measured value of k_{eff} to that calculated from the electrical measurement of V_{PI} , as expressed in Equation 3.1. The pull-in voltage was measured as $V_{\text{PI}} \sim 16.0\text{V}$ (Fig. 3.10(a)). From the design of the switch, the actuation gap thickness g_0 was defined to be $\sim 1.65\mu\text{m}$, $A_a \sim 180 \times 90\mu\text{m}^2$ (gate width $\sim 180\mu\text{m}$, beam width $\sim 90\mu\text{m}$), which results in $k_{\text{eff}} \sim 27.6\text{N/m}$. The two different effective spring constants k_{eff} , one from mechanical ($k_{\text{eff,m}}$) and the other from electrical ($k_{\text{eff,e}}$) measurements, correspond to the response of the beam to two different load application locations. In the electrical measurement, F_{elec} was applied from the gate electrode, while the nanoindenter tip exerted a concentrated load on the end of the beam. Since the effective spring constant of the beam depends on the distance from the anchor to the loading point (L^3) [5], the ratio of spring constants $k_{\text{eff,e}}/k_{\text{eff,m}} \sim 2.8$ can be estimated from the ratio of beam length (L_b) over the distance from the anchor to the center of the gate electrode (L_g),

$(L_b/L_g)^3 \sim (650\mu\text{m}/450\mu\text{m})^3 \sim 3.0$. This is within 10% of the measured value, attesting to the accuracy of the modeling and material property estimates.

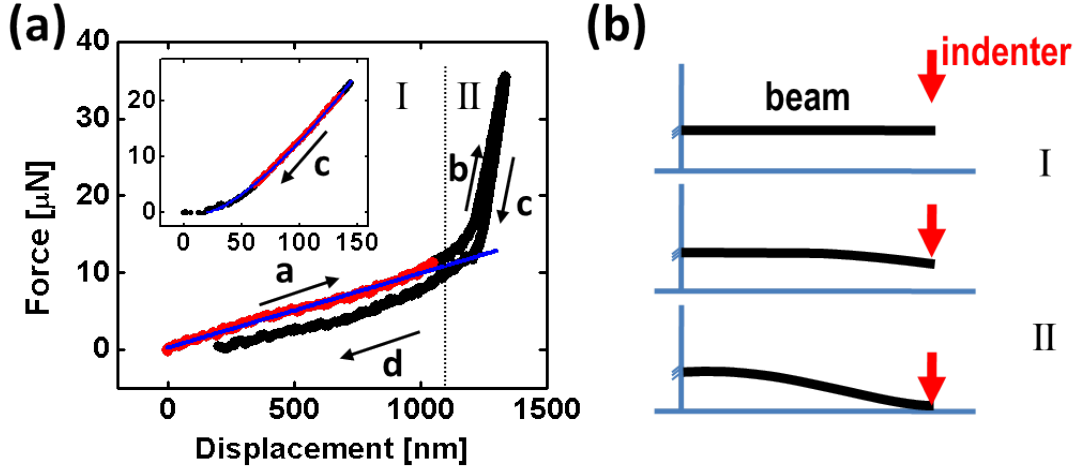


Figure 3.15: Structural analysis of the printed cantilever by nanoindentation technique. (a) Force-displacement curve was obtained by applying a nanoindenter load to the end of the cantilever beam; (inset) unloading portion of the curve is shown with effective force and distance values to extract the intrinsic properties of the printed nanoparticle film using Oliver-Pharr model [12]. (b) Schematic diagram shows the two different regimes; where (I) the beam is free-standing and bends downward to the contact electrode, and (II) the beam is finally in contact with the contact electrode and the nanoindenter tip starts to make an indentation into the surface of the beam.

In the second regime (II), intrinsic properties of the printed nanoparticle film were extracted using the conventional Oliver-Pharr model [12] to fit the unloading portion of the curve, as shown in the inset of Fig. 3.15(a), where the relevant unloading curve was extracted from Fig. 3.15(a). The middle portion of the unloading curve was fit to the load equation: $P = A(h - h_f)^m$, where h_f is final depth, h is the tip displacement, A and m are fitting parameters. The contact stiffness S , and reduced elastic modulus E_r of the material can be obtained by $S = \frac{dP}{dh} \big|_{h=h_{max}}$ and $E_r = \frac{\sqrt{\pi}}{2\sqrt{A_c(h)}}$, respectively, where $A_c(h)$ is a contact area function which depends on the geometry of the indenter tip used. From the curve, S is calculated as 260 N/m^2 and E_r is obtained as 47.5 GPa , which is somewhat lower than the value for bulk silver. This can be explained by the fact that the printed nanoparticle film is still somewhat porous after annealing, which may lead to a reduction in the elastic modulus [6]. The values from nanoindentation measurements on the cantilever beam and blank films (See Chapter 2) are consistent with each other. Indeed, this sintering-dependent mechanical property offers a design advantage for printed MEMS; the sintering of solution-processed nanoparticles can be used to tune the elastic modulus (E_r), which determines the effective spring constant of the beam. Since what separates region (I) and (II) physically is

the tip displacement value where the beam starts to be in contact with the bottom electrode, contact gap size can also be obtained from the displacement value at the boundary of the two regions, $\sim 1.2\mu\text{m}$. This is somewhat smaller than the thickness of the sacrificial PMMA, even after taking account of the difference between g_d and g_0 , because the silver nanoparticle ink is not perfectly orthogonal to PMMA and dissolves a small amount of PMMA during the cantilever printing process.

3.7 Conclusion

In summary, we have developed a new switch technology for printed electronics based on inkjet-printed MEM cantilevers. The MEM switches offer excellent on-state and off-state characteristics, and appear to be very promising for printed electronics applications. Several novel process steps were realized to ensure precise control of the actuation gap in printed MEMS structures, and the resulting devices showed low on-resistance, immeasurable leakage, good switching speed, and low voltage operation better than that of other many printed electronic devices.

Bibliography

- [1] S. B. Fuller, E. J. Wilhelm, and J. M. Jacobson. “Ink-jet printed nanoparticle microelectromechanical systems”. In: *Journal of Microelectromechanical Systems* 11 (1) (2002), pp. 54–60.
- [2] Corinne E. Packard et al. “Contact-Printed Microelectromechanical Systems”. In: *Advanced Materials* 22 (16) (Apr. 2010), pp. 1840–1844.
- [3] Yusaku Kato et al. “A large-area, flexible, ultrasonic imaging system with a printed organic transistor active matrix”. In: *2008 IEEE International Electron Devices Meeting* (Dec. 2008), pp. 1–4.
- [4] Shintaro Nakano et al. “Low operation voltage of inkjet-printed plastic sheet-type micromechanical switches”. In: *Applied Physics Letters* 92 (5) (Feb. 2008), pp. 053302–3.
- [5] Gabriel M Rebeiz. *RF MEMS Theory, Design, and Technology*. John Wiley & Sons, Inc., 2003.
- [6] T. Kawase et al. “Inkjet Printed Via-Hole Interconnections and Resistors for All-Polymer Transistor Circuits”. In: *Advanced Materials* 13 (21) (Nov. 2001), p. 1601.
- [7] K. E. van Ness. “Surface tension and surface entropy for polymer liquids”. In: *Polymer Engineering and Science* 32 (2) (Jan. 1992), pp. 122–129.
- [8] Edward M Liston. “Plasma Treatment for Improved Bonding : A Review”. In: *The Journal of Adhesion* 30 (1989), pp. 199–218.
- [9] J. M. Bustillo, R. T. Howe, and R. S. Muller. “Surface micromachining for microelectromechanical systems”. In: *Proceedings of the IEEE* 86 (8) (1998).
- [10] Julia R. Greer and Robert A. Street. “Mechanical characterization of solution-derived nanoparticle silver ink thin films”. In: *Journal of Applied Physics* 101 (10) (May 2007), pp. 103529–5.
- [11] Hei Kam et al. “Design, Optimization, and Scaling of MEM Relays for Ultra-Low-Power Digital Logic”. In: *Electron Devices, IEEE Transactions on* 58 (1) (2011), pp. 236–250.

- [12] W. C. Oliver and G. M. Pharr. “Measurement of hardness and elastic modulus by instrumented indentation: Advances in understanding and refinements to methodology”. In: *Journal of Materials Research* 19 (01) (Mar. 2011), pp. 3–20.

Chapter 4

Scaling of Inkjet-Printed Micro-Electro-Mechanical Switch

4.1 Introduction

The initial demonstration of printed micro-electro-mechanical (MEM) switches in Chapter 3 suggests that they can be potentially promising candidates for printed electronics. Based on the developed process, further optimization can be carried out to enhance device performance such as energy efficiency and to suppress process-induced performance variations. Reducing the operating voltage by scaling the device is of interest in this regard, which may lead to broader range of applications for printed switches. More in depth study on the process would be necessary for this purpose. In this chapter, various process-related issues will be studied to further optimize both the process and the performance of printed MEM switches.

4.2 Process Optimization for Scaled Actuation-gap Devices

The detailed fabrication process was previously described in Chapter 3, and the process steps which are relevant to scaling of the device and performance variation are revisited here. As mentioned previously, a two-step beam formation process was critical to overcome the difference in the printed ‘etch’ process from the conventional process using lithography and to form the required anchor. The ‘crater’-like structure from the coffee-ring effect forbids the use of one-step beam anchoring so that the beam has to be formed before it is anchored through the via-hole defined afterwards. The via-hole was defined by selectively dissolving the sacrificial poly(methyl methacrylate) (PMMA) layer at one end of the beam by printing a solvent (e.g. acetone) that can remove PMMA layer. This two-step process is illustrated in Fig. 4.1, where micrographs were taken at every step of the anchor formation process. The beam is first patterned on the sacrificial PMMA layer and via-hole was then defined

by printing multiple drops of acetone on a single spot (Fig. 4.1(a)). Next, this via-hole is filled with silver (Ag) nanoparticle ink by printing a sufficient volume of ink on the same spot (Fig. 4.1(b)). The beam can be connected to bottom source pad and becomes anchored after the filled Ag nanoparticle ink is sintered (150°C for 30 min.) (Fig. 4.1(c)).

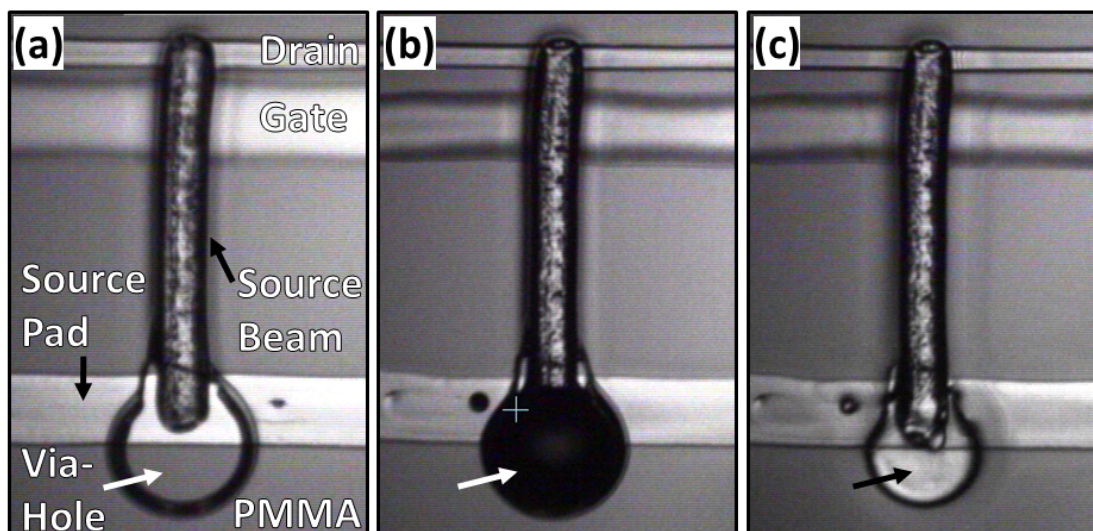


Figure 4.1: Micrographs showing two-step beam formation process. (a) The beam is patterned on the sacrificial PMMA layer and via-hole was then defined by printing multiple drops of acetone on a single spot. (b) Next, this via-hole is filled with silver (Ag) nanoparticle ink by printing a sufficient volume of ink on the same spot. (c) The beam can be connected to bottom source pad and anchored after the filled Ag nanoparticle ink is sintered.

One important parameter to be controlled in this process is the UV-ozone (UVO) exposure time; the PMMA is required to be exposed to UVO in order to introduce polymer chain-scission [1, 2], which makes it more vulnerable to dissolution by printed acetone so that it can be completely removed to define the anchor region. Without UVO exposure, a larger volume of acetone is required to dissolve the PMMA layer. The number of drops which is necessary to completely remove PMMA layer ($\sim 0.85 \mu\text{m}$ -thick) as a function of UVO exposure time is shown in Fig. 4.2(a) (solid square marker). The total time it takes to complete the via-hole process can be reduced by optimizing the UVO exposure time, since the number of drops that can completely remove PMMA decreases drastically by increasing UVO exposure time. After being exposed to UVO for 10 min., the PMMA layer can be dissolved out completely by printing less than 10 drops of acetone (inkjet nozzle head : $60 \mu\text{m}$ in diameter, MicroFab).

The UVO exposure time, however, cannot be arbitrarily increased because it can cause an ‘undercut’ effect during the via-hole process. The undercut in this via-hole formation is illustrated in Fig. 4.2(c), where an extension of the circular via-hole was formed under the

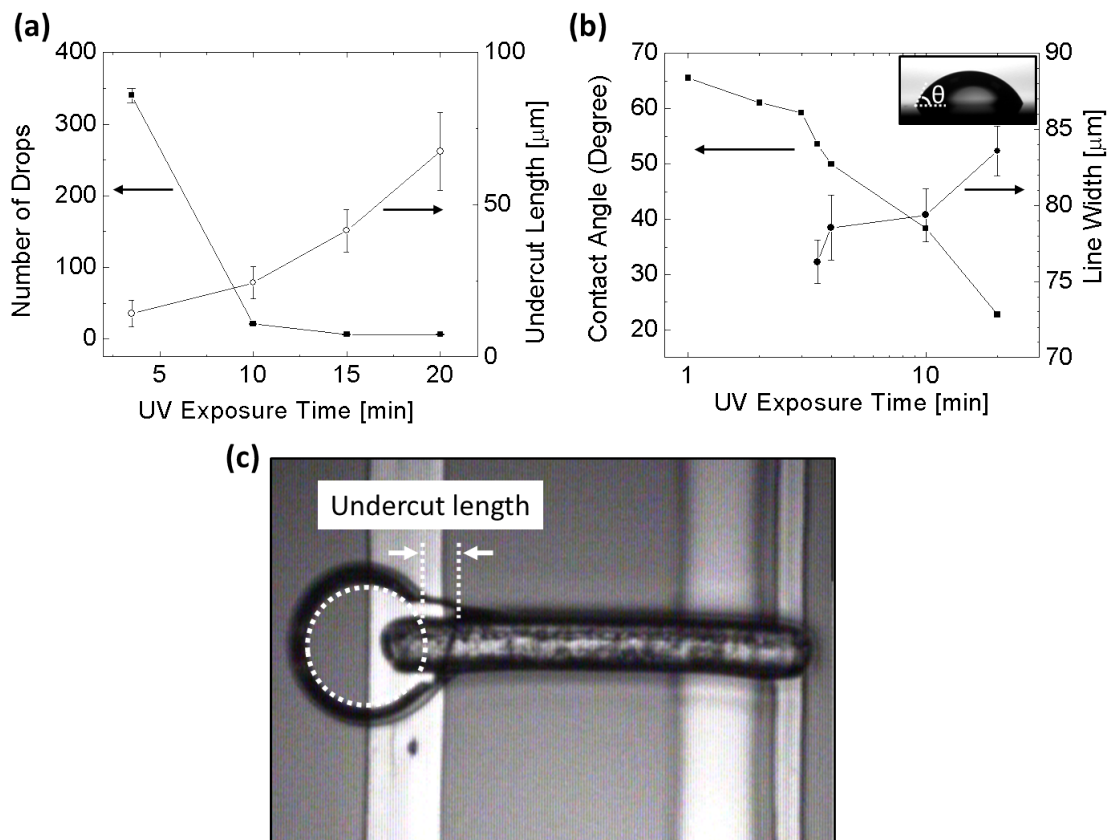


Figure 4.2: Effects of UV-ozone (UVO) exposure time on the process. (a) The number of drops to completely remove sacrificial PMMA and undercut length as a function of UVO exposure time. (b) The change of water contact angle of PMMA and minimum line width as UVO exposure time changes. (c) Undercut length is defined as the length of the extrusion from the imaginary boundary of the circular via-hole.

beam toward its free end. The undercut length is defined as the length of this extension from the imaginary boundary of the circular via-hole. This undercut length increases with the UVO exposure time because it makes PMMA more vulnerable to acetone, as shown in Fig. 4.2(b). The undercut is detrimental because it can cause variations in the length of the cantilever beam. When the via-hole is filled with Ag nanoparticle ink during the anchor formation, Ag ink can flow along the undercut, which in turn makes the beam length shorter than designed. Therefore, there is a trade-off between the process speed and its variation; the enhanced speed of the via-hole formation process due to the reduced number of drops required for complete removal of PMMA and potentially degraded process variation which may be caused by excessive amount of exposure to UVO. In this work, the UVO exposure time was set to 10 min. in order to balance the two effects.

An additional effect of the UVO treatment is the change of surface hydrophobicity [3, 4]. A

polymer surface is generally hydrophobic due to its low surface energy. Exposure of polymer to UVO is a widely used method to adjust its surface contact angle, for printed electronics. It was also used in this work for the beam printing process since the PMMA surface is hydrophobic as deposited and so it prevents adjacent droplets of printed Ag nanoparticle inks from merging together to form continuous patterns. A brief exposure (210 sec.) to UVO changes the surface hydrophobicity of the PMMA, and hence the beam can be successfully defined. The change of water contact angle shown in Fig. 4.2(a) as a function of UVO exposure time illustrates the change in surface energy with UVO exposure. There is also a trade-off here, since UVO exposure can adjust the surface hydrophobicity such that proper spreading conditions can be achieved and a continuous film can be formed, but excessive UVO exposure also increases the minimum linewidth of the printed features, as shown in Fig. 4.2(a). For scaling of the beam width, proper wetting conditions for the Ag nanoparticle ink on the sacrificial layer (e.g. PMMA) are necessary, and therefore the UVO exposure should be limited to balance the trade-off. It should be noted that the UVO treatment for beam formation occurs before the via-hole creation, and therefore excessive UVO treatment in beam formation process will also have implications for the following UVO treatment for the via-hole process.

4.3 Pull-in Voltage Reduction from Scaled Actuation Gap

With the aforementioned process optimizations, a reduction in operating voltage of the printed MEM switch was pursued. The pull-in voltage equation for the cantilever-type switch actuated by electrostatic force in this work is given again here for a reference:

$$V_{PI} = \sqrt{\frac{8}{27} \frac{k_{\text{eff}} g_o^3}{\epsilon_o A_a}} \quad (4.1)$$

where k_{eff} is the effective cantilever beam stiffness, g_o is the actuation gap (between the beam and the bottom gate electrode), ϵ_o is vacuum permittivity, and A_a is the actuation area (the overlap area between the beam and the gate electrode). As evident from Eq. (4.1), V_{PI} is dependent on mostly g_o among other parameters. It is therefore straightforward to scale down the pull-in voltage V_{PI} by reducing the actuation gap g_o , which can be pursued by adjusting the sacrificial layer thickness. The thickness of sacrificial PMMA layer can be adjusted by the speed of the spin-coat deposition, and it was varied as 1.65 μm , 1.25 μm , and 0.85 μm .

The measured drain current *vs.* gate voltage is shown in Fig. 4.3(a) for 1.65 μm and 0.85 μm g_o cases. The value of V_{PI} was reduced from ~ 16 V to ~ 5 V, as expected. The predicted values of V_{PI} from the scaled g_o were calculated (dotted line) and compared to the measured values (markers with error bars), as shown in Fig. 4.3(b). In order to calculate the predicted value of V_{PI} , k_{eff} values obtained from the nanoindentation measurement in Chapter 3 was

used. For the given dimensions of the beam in this work, the value of k_{eff} was measured to be $k_{\text{eff}} = 27.6 \text{ N/m}$ (See section 3.6) and it was used to calculate V_{PI} as function of g_o , with $A_a = 190 \mu\text{m}^2$ (gate width: $190 \mu\text{m}$ and beam width: $90 \mu\text{m}$). The measured V_{PI} of the scaled actuation-gap devices follows the predicted value calculated from the equation 4.1.

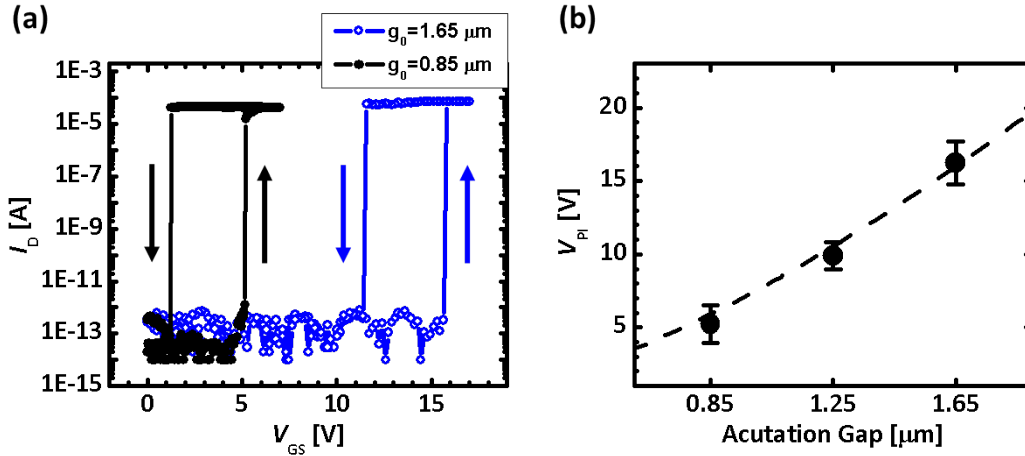


Figure 4.3: Measured current-voltage characteristics of scaled-gap printed switches. (a) Drain current *vs.* gate voltage measurements from two printed switches with different actuation gap thickness. Pull-in voltage was reduced from $\sim 16 \text{ V}$ to $\sim 5 \text{ V}$ as expected. (b) Measured and calculated values of pull-in voltages of printed switches with scaled actuation gaps.

It has also been tried to scale V_{PI} by changing the position of the actuating gate electrode. The effective beam stiffness k_{eff} is a function of the position of the applied load on the cantilever beam [5, 6] because the moment is proportional to the length of the torque. The original design of the MEM switch structure has the gate electrode closer to the anchor than the drain electrode. Therefore, it is worth trying to swap the roles of the two bottom electrodes, to obtain smaller k_{eff} by locating the gate at the end of the beam. The measured $I - V$ characteristic is shown in Fig. 4.4, where an actuation gap of $0.85 \mu\text{m}$ was used. The pull-in voltage indeed was reduced, compared to the switches with the same device dimensions but gate electrode closer to the anchor. However, it should be noted that this electrode configuration causes unstable physical contact between the beam and drain (contacting) electrode. This arises from the fact that the deflection of the beam over the drain electrode may not be sufficient to cause contact before the beam is pulled-in to contact the gate electrode. Therefore, it is not recommended to use this configuration even if there is a benefit in reduction of V_{PI} .

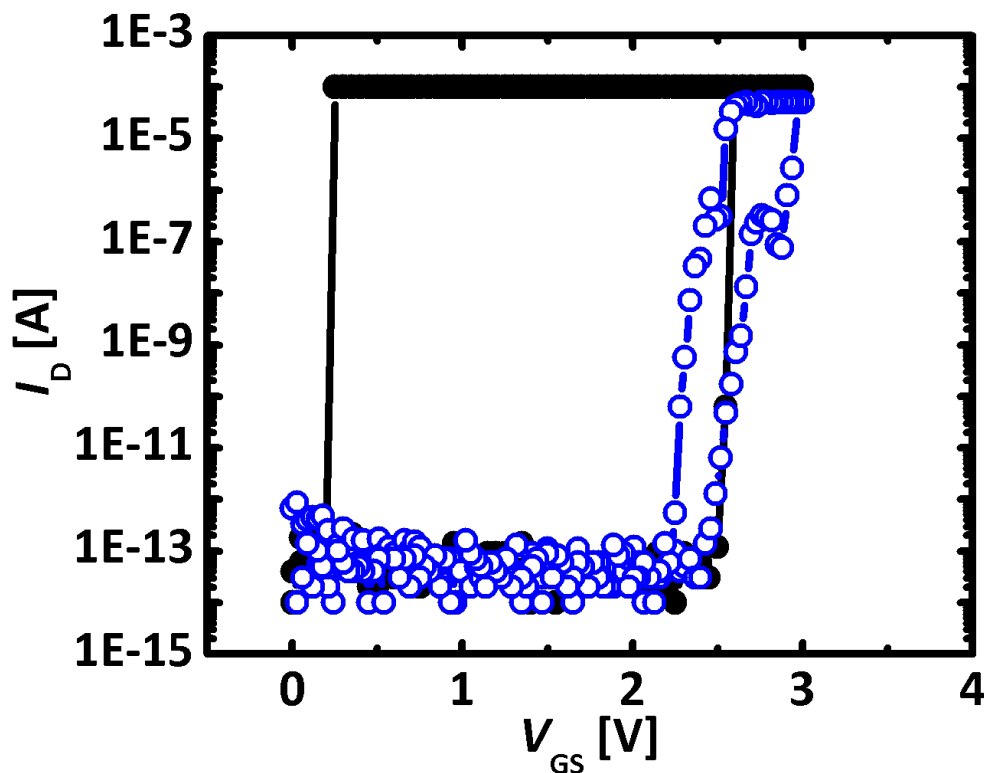


Figure 4.4: Measured current-voltage characteristics for two printed switches with the gate electrode farther from the anchor than the drain electrode. This configuration can effectively lower V_{PI} (both closed and open circle markers) but may cause unstable physical contact at the drain electrode due to insufficient beam deflection (open circle markers)

4.4 Conclusion

The performance of the printed MEM switch can be enhanced by reducing the operation voltage through scaling the actuation gap. It is straightforward to reduce the gap thickness by adjusting that of the sacrificial layer, and the pull-in voltage has larger dependency on the gap among other dimensions. The pull-in voltage of the switch was successfully reduced by $\sim 70\%$. Process optimization was carried out to facilitate gap scaling by studying the trade-offs for UVO exposure time, which impacts the throughput, variation, and scalability of the process.

Bibliography

- [1] Robert B Fox, Lawrence G Isaacs, and Suzanne Stokes. “Photolytic degradation of poly(methyl methacrylate)”. In: *Journal of Polymer Science Part A: General Papers* 1 (3) (Mar. 1963), pp. 1079–1086.
- [2] T Çaykara and O Güven. “UV degradation of poly(methyl methacrylate) and its vinyl-triethoxysilane containing copolymers”. In: *Polymer Degradation and Stability* 65 (2) (Aug. 1999), pp. 225–229.
- [3] Joseph Zelez. *SURFACE MODIFICATION OF PLASTIC SUBSTRATES, US Patent 5,098,618*. 1992.
- [4] Attila Oláh, Henrik Hillborg, and G.Julius Vancso. “Hydrophobic recovery of UV/ozone treated poly(dimethylsiloxane): adhesion studies by contact mechanics and mechanism of surface modification”. In: *Applied Surface Science* 239 (3-4) (Jan. 2005), pp. 410–423.
- [5] Gabriel M Rebeiz. *RF MEMS Theory, Design, and Technology*. John Wiley & Sons, Inc., 2003.
- [6] James Gere and Barry Goodno. *Mechanics of Materials*. 7th ed. CENGAGE Learning, Apr. 2008.

Chapter 5

Microshell Encapsulation using Inkjet-Printed Nanoparticle Films

5.1 Introduction

Microshell encapsulation processes have been developed for monolithic packaging of MEMS devices using polycrystalline silicon (poly-Si) as a porous encapsulation layer because it can be made permeable to HF when sufficiently thin [1] or electrochemically etched [2]. This reduces release times and penetration of the sealing material. The temperature required to form poly-Si ($> 600^{\circ}\text{C}$) is too high for CMOS backend integration [3], however, precluding the use of this technology in monolithically integrated microsystems. In this chapter, a low-thermal-budget ($< 300^{\circ}\text{C}$) microshell encapsulation process using inkjet-printed nanoparticle inks is proposed [4]. The nanoparticle ink consists of metal nanoparticles dispersed in solvent, where individual nanoparticles are encapsulated by organic capping material (ligands) to prevent aggregation. Multiple drops of the ink are deposited by inkjet printing onto the substrate to form a liquid film of the desired pattern. Afterwards, the solvent evaporates and the nanoparticles are sintered at an elevated temperature to form a solid metallic film. The minimum required sintering temperature depends on the size and structure of the nanoparticles and is usually much lower than the melting point of bulk materials, due to an increased surface-to-volume ratio [5]. For microshell encapsulation applications, it is advantageous that the porosities of such printed nanoparticle films can be controlled by the size and structure of the nanoparticles and sintering conditions. Furthermore, the sintering temperature is usually low enough such that the entire process is CMOS compatible.

5.2 The Microshell Material Requirements

As described in Chapter 1, there are two approaches to zero-level packaging [6]; (a) a separate cap is bonded into the device region to be protected, or (b) thin-film material is deposited to encapsulate individual devices. The latter approach is called microshell encapsulation and

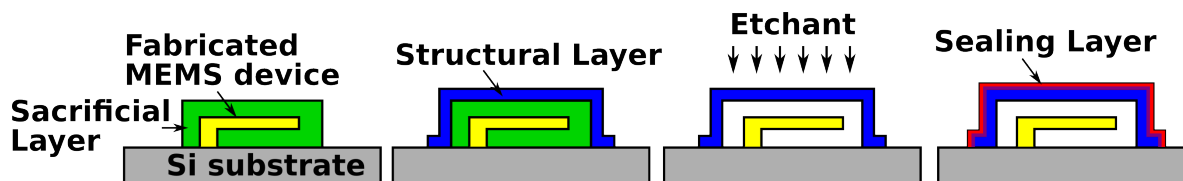


Figure 5.1: Process flow for microshell encapsulation. (a) Sacrificial layer is deposited and patterned to encapsulate devices. (b) The microshell material is deposited to coat the patterned sacrificial layer to define microshell structural layers. (c) The encapsulated devices are released by flowing an etchant material through the structural layer to remove the sacrificial layer. (d) Sealing layer is deposited in a controlled environment (e.g. high vacuum or inert gas ambient).

has been applied to various MEMS devices [1, 2, 6, 7, 8], whose general process flow is shown in Fig. 5.1. In a standard surface micromachining process used for MEMS device fabrication, the sacrificial layer is removed to release structures upon completion of device fabrication. But for microshell encapsulation processes, an additional sacrificial layer is deposited and patterned such that the devices can be encapsulated (Fig. 5.1(a)). The microshell material is deposited to coat the patterned sacrificial layer to define microshell structural layers (Fig. 5.1(b)).

Afterwards, the encapsulated devices are released by flowing an etchant material through the structural layer to remove the sacrificial layer (Fig. 5.1(c)). This step sets up two requirements for the structural layer; it should be permeable to the selected etchant to enable the removal of the sacrificial layer encapsulated by it, and it should also have sufficient mechanical strength so that it can be free-standing without structural collapse upon release. These two requirements can conflict each other because a film can be made to be permeable to gas or liquid if it is sufficiently thin, but it is necessary to be thickened above a certain critical thickness to avoid structural collapse. Conventionally, thin polycrystalline films, such as poly-Si, have been used for the structural layer due to their permeability to oxide etchants (gas or liquid phase hydrofluoric acid (HF)) [1, 9]. The poly-Si layer is usually made very thin ($< 100 \sim 200$ nm [1]) to achieve permeability to gas/liquid HF, and it requires additional structural support from a thick frame to compensate for its lack of mechanical strength [1].

Figure 5.2 shows the schematic of an archetypal microshell process flow which employs such frame-supported microshells with etch-access windows. An example of this scheme was reported in Ref [1], where etch-access windows of thin (~ 95 nm) poly-Si were defined by thicker ($\sim 1.4\mu\text{m}$) frames of low-stress silicon nitride and the size of the etch-access windows were decided by taking into account of the trade-off between etch-rate and structural robustness [1]. The structural layer, which forms the microshell, and the permeable layer, which is used as a thin membrane that allows etchant to penetrate into the microshell, are separated in this scheme. After the structural material is deposited and patterned to have etch-access windows (Fig. 5.2(a)), a thin film of permeable material is deposited (Fig. 5.2(b)). This thin

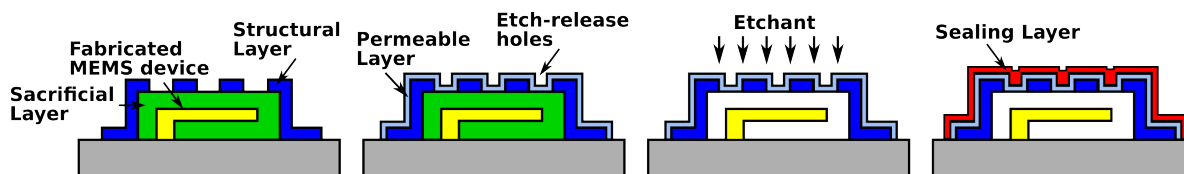


Figure 5.2: Process flow for microshells employing etch-access windows. (a) The structural material is deposited and patterned to have etch-access windows, (b) a thin film of permeable material is deposited, (c) the etchant penetrates the permeable material to remove the sacrificial layer, (d) a sealant is deposited.

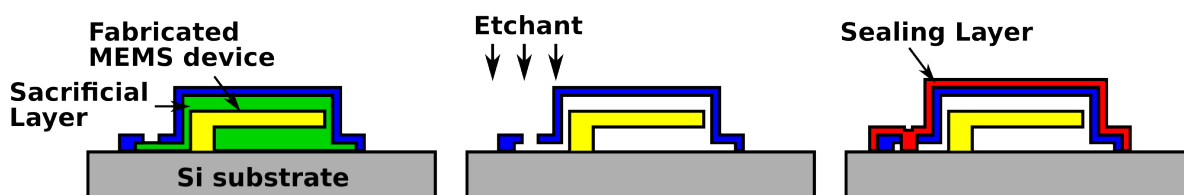


Figure 5.3: Process flow for microshells employing etch-release holes. (a) Structural layer is deposited and patterned to have etch-release holes after the sacrificial layer was patterned to have footing regions where etch-release holes can be incorporated. (b) Sacrificial layer is removed by etchant that flows into the microshell through the etch-release holes. (c) Sealing material is deposited such that the etch-release holes is sealed.

film of permeable material allows the etchant to remove the sacrificial layer (Fig. 5.2(c)), and blocks the sealant from depositing inside microshell cavity (Fig. 5.2(d)). It is also possible to avoid the use of a reinforcing frame by making the structural layer thick to have sufficient mechanical strength with separate etch-release holes [7, 8], as shown in Fig. 5.3. In this process, the etchant penetrates the microshell not through the structural layer but through etch-release holes. The structural layer is deposited and patterned to have etch-release holes after the sacrificial layer is patterned, to create footing regions with etch-release holes incorporated (Fig. 5.3(a)). The sacrificial layer is removed by etchant that flows into the microshell through the etch-release holes (Fig. 5.3(b)). Sealing material is then deposited such that the etch-release holes are sealed (Fig. 5.3(c)). *Lin* showed in Ref. [7] that 1 μm -thick LPCVD low-stress silicon nitride film can be deposited to form the microshell with etch-release holes and that a sacrificial phosphorus-doped silicate glass layer ($\sim 7 \mu\text{m}$) can be successfully removed by exposure to concentrated HF solution for 5 min.

The final step of microshell fabrication process is to seal the structural layer in a controlled ambient, such as high vacuum or inert gas, to encapsulate the MEMS devices with a hermetic seal in a desired environment. This step also puts an additional stringent requirement on the material properties of the structural layer; it should be sufficiently dense to prevent the sealant from penetrating into the microshell cavity and being deposited onto the encapsulated devices. If the sealing material is deposited onto the packaged devices,

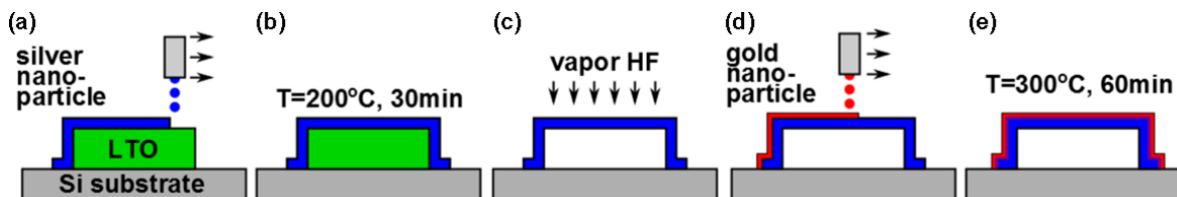


Figure 5.4: Schematic illustration of inkjet-printed microshell encapsulation process. (a) Silver nanoparticles (50 nm) in solution are inkjet-printed. (b) The printed silver nanoparticles are sintered (at 200°C for 30 min) to form a porous microshell. (c) Sacrificial oxide is removed by an HF vapor etch process. (d) Gold nanoparticles (5 nm) in solution are inkjet-printed and (e) annealed (at 300°C for 60 min) to seal the microshell.

mechanical or electrical properties can be accidentally altered, which may cause undesirable changes in the device performance.

Therefore, it is important to choose a proper material for the structural layer such that it can satisfy all the stringent requirements described above. A nanoparticle film deposited by inkjet-printing is a promising candidate in this regard because it can be thickened using multi-layer deposition to achieve high mechanical strength and its porosity can be controlled either by the particle size or annealing temperature. Furthermore, the process temperature can be CMOS-compatible since the temperature to anneal the printed nanoparticle film is relatively low ($< 300^{\circ}\text{C}$) due to the enhanced surface-to-volume ratio of nanoparticles [5].

5.3 Inkjet-Printed Microshell Process

The steps used in the proposed inkjet microshell encapsulation process are illustrated in Figure 5.4. For initial proof of concept, only a sacrificial layer of low-temperature-deposited silicon dioxide (LTO), 1.3 μm thick, was deposited and patterned into islands of various lateral dimensions. The microshell is formed by inkjet-printing a solution containing Ag nanoparticles (50 nm in diameter) to encapsulate the sacrificial oxide. The printed liquid film is then sintered on a hot plate (after ramping up the temperature at a rate of 5°C/min) to evaporate the solvent and form a solid film.

Figure 5.5 shows a printed Ag nanoparticle film that encapsulates two oxide islands, where (a) as-printed liquid film is patterned by inkjet-printing and (b) solid film is formed after annealing. A drop spacing of 25 μm was used and the substrate temperature was held at room temperature during printing. Drops of nanoparticle ink pin on the substrate and form a thin film of liquid by merging with adjacent drops. During the annealing process, the solvent and the ligands that encapsulated the individual nanoparticles in the solution to separate and prevent the particles from aggregating evaporate [10, 11]. It is during this process that individual nanoparticles consolidate to form a solid film. The thickness of the resulting solid film is an important parameter to be controlled in order for the microshell to

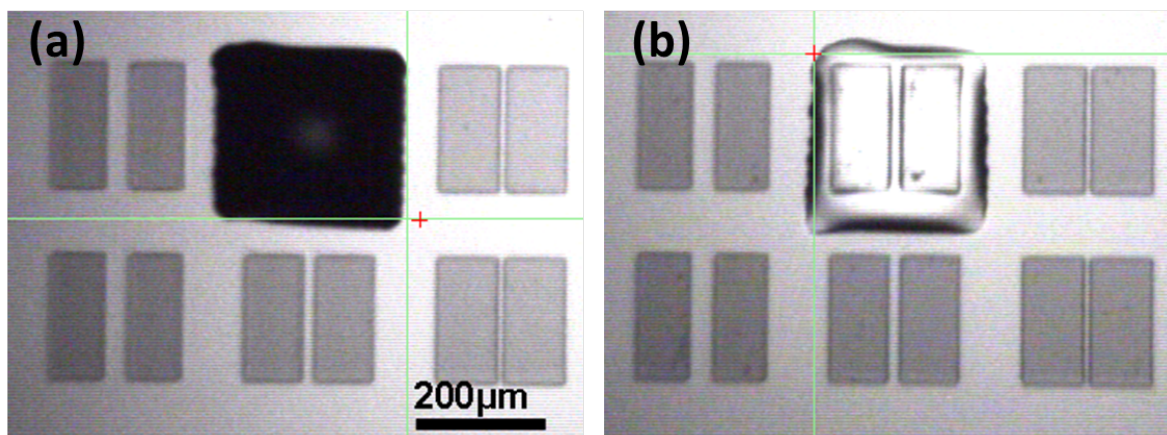


Figure 5.5: Micrographs of inkjet-printed Ag microshell. (a) As printed, the liquid Ag film encapsulates the patterned sacrificial oxide. (b) The Ag film is solid after drying to evaporate the solvent.

obtain sufficient mechanical strength and avoid structural collapse upon release. Figure 5.6 shows how the thickness of the printed film increases with the number of printed layers, for two different sintering temperatures (200°C and 400°C). Each printed layer of Ag liquid film is dried at 100°C for 10 min to evaporate the solvent, before any subsequent layer is printed.

The interspersed drying steps are necessitated because the thickness of printed film can be adjusted more accurately by printing additional ink on top of a solid film, rather than on a liquid one, for the following reasons. First, the amount of liquid which can be deposited inside a certain area on a partially wetting surface is limited in equilibrium [12, 13]. Excessive volume of liquid will result in the deformation of printed patterns and may even cause bulge instability [14]. Secondly, a coffee-ring effect may be exacerbated in a larger volume of liquid, which will cause non-uniformity in the dried film morphology due to increased evaporation time [15]. Finally, thicker films are more prone to stress-induced crack formation in the film during the annealing process [16]. Therefore, it is beneficial to print multiple layers and limit the thickness of each solid film to minimize the possibility of crack formation. Figure 5.7 shows printed nanoparticle films composed of multiple layers, where the deposited inks were dried at 60°C in the interspersed drying steps. Non-uniform surface morphology, such as wrinkles on the surface, occurred on the films upon drying the 4th layer, while uniform and smooth surface without wrinkles were obtained when films were dried at or above 100°C. Incomplete drying may have caused such wrinkles because of the residual solvent or polymers used for nanoparticles in the ink may have evaporated from the partially dried films while drying the films deposited above it.

During the sintering process, the ligands that encapsulated the nanoparticles in the printed liquid film evaporate and diffuse away, so that the center-to-center distance between neighboring nanoparticles decreases, allowing them to merge and form a continuous

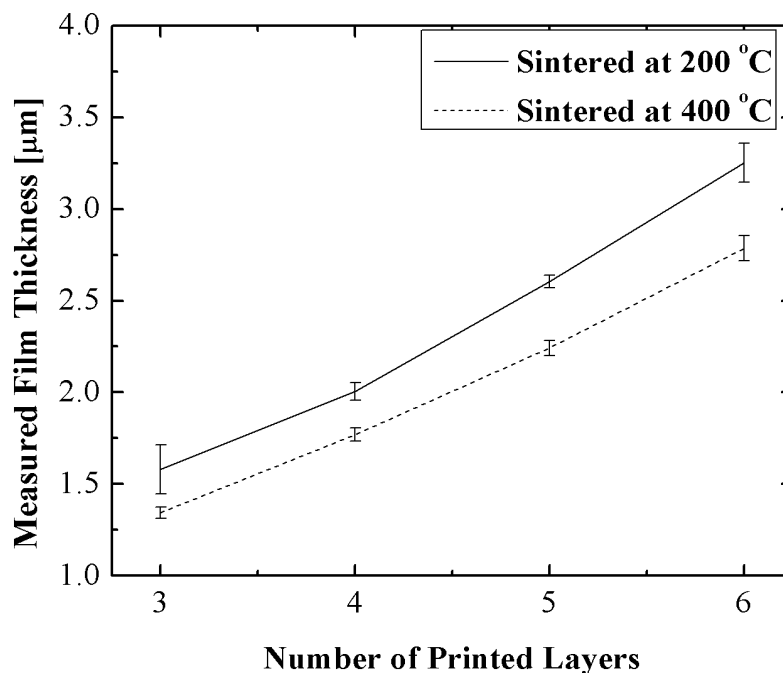


Figure 5.6: Measured thicknesses of inkjet-printed films after sintering at 200°C and 400°C.

film [16]. Voids resulting from the removal of the capping ligands result in porosity in the printed nanoparticle film, especially if the nanoparticles are of larger size. The porosity makes the film permeable to HF vapor, which allows the underlying sacrificial oxide to be rapidly removed. Higher sintering temperature enhances ligand removal (limited by diffusion for such thick films) and additionally facilitates the coalescence of the nanoparticles, resulting in smaller average pore size and hence a thinner film.

The printed Ag microshells were verified to be permeable to HF vapor. Figure 5.8 shows a cross-sectional scanning electron micrograph of a “released” microshell. The sacrificial oxide island had a width of $100\mu\text{m}$, a length of $200\mu\text{m}$, and a thickness of $1.3\mu\text{m}$, and was removed completely by a brief (5 min.) HF vapor etch to form the cavity. It can be verified that the released microshell is mechanically strong enough that it is not collapsed throughout the whole cavity region as shown in Fig. 5.8(a). The corner of the cavity, where the microshell is anchored, is shown at higher magnification in Fig. 5.8(b), and sacrificial oxide is not observed inside the cavity, verifying the complete removal of the oxide by HF vapor etch.

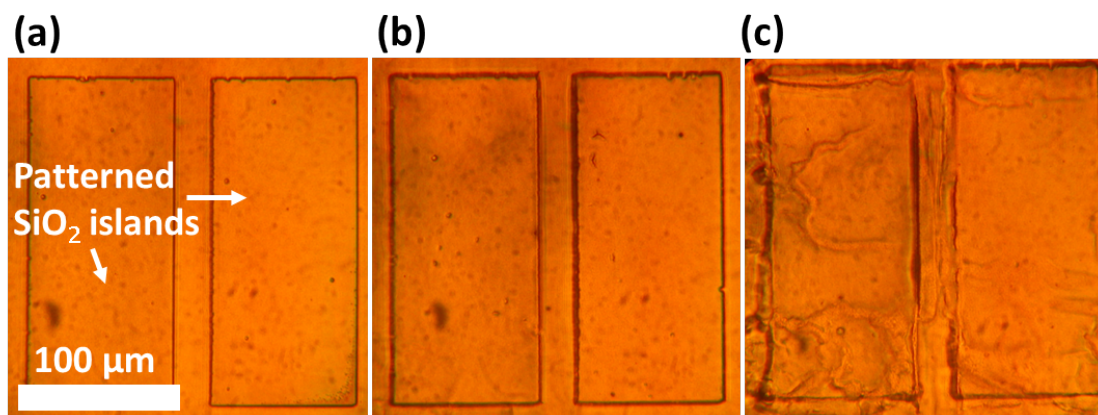


Figure 5.7: Micrographs of dried inkjet-printed nanoparticle films composed of multiple layers, dried at 60°C. Images were taken after (a) the first layer deposited and dried, (b) second layer, and (c) fourth layer. Non-uniform surface morphology, such as wrinkles on the surface, occurred on the films upon drying the 4th layer.

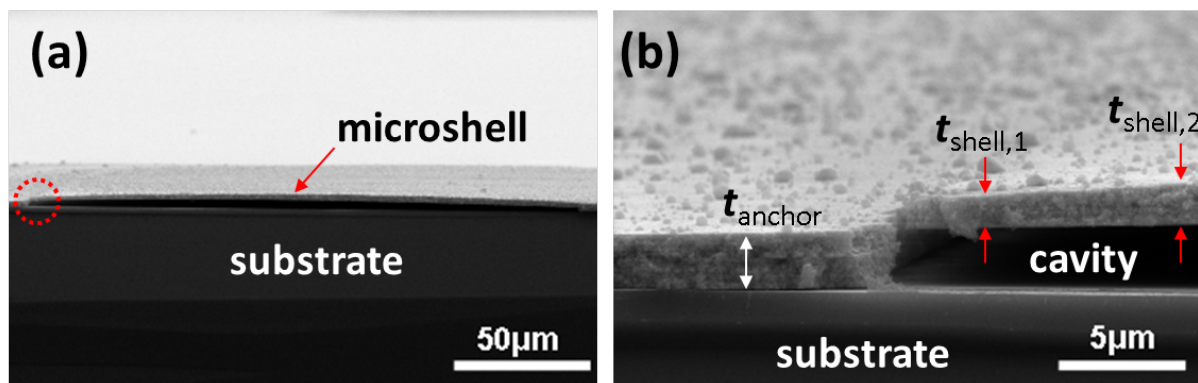


Figure 5.8: Cross-sectional SEM images of an inkjet-printed Ag microshell after exposure to HF vapor indicate that it is (a) free-standing, and (b) a porous structure.

5.4 Structural Properties of the Printed Microshell

If the microshell is too thin ($< 2\mu\text{m}$ thick) then it will collapse upon removal of the underlying oxide. Figure 5.9 shows surface topography maps of printed Ag microshells, before and after removal of underlying sacrificial oxide in HF vapor. The line profiles for the microshell fabricated by printing 3 layers ($\sim 1.5\mu\text{m}$ total thickness) clearly show that it lacks the necessary mechanical strength, so that it is collapsed after release. The inset of Fig. 5.9(a) shows the comparisons of line profiles for the microshells between before (indicated as red line) and after (white line) the release, where white line (after release) does not follow the red line (before release) at the microshell region. Microshells of various film thicknesses were fabricated to find an optimal thickness which can give necessary mechanical strength to avoid such collapse. The thickness of the film was adjusted by the number of printed layers as shown in Fig. 5.6. A thickness of $\sim 2.5\mu\text{m}$ was found to be sufficient for forming microshells with lateral dimensions exceeding 1 mm in length, as shown in Figure 5.9(b), where negligible difference was observed in the line profiles for the microshells before and after the removal of the encapsulated sacrificial oxides, and Table 5.1.

5.5 Sealing Microshell with Finer-Sized Nanoparticles

In order to seal the microshell (after the HF vapor release etch), a solution containing Au nanoparticles of much smaller size (~ 5 nm in diameter) is inkjet-printed and sintered in a tube furnace at 300°C for 60 min. Figure 5.10(a) shows a cross-sectional scanning electron micrograph of an Ag film fabricated by inkjet-printing 5 layers of Ag nanoparticle ink (total thickness $\sim 2.5\mu\text{m}$) and sintering at 200°C for 30 min. The porous structure is clearly evident, as are the grains formed by merged nanoparticles. The smaller Au particles completely fill the voids in the outermost portions of the Ag film, as can be seen in Figure 5.10(b).

The effectiveness of the Au seal was tested by exposing an unreleased and sealed microshell to HF vapor. It was found that the sealed microshell is not permeable to vapor HF, because the remaining oxide thickness after a 10-min. exposure to HF vapor was measured to be the same as originally deposited (Figure 5.11). The thickness of oxides before and after the etch process have been measured for comparison using a contact profilometer (alpha-step IQ surface profiler). Different amounts of Au ink were deposited by varying the number of printed layers and it was found that printing more than 3 layers of Au ink was sufficient to effectively seal the porous Ag films by filling the voids. Partial removal of oxide by vapor HF etch was observed for the case of depositing less than 3 layers of Au ink.

As mentioned above, the microshell must be sufficiently thick to avoid collapse upon release. Stress-induced cracks can form more easily in thicker films, however, due to volume reduction during the sintering process [16, 17]. Also, non-uniform solvent evaporation and internal stress due to differences between the coefficients of thermal expansion for the film and the substrate can initiate cracking inside the film [18]. To suppress cracking, an intermediate sintering step (200°C for 30 min.) was performed after printing the first 3 layers. This

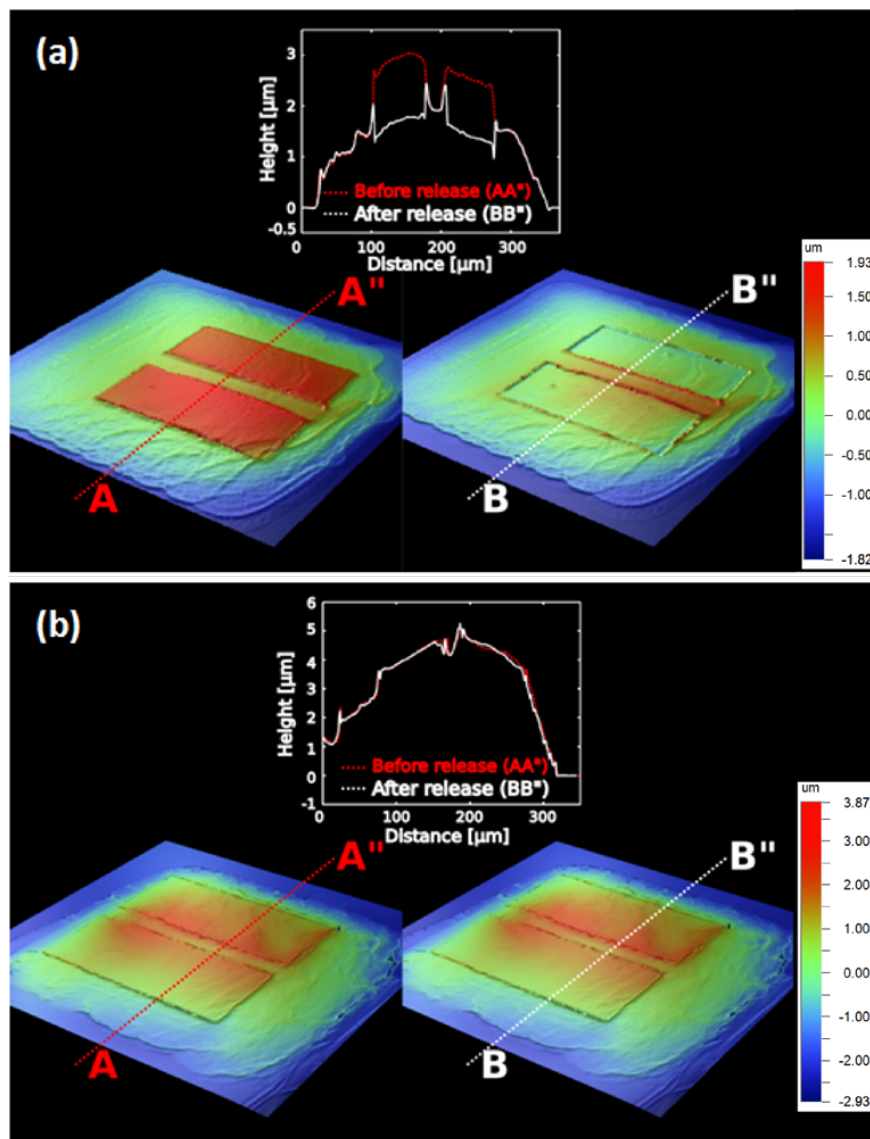


Figure 5.9: Measured height profiles of inkjet-printed microshells before (AA^{*}) and after (BB^{*}) HF vapor etch, obtained with an optical profilometer. (a) 1.4 μm-thick microshell is collapsed after release. (b) 2.7 μm-thick microshell is free-standing after release.

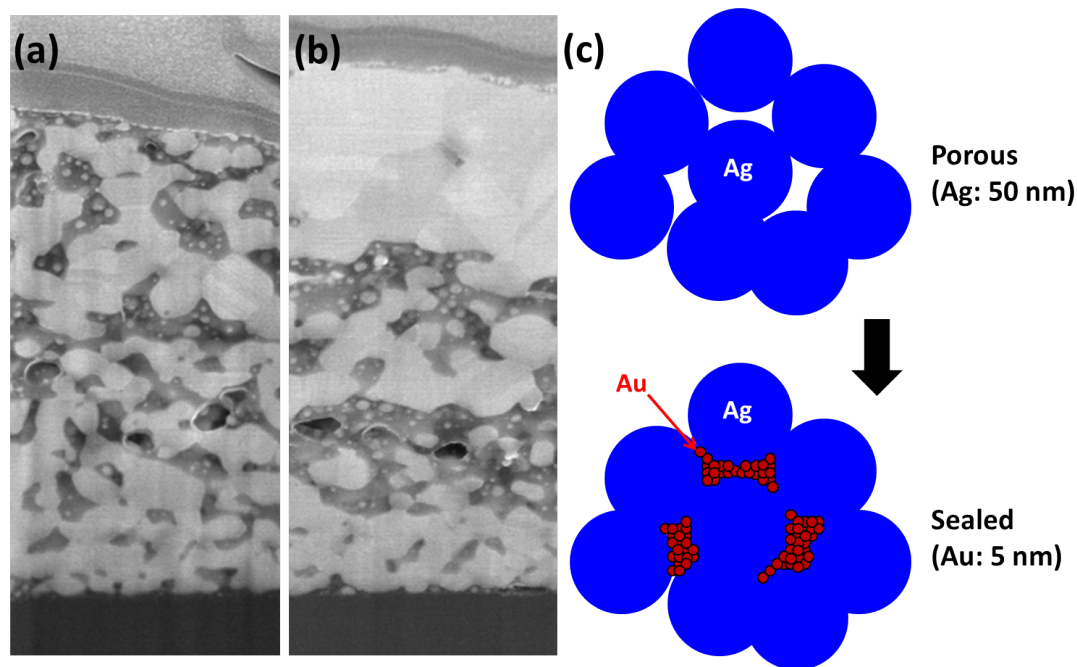


Figure 5.10: Cross-sectional SEM images of printed nanoparticle films. (a) Ag nanoparticle (50 nm) film after sintering. A porous structure is clearly evident. (b) Au nanoparticle (5 nm) sealed Ag film. The upper portion of the film is dense (not porous), indicating that the finer Au nanoparticles effectively fill the voids in the upper portion of the Ag film. The scale bars each are 500 nm long. (c) Schematics illustrates that a solution containing Au nanoparticles of much smaller size (~ 5 nm in diameter) fill the voids of the porous structure in larger size (~ 50 nm in diameter) Ag nanoparticle film.

reduces both the amount of residual solvent that has to diffuse out from the film and the total thickness of the film during the subsequent sintering steps. Figure 5.12 compares the surface topographies of two microshells fabricated with 5 printed Ag layers: the one mapped in Figure 5.12(a) underwent an intermediate sintering step whereas the one mapped in Figure 5.12(b) did not. Regions indicated by arrows in Fig. 5.12 show the opening of the shells by cracking. This is evident from the fact that blue color was mapped, which indicates lower value of height in the topographical maps while the red color is used for higher value. It should be noted that the most of the crack openings occurred at the edge of the shell, where the maximum value of stress usually occurs [19]. It can be seen that crack formation is effectively suppressed with the intermediate sintering step.

Because some layout area is required to anchor a microshell, it is desirable to encapsulate many devices with a single microshell, for good area efficiency. Microshells of various dimensions were fabricated and the vertical deflections at their center points after HF vapor release were measured by an optical profilometer. The results are summarized in Table 5.1. The microshell width (W) was $50\mu\text{m}$, $100\mu\text{m}$, or $150\mu\text{m}$, and the microshell length (L) ranged

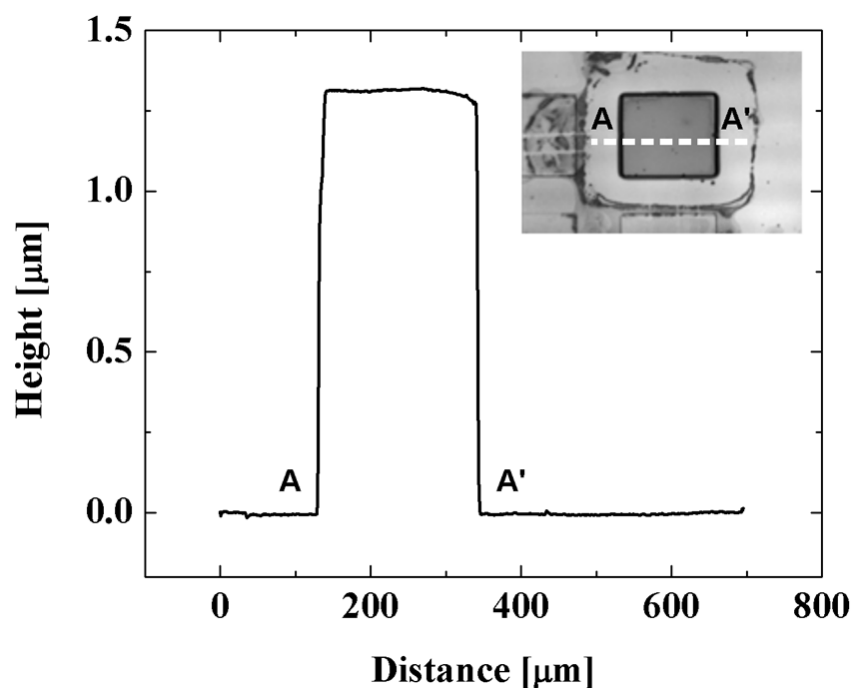


Figure 5.11: Measured profile of the encapsulated sacrificial oxide after exposure of its sealed microshell to HF vapor and subsequent removal of the microshell by wet etching. (Inset: optical micrograph of the remaining oxide island).

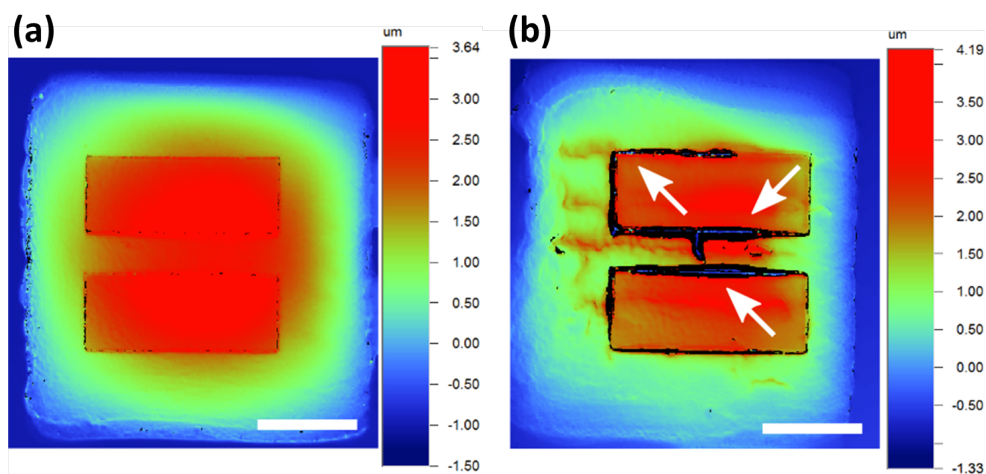


Figure 5.12: Measured height profiles of microshells fabricated with differences in the sintering process. (a) Microshell formed with an intermediate sintering step after the first 3 Ag layers were printed, as well as a sintering step after all 5 Ag layers were printed. (b) Microshell formed with only a sintering step after all 5 Ag layers were printed. The scale bar is 100 μm long.

L/W \ W	50	100	150
1	50	100	150
2	100	200	300
4	200	400	600
8	400	800	1200
16	800	1600	2400
32	1600	3200	4800
64	3200	6400	
128	6400		

Table 5.1: Length (L) values (in μm) of microshells investigated in this work. Grey-shading indicates that the microshell collapsed after release. The microshell film thickness is $3.0\mu\text{m}$.

from $1\times$ to $64\times$ the width. The narrowest ($W = 50\mu\text{m}$) microshells do not collapse for the entire range of L values investigated, indicating promise for encapsulation of multiple devices within a single microshell. It should be noted that the shells of larger aspect ratios eventually collapse, whereas the ones of the same width and smaller aspect ratios are intact and free-standing. This may result from the non-uniform film thickness of the printed film.

5.6 Conclusion

Printed silver nanoparticle (~ 50 nm) films of thickness greater than $\sim 2.5\mu\text{m}$ have sufficient mechanical strength to be used for microshell encapsulation of MEMS devices while being permeable to vapor HF to allow for short release times. They can be effectively sealed with a printed gold nanoparticle (~ 5 nm) film. The low thermal budget ($\leq 300^\circ\text{C}$) of a printed microshell encapsulation process makes it attractive for low-cost packaging of monolithically integrated microsystems.

Bibliography

- [1] K.S. Leboutitz et al. “Vacuum encapsulation of resonant devices using permeable polysilicon”. In: *Micro Electro Mechanical Systems, 1999. MEMS '99. Twelfth IEEE International Conference on.* 1999, pp. 470–475.
- [2] Rihui He and Chang-Jin C.-J. Kim. “On-Wafer Monolithic Encapsulation by Surface Micromachining With Porous Polysilicon Shell”. In: *Journal of Microelectromechanical Systems* 16 (2) (Apr. 2007), pp. 462–472.
- [3] H Takeuchi et al. “Thermal budget limits of quarter-micrometer foundry CMOS for post-processing MEMS devices”. In: *Electron Devices, IEEE Transactions on* 52 (9) (2005), pp. 2081–2086.
- [4] E S Park et al. “Inkjet-printed microshell encapsulation: A new zero-level packaging technology”. In: *Micro Electro Mechanical Systems (MEMS), 2012 IEEE 25th International Conference on.* 2012, pp. 357–360.
- [5] Ph. Buffat and J-P. Borel. “Size effect on the melting temperature of gold particles”. In: *Physical Review A* 13 (6) (1976), pp. 2287–2289.
- [6] K Najafi. “Micropackaging technologies for integrated microsystems: Applications to MEMS and MOEMS”. In: *Micromachining and Microfabrication* 4979 (2003), pp. 1–19.
- [7] Liwei Lin. “Selective encapsulations of MEMS: Micro channels, needles, resonators and electromechanical filters”. Ph. D. University of California at Berkeley, 1993.
- [8] C H Mastrangelo, J.H.-J. Yeh, and R S Muller. “Electrical and optical characteristics of vacuum-sealed polysilicon microlamps”. In: *Electron Devices, IEEE Transactions on* 39 (6) (1992), pp. 1363–1375.
- [9] M W Judy and R T Howe. “Polysilicon hollow beam lateral resonators”. In: *Micro Electro Mechanical Systems, 1993, MEMS '93, Proceedings An Investigation of Micro Structures, Sensors, Actuators, Machines and Systems. IEEE.* 1993, pp. 265–271.
- [10] Madhusudan Singh et al. “Inkjet printing-process and its applications.” In: *Advanced materials (Deerfield Beach, Fla.)* 22 (6) (Feb. 2010), pp. 673–85.
- [11] Alexander F Routh. “Drying of thin colloidal films.” In: *Reports on progress in physics. Physical Society (Great Britain)* 76 (4) (Apr. 2013), p. 046603.

- [12] PG De Gennes. “Wetting: statics and dynamics”. In: *Reviews of modern physics* 57 (3) (1985), pp. 827–863.
- [13] Reinhard Lipowsky et al. “Droplets, bubbles, and vesicles at chemically structured surfaces”. In: *Journal of Physics: Condensed Matter* 17 (9) (Mar. 2005), S537–S558.
- [14] Jonathan Stringer and Brian Derby. “Formation and stability of lines produced by inkjet printing.” In: *Langmuir : the ACS journal of surfaces and colloids* 26 (12) (July 2010), pp. 10365–72.
- [15] Heather Meloy Gorr, Joshua M Zueger, and John a Barnard. “Characteristic size for onset of coffee-ring effect in evaporating lysozyme-water solution droplets.” In: *The journal of physical chemistry. B* 116 (40) (Oct. 2012), pp. 12213–20.
- [16] Julia R. Greer and Robert a. Street. “Thermal cure effects on electrical performance of nanoparticle silver inks”. In: *Acta Materialia* 55 (18) (Oct. 2007), pp. 6345–6349.
- [17] a L Yarin et al. “Lines of dense nanoparticle colloidal suspensions evaporating on a flat surface: formation of non-uniform dried deposits.” In: *Journal of colloid and interface science* 294 (2) (Feb. 2006), pp. 343–54.
- [18] Julia R. Greer and Robert A. Street. “Mechanical characterization of solution-derived nanoparticle silver ink thin films”. In: *Journal of Applied Physics* 101 (10) (May 2007), pp. 103529–5.
- [19] Stephen D Senturia , *Microsystem design*. English. Boston: Kluwer Academic Publishers, 2001.

Chapter 6

Integration of Printed Microshell with Relay Fabrication for Improved Contact Stability

6.1 Introduction

Micro-electro-mechanical (MEM) relays have gained interest again recently as an alternative technology for low-power logic devices, because the benefits from scaling conventional CMOS transistors in terms of performance and power consumption are diminishing. The MEM relays can perform the same functionalities as their solid-state transistor counterparts, with steeper switching characteristics and low leakage current [1]. Figure 6.1 illustrates the structure and operating principle of a six-terminal MEM relay that can incorporate multiple device functionalities into a single relay [2]. A plan view of the relay (Fig. 6.1(a)) shows various electrodes; the movable body electrode can be actuated by applying voltage on the gate electrode; conductive channels attached to the movable bandy can form an electrical paths between the source and drain electrodes. Cross-sectional views along the A-A line in Fig. 6.1(a) are shown for the case of the OFF-state (Fig. 6.1(b)) and ON-state (Fig. 6.1(c)). This device has a fundamentally similar operating principle to the 3-terminal MEM switch shown in Chapter 3, except for the fact that there is an additional (body) electrode that separates the electrode which responds to the actuating electrostatic force from the one which conducts current between the source/drain electrodes. In the OFF-state, the air gap separates the conductive channel on the bottom of the body from the source/drain electrodes, and thus no current flows. On the other hand, the movable body electrode can be pulled-in by electrostatic force when the applied voltage on the gate electrode is above the pull-in voltage. This results in physical contact between the channel and the source/drain electrode, and an electrical path is created in the ON-state (Fig. 6.1 (c)). When the V_{GS} is lowered below the release voltage V_{RL} , the spring restoring force of the beam will pull off the body electrode so that the electrical path be broken.

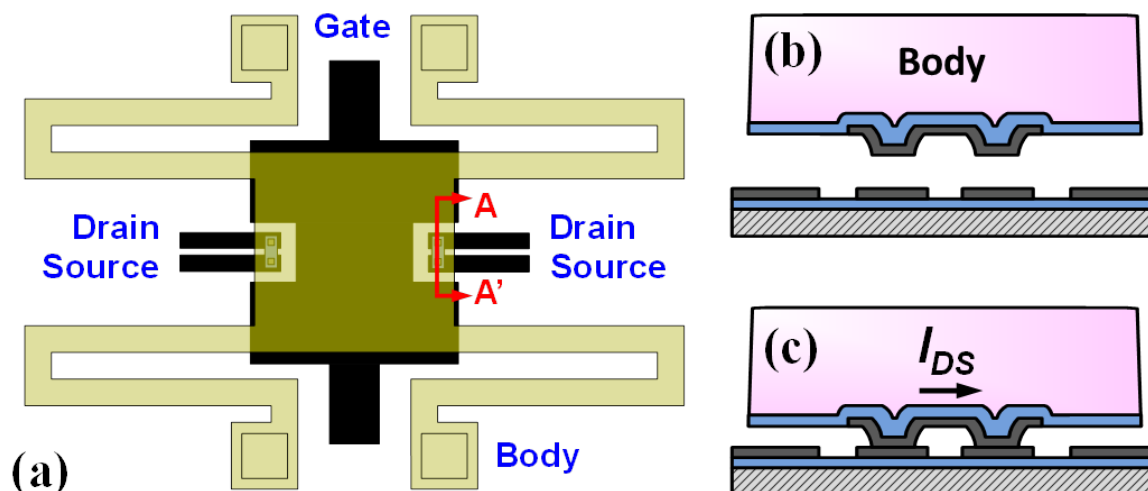


Figure 6.1: Schematic diagram illustrating the structure and operating principle of a six-terminal MEM relay in this work: (a) A Plan view of the relay shows various electrodes. (b) Cross-sectional view along A-A' line shows the position of the movable electrode in the OFF-state and (c) in the ON-state.

It is important to select a proper contact material that has good electrical conductivity as well as physical hardness because the conductive channel must make a physical contact with the drain and source electrode to form the electrical path. Tungsten (W) was chosen as the contacting electrode due to its excellent mechanical hardness that reduces physical wear and micro-welding [3]. A drawback of using W as the contacting electrode is that its electrical conductivity degrades once oxidized, which is likely to happen over the device operational lifetime, especially when Joule heating from the electrical current exacerbates the situation. Therefore, a hermetic package is necessary to reduce the contact oxidation and improve the contact resistance stability.

The inkjet-printed microshell encapsulation technology described in Chapter 5 has been employed to provide the MEM relays with a hermetic package for improved contact stability. The CMOS-compatible process (due to its low thermal budget) has successfully been applied and the contact resistance stability was enhanced by $\sim 100\times$.

6.2 Process Integration of Inkjet-Printed Microshell

The fabrication process for integration of printed microshell on MEM relays is illustrated in Fig. 6.2. Electrical connections to the electrodes of the MEM relays were insulated from the surface by inter-layer dielectric (80 nm Al_2O_3) to avoid electrical shorting to the microshell, since the microshell material is formed using electrically conductive silver (Ag) nanoparticles (Fig. 6.2(a)). Upon the completion of the MEM relay fabrication, sacrificial oxide (low-

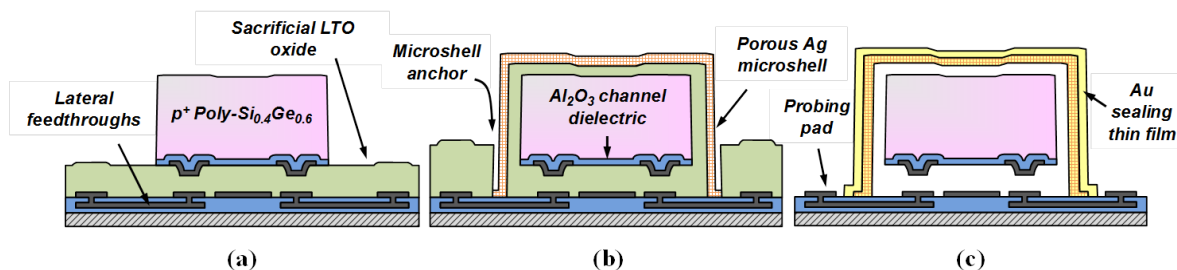


Figure 6.2: Schematic illustration of the fabrication process for encapsulating a relay in a microshell.: (a) completed relay with connections to electrodes routed through an underlying layer of Al₂O₃; (b) deposition and patterning of a capping sacrificial layer to define microshell anchor regions, followed by Ag nanoparticle inkjet printing to form a porous microshell; (c) vapor HF etch to release the structure through the microshell, followed by Au nanoparticle inkjet printing to seal microshell.

temperature oxide, 800 nm) was deposited and patterned into islands to isolate the MEM relays (Fig. 6.2(b)). The connections to the external contact electrodes were also coated by this sacrificial LTO, resulting in trench-like structures around the encapsulated devices, which provides the footing regions for the microshell. Next, Ag nanoparticles were deposited by inkjet-printing to define the microshell structure (Fig. 6.2(b)), which becomes a porous solid film upon annealing (180°C 30 min.). Afterwards, the wafer is exposed to vapor-phase hydrofluoric acid (HF) to release the encapsulated MEM relays by removing the sacrificial LTO and forming the cavity inside the microshell. Finally, the sealing layer was deposited by inkjet-printing finer-sized gold (Au) nanoparticles (~ 5 nm in diameter) to fill the voids on the outermost part of the porous printed Ag microshell film (Fig. 6.2(c)). Then, the devices were annealed inside a glove-box, where the oxygen level was kept low (< 5 ppm) at 200°C (after ramped up at 2°C/min.).

Alternatively, a polymeric material can be used as a sealant. In this work, the amorphous cyclic transparent optical polymer (Cytop, Asahi Glass, Japan), which has very low oxygen permeability (8.34×10^{-10} cm³·cm/cm²·s·cmHg) was investigated as an alternative sealant. For demonstration purposes, it was deposited by spin-coating (to a thickness of ~ 1 μm) inside the glovebox and cured in situ at 200°C. (Since it is a dielectric polymer, with resistivity $> 10^{17}$ Ω·m, it can be deposited over the entire chip area without causing any electrical shorting of the signal lines/electrodes.) In principle, Cytop also can be inkjet-printed.

Figure 6.3 shows a plan-view SEM micrograph of Au nanoparticle-sealed microshell, encapsulating one device. As shown in Chapter 5, the length of microshells can be made arbitrarily large if the width of the microshell is kept below 50 μm [4], which is beneficial in terms of layout area since each microshell should be allocated area for anchoring. In this work, up to 6 devices (not shown here) have been encapsulated in one microshell of 75-μm width. The surface profile of a microshell after the sacrificial LTO was removed by HF vapor etch was measured using an optical profilometer (Wyko NT3300 White light interferometer)

as shown in Fig. 6.4. This particular microshell encapsulates 6 devices, while only one device is shown in Fig. 6.4. Topographical map of a microshell is shown in Fig. 6.4(a) and height profile along the line across the device region (AA) is shown in Fig. 6.4(b). The surface of the microshell where underlying devices are encapsulated reflects the underlying structures (flexures and the movable electrode) because the sacrificial oxide was deposited conformally (Fig. 6.4(a)). The line profile (Fig. 6.4(b)) shows that the height of the microshell increased upon release due to a negative stress gradient within the printed film. This is beneficial since the microshell does not have a physical contact with encapsulated devices and hence does not affect the mechanical or electrical behavior of the encapsulated devices.

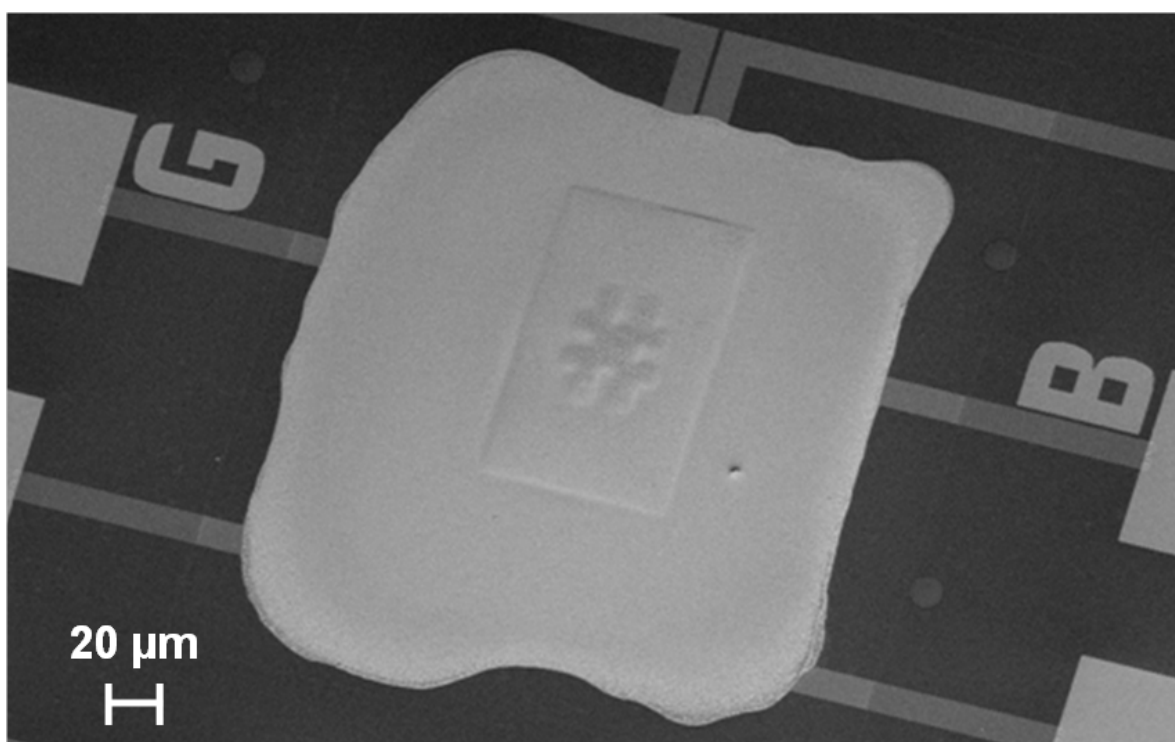


Figure 6.3: SEM image of a single encapsulated relay.

Figure 6.5 shows a micrograph of the patterned oxide (LTO) islands for microshells, where multiple devices (up to 6, not shown in the figure) were coated and encapsulated. The dimensions of the oxide patterns labeled in Fig. 6.5 are listed in Table 6.1. Packing of the devices into a confined area was not optimized for this test structure design and devices were distributed with rather large distances. The dimensions of the microshells follows those of oxide islands, whose width W_s was set to $75 \mu\text{m}$ since it was verified in Chapter 5 that the length of the shell L_s can be made arbitrarily large for $W_s < 100 \mu\text{m}$. Indeed, it was found that no collapse was observed even for the longest shell which encapsulates six devices ($L_{s6} = 2 \text{ mm}$). Electrical traces from the MEM relays were routed out to the outer contact pads for electrical measurement, and they were insulated by inter-dielectric

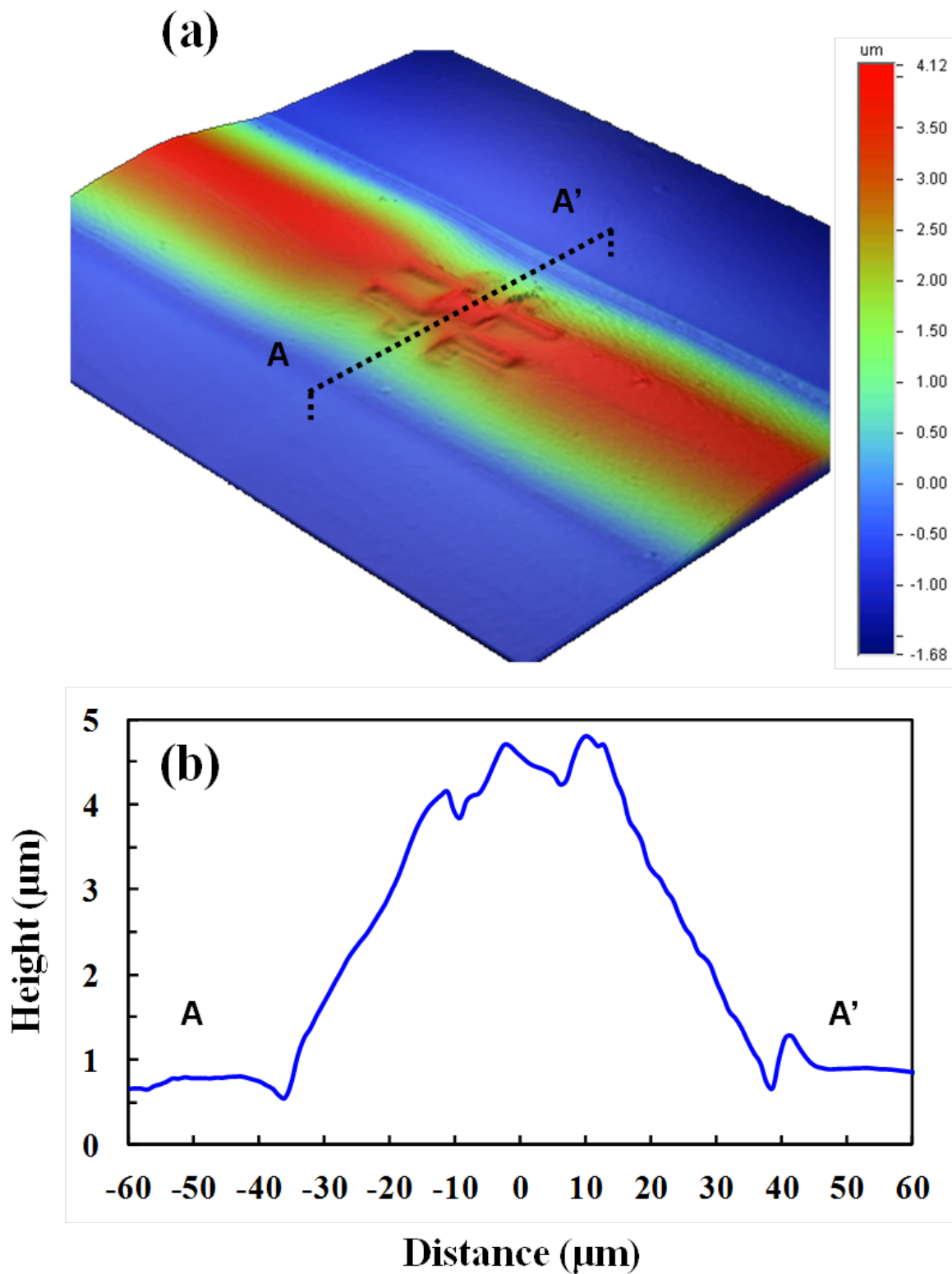


Figure 6.4: Surface profiles of a microshell-encapsulated MEM relay: (a) 3D topography map, and (b) corresponding surface height profile.

Parameters	Values (μm)
Length of shell for 1 relay L_{s1}	120
Length of shell for 2 relays L_{s2}	500
Length of shell for 3 relays L_{s3}	880
Length of shell for 6 relays L_{s4}	2000
Width of footing region W_f	100
Width of shell W_s	75

Table 6.1: Parameters and values of dimensions in the microshell test structures.

Al_2O_3 at the trench regions where the microshell makes anchors. This footing area needs to have a certain width (W_f) because of the non-uniform thickness variation of the printed nanoparticle film. The thickness of the printed microshell film peaks at the center of the film and decreases to the edges (Fig. 6.4). Microshell material is deposited to cover the oxide islands and fill the footing trench area as shown in Fig. 6.6, where Ag nanoparticle ink was inkjet-printed to the confined area. It is also beneficial to have this trench structure since it can confine the liquid phase nanoparticle ink upon deposition and during the drying, and hence a fine shaped structure can be obtained as shown in Fig. 6.6. Wetting of the nanoparticle ink on the surface was well controlled since it has a homogeneous (oxide-only) surface (SiO_2 and Al_2O_3) (water contact angle – footing region: Al_2O_3 $55^\circ \pm 5^\circ$ [5], shell region: SiO_2 $48^\circ \pm 2^\circ$ [6]).

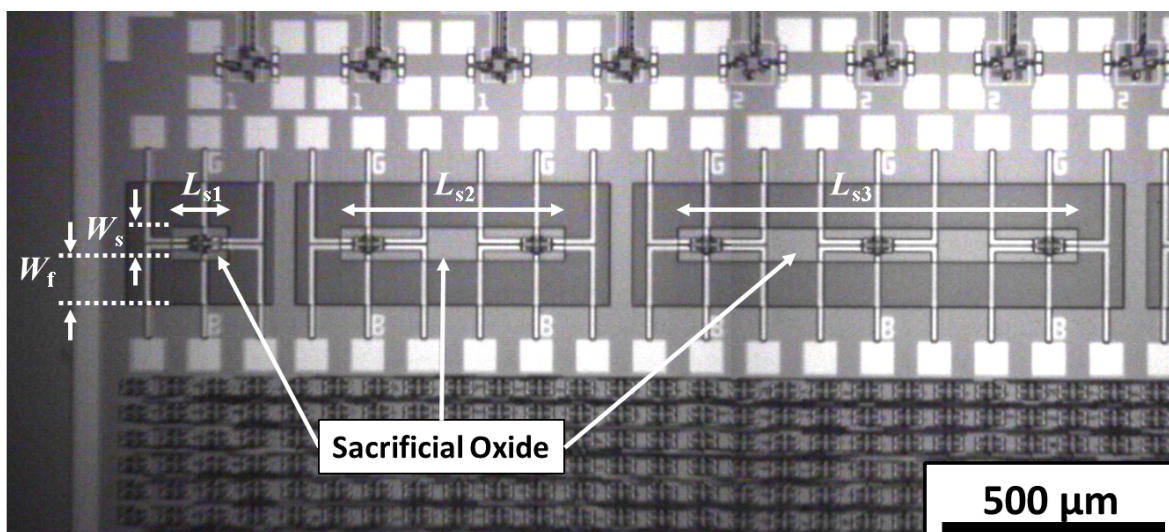


Figure 6.5: Micrograph of the patterned oxide islands for microshells encapsulating MEM relays. Oxide islands were patterned to have various lengths to span multiple devices by one microshell.

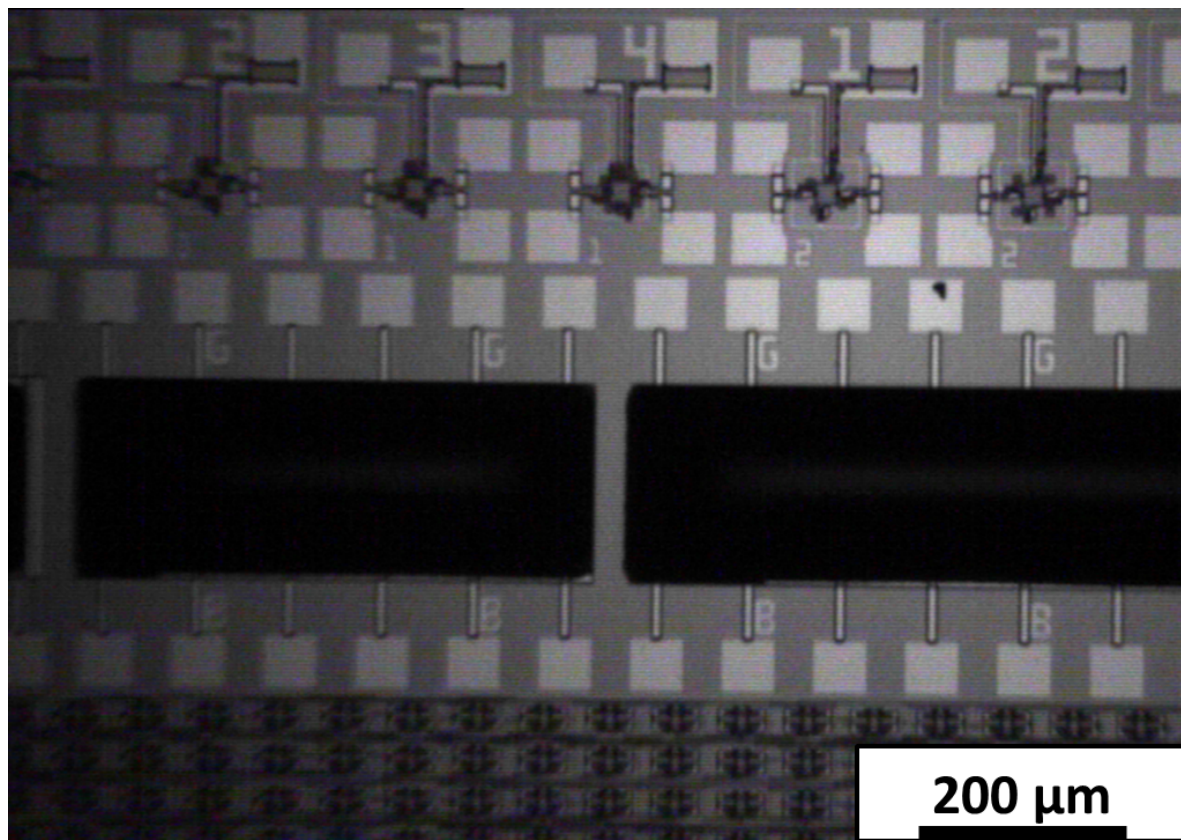


Figure 6.6: Micrograph of printed Ag nanoparticle ink on patterned oxide islands.

The deposited nanoparticle film becomes solidified after drying (150°C , 15 min.), and the next layer is deposited after this interspersed drying step to increase the microshell thickness. A total of 6 layers were deposited to obtain the final thickness and intermediate sintering (200°C , 30 min.) was performed after deposition of the first 3 layers to reduce stress-induced crack formation (Chapter 5). It is worth studying the change of the structure after the completion of the microshell deposition and after release by vapor HF oxide etch. Figure 6.7 shows surface height profiles of the printed microshell after completion of depositing the total of 6 layers and sintering. A topographical map of the microshell is shown in Fig. 6.7(a), where horizontal (X) and vertical (Y) height profiles along the three position markers are shown in Fig. 6.7(b,c). The topography of the encapsulated device is reflected at the center of the microshell, clearly evident both in X and Y profiles indicated in red lines (Fig. 6.7(b,c)). The green and blue line markers in the X profile are positioned along the anchoring edge of the microshells, while the red marker scans along the center of the microshell where the height is maximum. The difference between the red and blue/green line profile indicates this height difference between the top of the microshell and anchoring region ($\sim 0.8 \mu\text{m}$) and this corresponds to the value of the deposited sacrificial oxide thickness (Fig. 6.7(b)).

The thickness decrease from the center to the edge of the printed nanoparticle film can be clearly observed in the line profile along the Y -direction, where $\sim 0.5 \mu\text{m}$ difference was seen between the boundary of the anchor and shell edge (Fig. 6.7(c)). It is worth comparing this surface profile to that measured after the microshell structure is released by removing the encapsulated oxide. The surface height values of the same position were mapped and shown in Fig. 6.8. It should be noted that the peak height of the shell increased upon release, as can be seen from the difference between the average value of red line marker and blue/green markers in the X - and Y -profile data. The height increased by $\sim 3 \mu\text{m}$, from $\sim 0.8 \mu\text{m}$ to $\sim 3.8 \mu\text{m}$, upon release due to a negative stress gradient in the film.

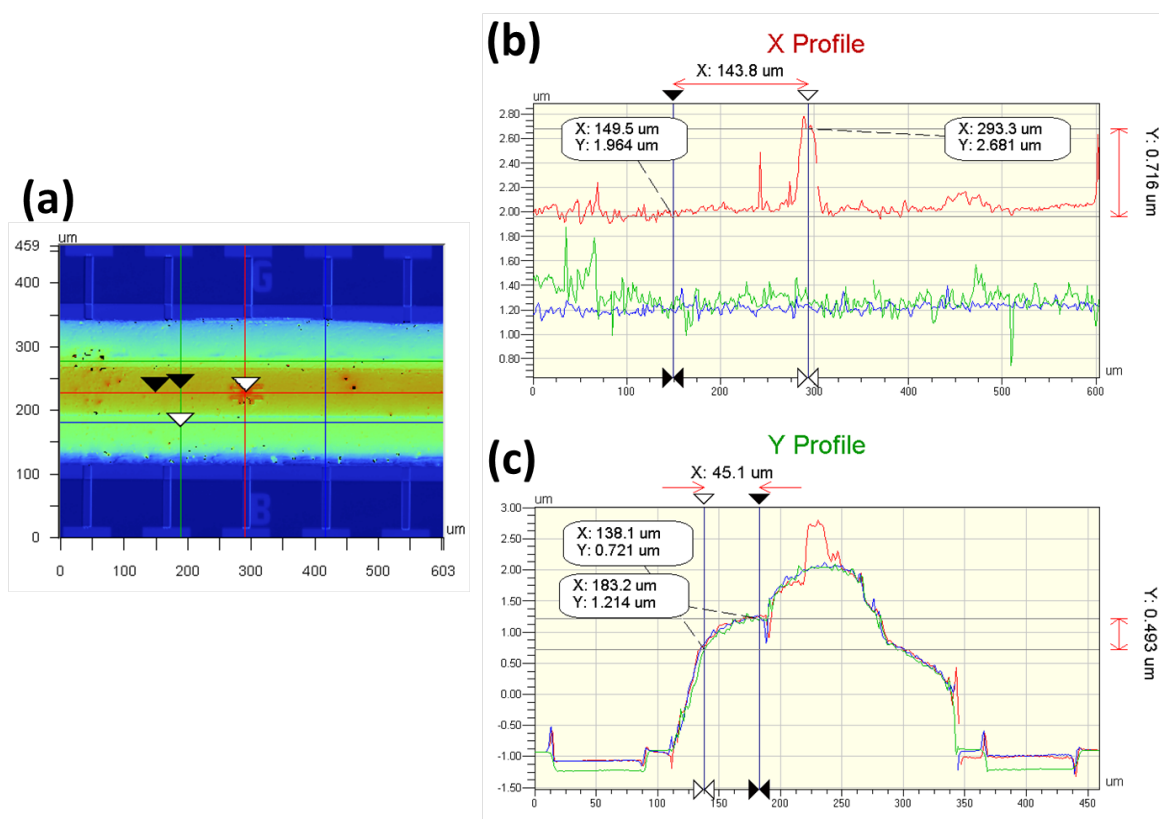


Figure 6.7: Surface profiles of a microshell-encapsulated MEM relay after completion of microshell deposition. (a) 3D topography map with 3 line markers, and corresponding surface height profiles along the markers in (b) X , and (c) Y directions.

As verified in the previous chapter, the microshell film thickness was controlled to obtain sufficient mechanical strength to avoid structural collapse. It was adjusted by printing 6 layers of Ag ink to obtain a thickness of $\sim 2.7 = 0.45 \times 6 \mu\text{m}$, since the thickness of each printed layer is $\sim 0.45 \mu\text{m}$. Maximum deflection at the center of the microshell under ambient pressure is calculated as shown in Fig. 6.9. It was assumed that the microshell has

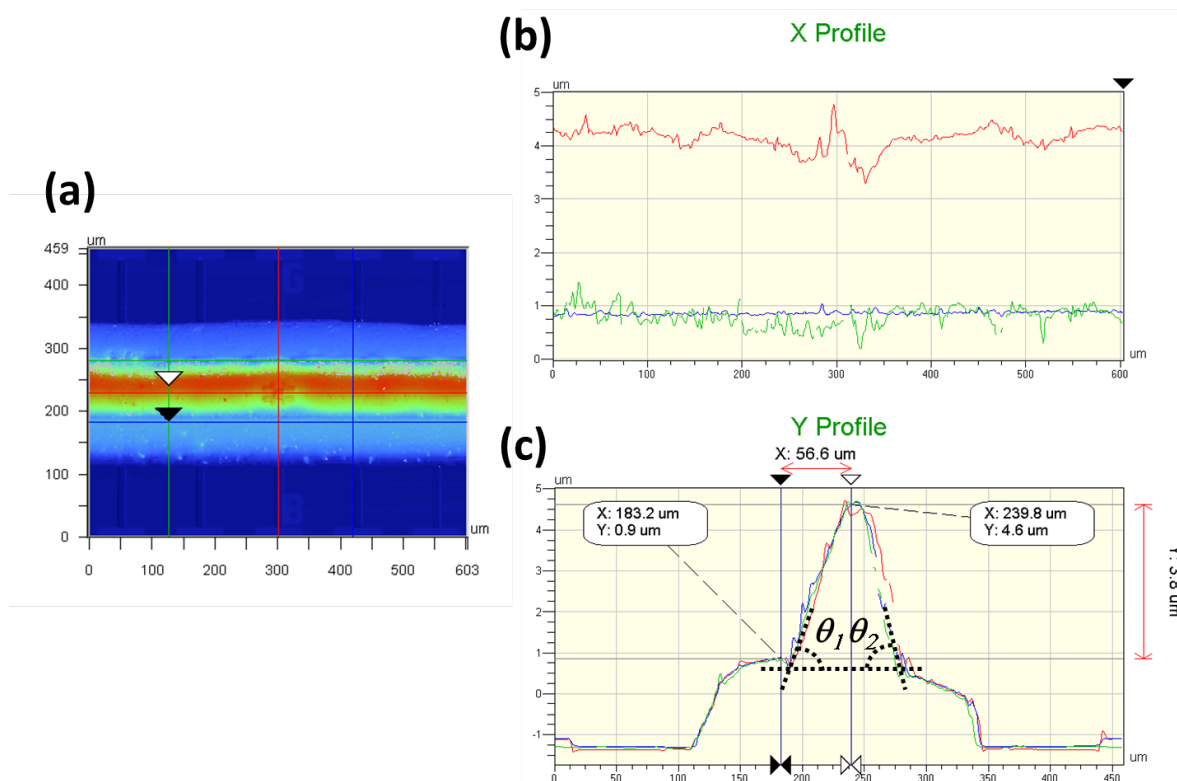


Figure 6.8: Surface profiles of a microshell-encapsulated MEM relay after oxide removal by vapor HF etch. (a) 3D topography map with 3 line markers, and corresponding surface height profiles along the markers in (b) X, and (c) Y directions.

built-in edge and uniform thickness on the plate, using the following equation [7]:

$$w = \frac{0.00126qa^4}{D} \quad (6.1)$$

where w is the maximum deflection (at the center) of the microshell, q is the intensity of a distributed load, a is the length of the plate (assuming the square plate), and D is the flexural rigidity for the microshell. The flexural rigidity D can be obtained as follows:

$$D = \frac{Eh^3}{12(1 - \nu^2)} \quad (6.2)$$

where E is the elastic modulus of the microshell material, h is the film thickness of the microshell, and ν is the Poisson ratio. The ambient pressure of 1atm was assumed and $E = 50$ GPa was used for the calculation of D , which was obtained from nanoindentation measurement on the printed Ag nanoparticle film. Figure 6.9 shows the calculation of the maximum deflection of the microshell as a function of shell length and thickness. It can be

noted that the deflection of the microshell is negligible when the shell length is set $< 100 \mu\text{m}$, for shell thickness larger than $\sim 2.5 \mu\text{m}$, as tested in the previous chapter.

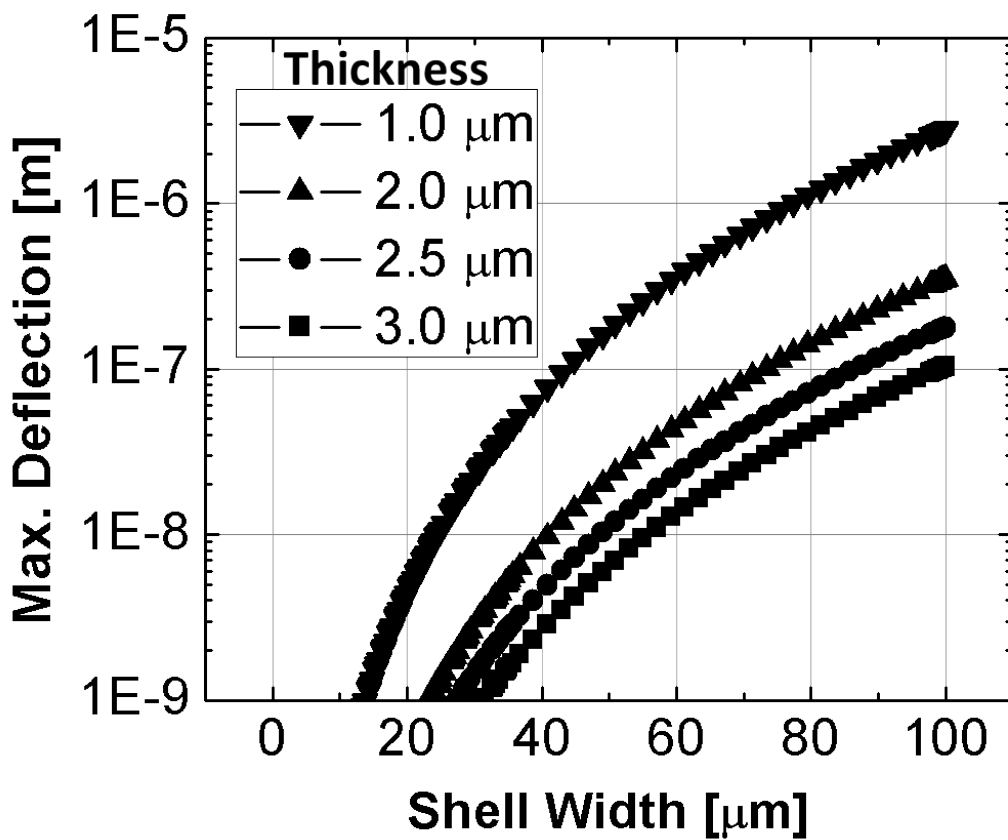


Figure 6.9: Plot of calculated maximum shell deflection under ambient pressure with varying widths and thickness of the square microshell. It was assumed that the microshell has built-in edge, uniform thickness on the plate, and no stress gradient.

6.3 Contact Resistance Stability Results

Measured electrical characteristics of a bare relay and an encapsulated relay are compared in Fig. 6.10, where negligible difference is observed. This comparison shows that the printed microshell process has not affected the MEM relay electrical/mechanical performance. It should be noted that the thermal process for annealing both Ag and Au nanoparticles ($\leq 200^\circ\text{C}$) and the deposition of sealing material (Au nanoparticles) did not cause any observable change of MEM relay performance.

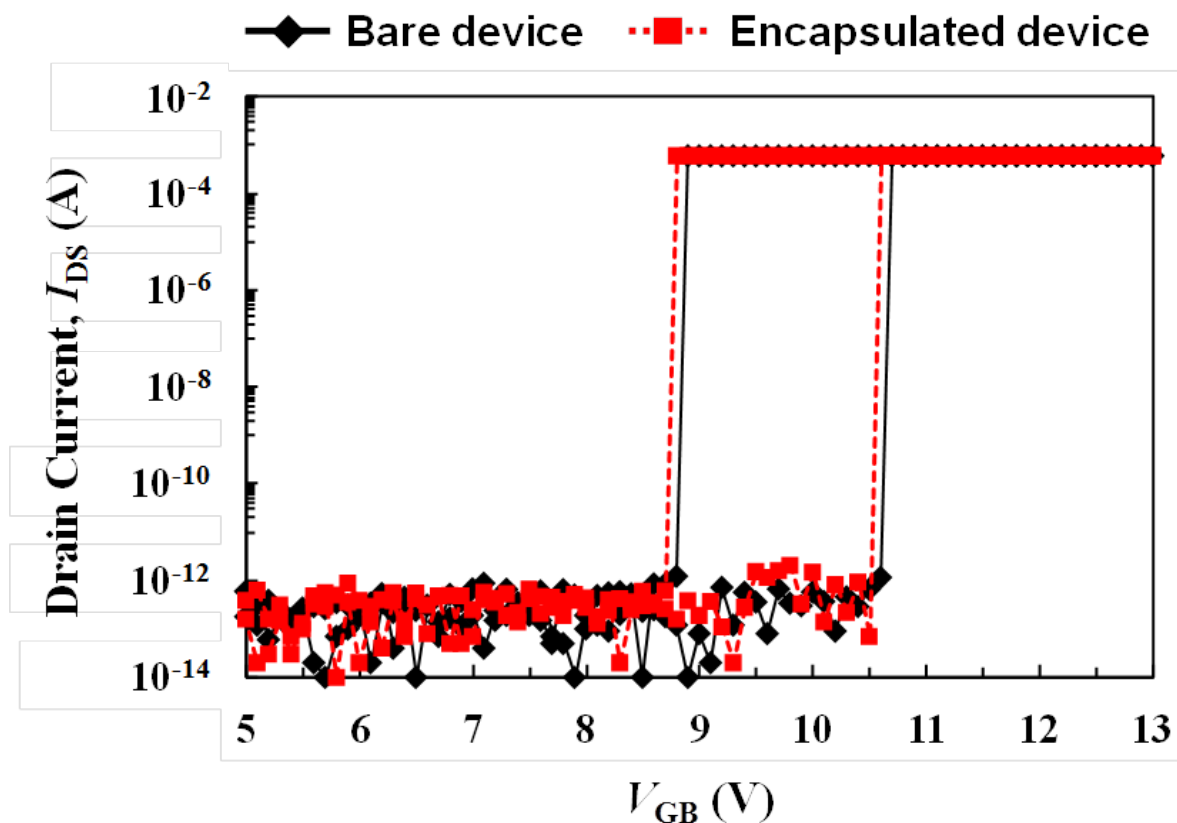


Figure 6.10: Comparison of measured I-V characteristics for a bare relay vs. an encapsulated relay, showing that the MEM relay electrical/mechanical performance is not affected by the 200C packaging process. The current compliance was set to 600A.

The measurement setup used to study ON-state resistance R_{ON} stability of MEM relays is illustrated in Fig. 6.11. It is an inverter-like setup where the MEM relay acting as a pull-down device, and is connected in series with a load resistor. The gate electrode is connected to a voltage pulse signal (amplitude 15 V, frequency 5 kHz) to drive the MEM relay, switching ON and OFF repeatedly, and the evolution of R_{ON} over multiple switching cycles (which is obtained by a voltage-divider formula) can be determined. This stability test measurement was done at room temperature (300K) and ambient air. It should be noted that the device is under harsher stress in this measurement setup than in normal digital logic operation, where the period of time in which the device under stress is limited to the RC charging delay whenever the device is switched ON. Figure 6.12 shows the measured evolution of R_{ON} with the number of switching cycles, where R_{ON} increases over cycles due to the oxidation of W electrode at the contact. In order for the MEM relay to be employed in digital logic circuits, R_{ON} should remain below ~ 10 k Ω to avoid any significant performance degradation [8]. For a bare (unencapsulated) device, R_{ON} passes this threshold after $\sim 10^5$ cycles. In contrast,

R_{ON} remains stable up to $\sim 10^7$ cycles for microshell-encapsulated devices, sealed either using Au nanoparticles or Cytop, so that the effective relay operating lifetime is enhanced by $\sim 100\times$ with encapsulation. The reason why Cytop-sealed device shows a slightly higher relay operating lifetime may come from the fact that the Cytop sealing process was carried out entirely inside a glovebox where the oxygen level is kept very low, while the deposition of sealing Au nanoparticles were performed in a room air ambient.

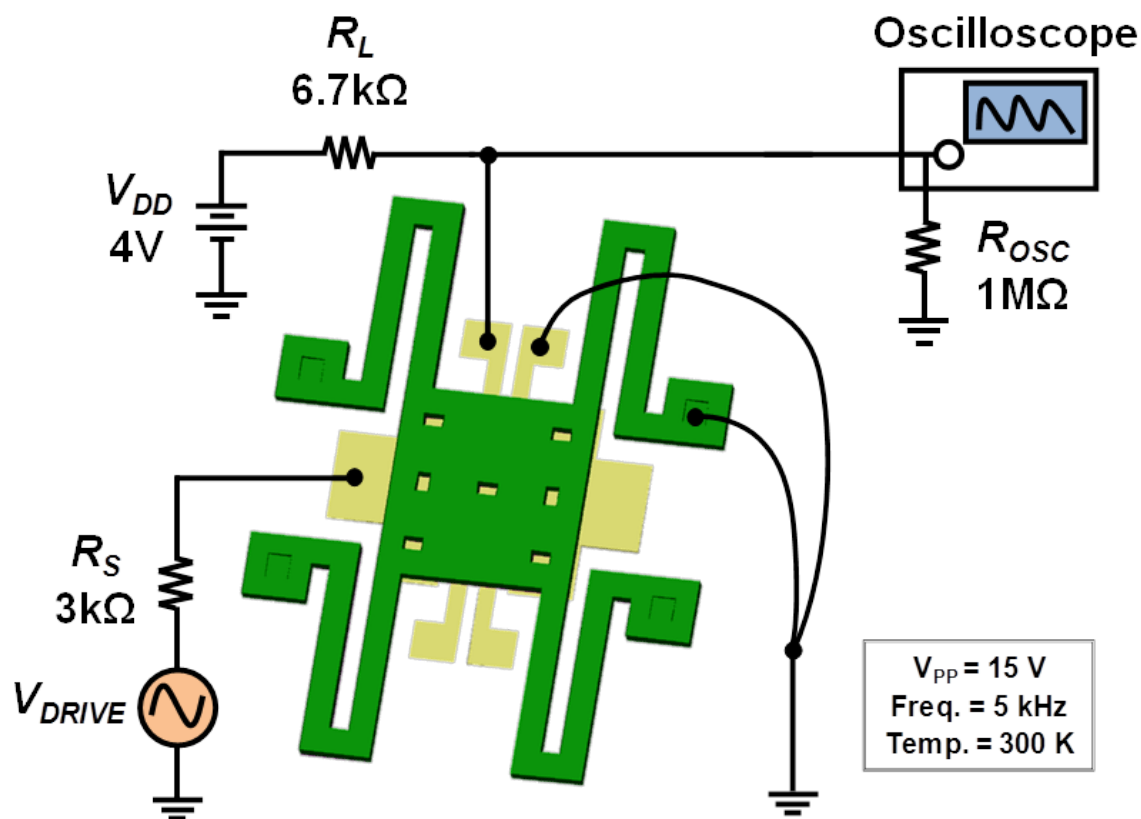


Figure 6.11: Test setup for monitoring relay ON-state resistance over many hot-switching cycles.

It should be noted that some contamination may result from the microshell sealing process. The Au nanoparticles are originally covered with an organic material (ligands) to prevent them from aggregating within the ink; when the printed ink is dried/solidified by thermal annealing, this organic material vaporizes and some of it may diffuse through the pores of the Ag film into the microshell cavity. Cytop is only available in perfluorinated solvents, which outgas during thermal annealing and may end up in the microshell cavity

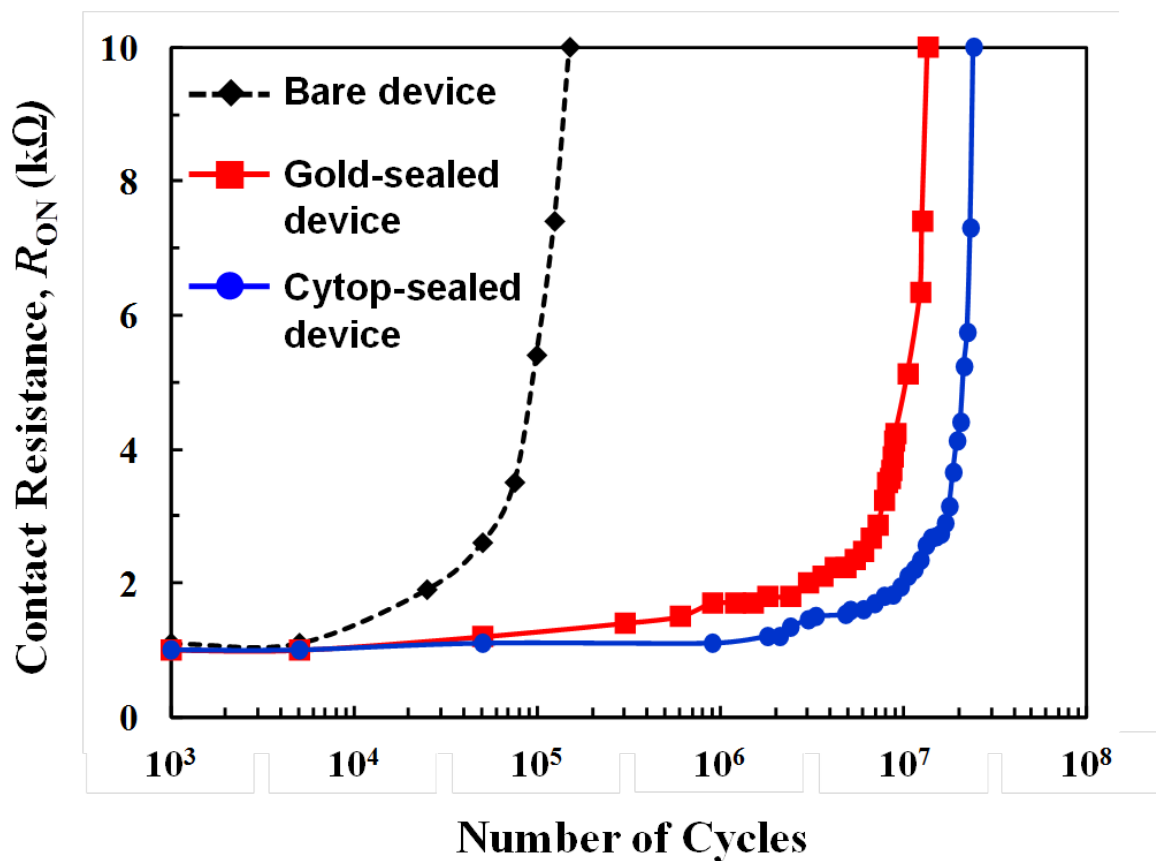


Figure 6.12: Evolution of contact resistance with the number of hot-switching cycles, for bare vs. encapsulated relays. The effective relay operating lifetime is enhanced by 100 with encapsulation.

as well. Differences in the outgassing levels for Au nanoparticle ink vs. Cytop might also account (in part) for the superior R_{ON} stability of the Cytop-sealed relay.

6.4 Conclusion

A low-thermal-budget inkjet printed microshell encapsulation technology is successfully applied to micro-relays for dramatically enhanced contact stability, by 100 \times . With further process refinements (e.g. incorporation of a getter material, annealing under lower ambient pressure) this technology can facilitate the cost-effective manufacture of reliable relay integrated circuits.

Bibliography

- [1] R Nathanael et al. “4-terminal relay technology for complementary logic”. In: *Electron Devices Meeting (IEDM), 2009 IEEE International*. 2009, pp. 1–4.
- [2] R Nathanael et al. “Multi-input/multi-output relay design for more compact and versatile implementation of digital logic with zero leakage”. In: *VLSI Technology, Systems, and Applications (VLSI-TSA), 2012 International Symposium on*. 2012, pp. 1–2.
- [3] V Pott et al. “Mechanical Computing Redux: Relays for Integrated Circuit Applications”. In: *Proceedings of the IEEE*. Vol. 98. 12. 2010, pp. 2076–2094.
- [4] E S Park et al. “Inkjet-printed microshell encapsulation: A new zero-level packaging technology”. In: *Micro Electro Mechanical Systems (MEMS), 2012 IEEE 25th International Conference on*. 2012, pp. 357–360.
- [5] Dudley S Finch et al. “Biocompatibility of atomic layer-deposited alumina thin films”. In: *Journal of Biomedical Materials Research Part A* 87A (1) (Oct. 2008), pp. 100–106.
- [6] R G Frieser. “Characterization of Thermally Grown SiO₂ Surfaces by Contact Angle Measurements”. In: *Journal of The Electrochemical Society* 121 (5) (May 1974), pp. 669–672.
- [7] Liwei Lin. “Selective encapsulations of MEMS: Micro channels, needles, resonators and electromechanical filters”. Ph. D. University of California at Berkeley, 1993.
- [8] F Chen et al. “Integrated circuit design with NEM relays”. In: *Computer-Aided Design, 2008. ICCAD 2008. IEEE/ACM International Conference on*. 2008, pp. 750–757.

Chapter 7

Conclusion

7.1 Summary and Conclusion

In this dissertation, new processes were developed to fabricate micro-electro-mechanical systems (MEMS) using inkjet printing technology. The conventional solution-processed thin-film transistors (TFTs) generally suffer from poor performance which results from the performance of printable semiconductors. On the other hand, performance of printable metals have already approached to that of their solid-state counterpart. Therefore, it would be interesting to develop an alternative scheme of switches, which avoids usage of printable semiconductors at all and employs only solution-processed metals, in this regard. It can be implemented by building mechanical switches, rather than electrical switches. A novel fabrication process which can implement MEM switches using inkjet-printed metal nanoparticle films has been presented.

The inkjet printing technology can also be employed to provide conventional MEMS with packaging. In the field of conventional MEMS using surface-micromachining process, packaging is an important field which holds a key to successful commercialization of MEMS. It is also a process that is the biggest cost of the various parts of the whole MEMS process. The requirements of the package also include low process temperature in order to be CMOS compatible so that the MEMS can be integrated into CMOS devices to obtain potential synergy. It is therefore ideal to employ inkjet-printing technology to implement a MEMS packaging process as it can satisfy most of the requirements mentioned above. Therefore, a new process was developed to fabricate microshell encapsulation package using inkjet-printed nanoparticle films.

In chapter 3, a new switch technology for printed electronics based on inkjet-printed MEM cantilevers was demonstrated. The MEM switches offer excellent on-state and off-state characteristics, and appear to be very promising for printed electronics applications. Several novel process steps were realized to ensure precise control of the actuation gap in printed MEM structures, and the resulting devices showed low on-resistance, immeasurable leakage, good switching speed, and low voltage operation better than that of other many

printed electronic devices.

In chapter 4, performance of the printed MEM switch was improved by scaling down the actuation gap and the process optimization was presented. It is straightforward to reduce the gap thickness by adjusting that of the sacrificial layer since the pull-in voltage has larger dependency on the gap among other dimensions. The pull-in voltage of the switch was successfully reduced by $\sim 70\%$. Process optimization was carried out to obtain the gap scaling by studying the trade-offs from UV-ozone time, which impacts the speed, variation, and scalability of the process.

In chapter 5, a low-thermal-budget ($< 300^\circ\text{C}$) microshell encapsulation process using inkjet-printed nanoparticle inks is demonstrated. Printed nanoparticles (~ 50 nm) films of thickness greater than ~ 2.5 μm have sufficient mechanical strength to be used for microshell encapsulation of MEMS devices while being permeable to vapor HF to allow for short release times. They can be effectively sealed with a printed gold nanoparticle (~ 5 nm) film. The low thermal budget of a printed microshell encapsulation process makes it attractive for low-cost packaging of monolithically integrated microsystems.

In chapter 6, the inkjet printed microshell encapsulation technology is successfully applied to micro-relays for dramatically enhanced contact stability, by $100\times$. With further process refinements (e.g. incorporation of a getter material, annealing under low ambient pressure) this technology can facilitate the cost-effective manufacture of reliable relay integrated circuits.

7.2 Contributions of This Work

New processes for inkjet-printed MEM structures from solution-processed metal nanoparticles are developed and the fabricated device structures are characterized to study their electrical and mechanical performance. A two-step beam process has been developed which enables successful beam anchoring and hence results in the implementation of the printed MEM switch. The printed nanoparticle films show sufficient mechanical strength as well as excellent electrical conductivity, which are required for MEM structural and electrode materials. It shows that the printed nanoparticles can be a promising candidate material for future printed MEM applications. The performance of printed MEM switches shows promising results and suggests that they can be readily employed to proper applications such as pixel switches in active matrix liquid crystal displays and further process optimization may even improve their performance to be suitable for broader range of applications. Printed microshell encapsulation demonstrated using the newly developed process and it was shown that the contact resistance stability of packaged MEM relays can be enhanced by $\sim 100\times$.

7.3 Suggested Future Work

7.3.1 Process Optimization

Further process optimization can be pursued to improve performance of the printed MEM switches. As addressed in Chapter 4, the ‘undercut’ from the via-hole process may induce variations of the beam length due to accidentally increased size of the anchor by filling of the undercut region during the anchor formation process. It was shown that the length of such undercuts can be reduced by optimizing UV-ozone exposure time. If less aggressive solvent, for example, a developer designed specifically for the sacrificial PMMA (MIBK, MicroChem) is used as ‘etchant’ in the via-hole process, instead of acetone, finer control may be obtained in the dissolution of PMMA. It should also be noted that a different choice of materials can also be considered as a sacrificial layer. In this work, PMMA was chosen for several properties; thermal resistance required to endure the sintering temperature of the beam material, solvent orthogonality to minimize the interaction with the beam material, and dissolving property which is necessary for via-hole opening and anchor formation. Although it satisfies most of the requirements, it is not perfectly orthogonal to the silver nanoparticle ink so that some amount of dissolution occurs during the beam printing (100 ~ 200 nm), which can be an additional source of device performance variation, especially for device having scaled actuation gaps. Therefore it would be worth searching for candidate materials for the sacrificial layer which can satisfy those requirement more faithfully. It would be ideal if it can be inkjet-printed with uniform surface thickness so that the beam can be anchored in a simpler one-step process.

7.3.2 Scaling Device Dimensions

It is also worth pursuing scaling the lateral device dimensions. The printed MEM switches demonstrated in this dissertation have unoptimized device size: beam length $\sim 600 \mu\text{m}$ and beam width $\sim 100 \mu\text{m}$. Although it was shown that the operating voltage can be reduced to $\sim 5 \text{ V}$ by straightforward vertical scaling of the actuation gap, lateral dimensions of the devices can also be scaled down in order to increase device density.

The printed MEMS switches provide excellent ON-state conductivity and OFF-state resistivity due to its metallic structure material and air-gap separated channel electrode, respectively. These characteristics would make the device to be ideal for power inverters. The current-carrying capacity of the printed MEM switches was investigated by studying device failure while increasing the drain current, as shown in Fig. 7.1. It was shown that the device can flow up to $< 10 \text{ mA}$ without failure from stiction or welding issue. One straightforward method to improve its current-carrying capacity would increase the contact area, so that the contact resistance should be reduced to suppress joule heating at the contact. These factors should be considered when deciding the device dimension for the scaling; different set of strategies are required for components of the devices, depending on the applications.

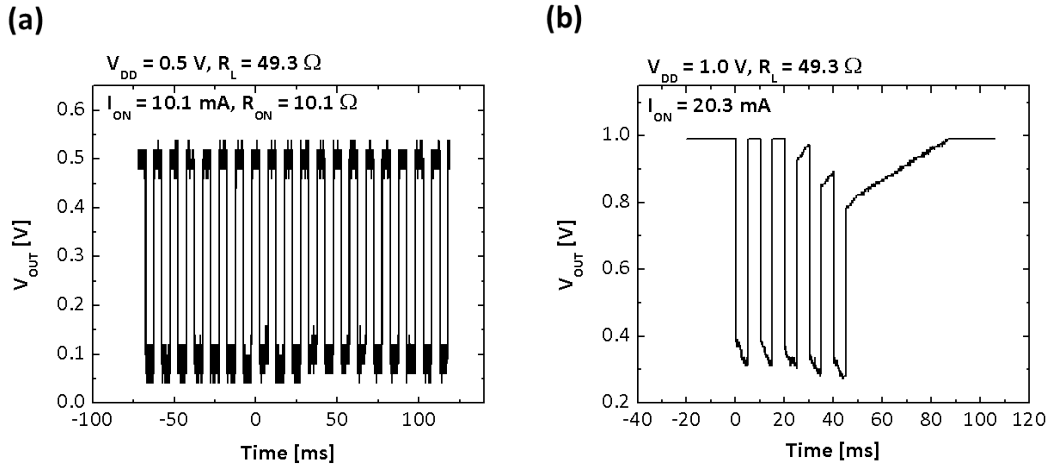


Figure 7.1: Measured current-carrying capacity of the printed MEM switches. Maximum drain current I_{DS} which flows through the source-drain contact was adjusted by the drain voltage V_{DS} , where (a) $V_{DD} = 0.5V$ and (b) $V_{DD} = 1.0V$. It is evident that the switch is not able to be pulled off from the contact for $I_{DS} > 10$ mA, probably due to welding at the contact. The measurement was carried out using an inverter-like setup as shown in Fig. 3.11.

7.3.3 Four-Terminal Printed MEM Switch

As is in solid-state MEMS relays presented in chapter 6, four-terminal (4T) relay design have advantages over the three-terminal (3T) configuration in that it enables to adjust pull-in and release voltages by body biasing. This allows the same 4T relays to perform either as a pull-down or pull-up device, and hence complementary logic circuits can be implemented [1, 2, 3]. The channel electrode which connects the drain and source electrodes should be electrically isolated from the body electrode in the 4T relay design. Therefore, the current 3T configuration can be modified to implement 4T design. Specifically, the monolithic beam can be changed to have an insulating gate dielectric sandwiched by two conductive electrodes; channel and body.

Two potential 4T relay schemes are illustrated in Fig. 7.2, where the source and drain electrodes are positioned either in series at the free-end of the beam or in parallel under the beam. The channel electrode, which is attached to the bottom electrode via printed gate dielectric, can provide an electrical path by making physical contact with both electrodes when the beam is pulled down. The gate dielectric is required to provide electrical isolation between the channel and body electrode, as well as sufficient mechanical adhesion between the two electrodes. In a serial-source/drain electrode configuration, as in Fig. 7.2(a), physical contact between the beam and source/drain electrode is assured due to the curvature of the cantilever beam deflection. The width of the channel electrode, and hence the beam, is required to overlap both of the source/drain electrode in this configuration, which may limit the scalability of the device size. In a parallel-source/drain electrode design, as in Fig. 7.2(b),

beam width can be scaled as required. However, the beam length should be decided so that a stable contact can be obtained at the beam-source electrode contact.

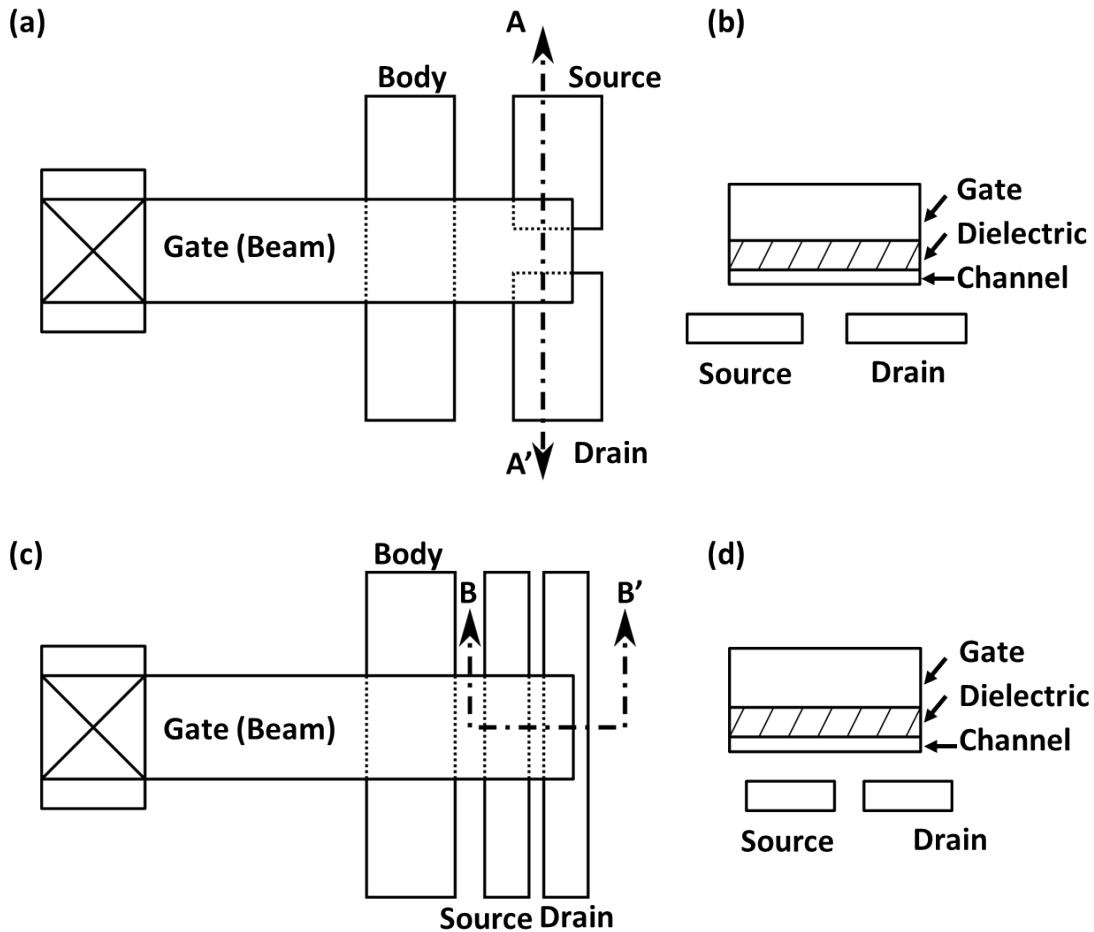


Figure 7.2: Schematic diagrams illustrate design schemes for printed four-terminal relays. The source and drain electrodes are positioned either (a,b) in series at the free-end of the beam, or (c,d) in parallel under the beam.

7.3.4 Material Selection for Printed Microshell Encapsulation

The printed microshell encapsulation in Chapter 6 successfully enhanced the life cycle of the sealed MEM relays by $\sim 100\times$. It should be noted that the contact oxidation still occurs although delayed for the sealed MEM relays. This suggests that the oxygen level inside the sealed microshell should be further reduced at the sealing process or during the device operation in order to provide better contact stability. The use of getter materials which can actively absorb active molecules in a vacuum environment, such as oxygen and/or hydrogen

molecules, can be a solution. It has been widely known in the field of MEMS packaging that the concentration of such molecules inside the cavity of the packages can be suppressed by getter material films, such as Zr or Ti, deposited inside the package [4, 5, 6]. Therefore, it would be possible to implement such getter materials by depositing it on the sacrificial layer, followed by patterning the microshell material, to absorb oxygen molecules inside the shell cavity. The getter material can also be deposited by inkjet printing, which is also advantageous in terms of the getter performance since the rough surface of the printed films will increase surface area.

Bibliography

- [1] Rhesa Nathanael et al. “Four-Terminal-Relay Body-Biasing Schemes for Complementary Logic Circuits”. In: *Electron Device Letters, IEEE* 31 (8) (Aug. 2010), pp. 890–892.
- [2] Jaeseok Jeon, Rhesa Nathanael, and Vincent Pott. “Four-Terminal Relay Design for Improved Body Effect”. In: *IEEE Electron Device Letters* 31 (5) (May 2010), pp. 515–517.
- [3] Tsu-Jae King Liu et al. “Prospects for MEM logic switch technology”. In: *Electron Devices Meeting (IEDM), 2010 IEEE International*. 2010, pp. 18.3.1–18.3.4.
- [4] Rajeshuni Ramesham and Richard C Kullberg. “Review of vacuum packaging and maintenance of MEMS and the use of getters therein”. In: *Journal of Micro/Nanolithography, MEMS, and MOEMS* 8 (3) (2009), pp. 31307–31309.
- [5] Byeungleul Lee, Seonho Seok, and Kukjin Chun. “A study on wafer level vacuum packaging for MEMS devices”. In: *Journal of Micromechanics and Microengineering* 13 (5) (Sept. 2003), pp. 663–669.
- [6] Gil-Geun Lee and Je-Shin Park. “Hydrogen Sorption Property of Zr₅₅V₂₉Fe₁₆ Nanopowder Synthesized by the Plasma Arc Discharge Process”. In: *Materials Transactions* 48 (6) (2007), pp. 1566–1570.